Studies of Metalloporphyrins and Tantalum Amide Imide Compounds

A Dissertation Presented for the

Doctor of Philosophy

Degree

The University of Tennessee, Knoxville

Seth Carlton Hunter

May 2015

Dedication

This dissertation is dedicated to my wife Melissa for her love and support throughout my graduate career. I would also like to dedicate this dissertation to my parents, Robert and Gina Hunter, for their continuous love and support. Finally, I want to also dedicate this dissertation to my son, Max, who has made the last few years of graduate school extra special.

Acknowledgement

I would first and foremost like to thank my advisor, Dr. Ziling (Ben) Xue for his guidance and support during my time here at UTK. My committee members, Dr. Craig Barnes, Dr. Jon Camden, Dr. Claudia Rawn, and Dr. Brian Long, are acknowledged for their time and consideration of my dissertation. I would like to give special thanks to Dr. Long for agreeing to fill Dr. Camden's position on my committee. Several scientists at Oak Ridge National Laboratory (ORNL) play critical roles in my research. Dr. Andrey Podlesnyak has helped run my samples at the Spallation Neutron Source (SNS) and taught me how to analyze neutron scattering data. Drs. Christina Hoffman and Xiaoping Wang have guided me in the studies of solid-state structures of metalloporphyrins.

I would like to thank my past and present group members for their help and encouragement throughout my graduate career. Special thanks go to Shujian (Jim) Chen, Adam Lamb, Julia Abbott, Maozhong Miao, and Tabitha Callaway for teaching me lab skills and how to operate instruments. I would also like to acknowledge other group members, Stefanie Bragg, Bhavna Sharma, Thomas Carpenter, Royce Dansby-Sparks, Jonathan Fong, Roberto Alan Federico-Perez, Shelby Stavretis, Kendhl Whitt, and Duncan Moseley.

I would like to thank the Joint Institute for Neutron Science Fellowship in supporting my graduate studies, American Chemical Society Petroleum Research Fund for supporting my metalloporphyrin research, ORNL and the Department of Energy for the use of SNS for neutron scattering work, and National Science Foundation for funding my research on tantalum imide chemistry.

Abstract

The focus of this dissertation is on two different subjects. The first examines the magnetic and structural properties of metalloporphyrins. In these studies, neutrons were used to probe the magnetic properties of metalloporphyrins. Insight on the structural properties of metalloporphyrins was also gained by examining the intermolecular interactions in the solid state. The second subject is the synthesis and characterization of new tantalum complexes and studies of their reactions with O_2 [dioxygen]. These complexes are potential precursors to make metal oxide and metal nitride thin films.

In the first part of this dissertation, the zero-field parameters *D* have been directly determined for [M(TPP)Cl] (M = Cr, Mn, Fe, TPP = *meso*-tetraphenylporphyrinate) and [Mn(TPP)] using inelastic neutron scattering (INS). Non-deuterated samples were used to measure small energy differences of the magnetic excitations in these metalloporphyrins. To our knowledge, this is the first time INS has been used to probe the magnetic excitations in bioinorganic complexes.

Intermolecular interactions in the solid state structures of biomimetic [Fe(TPP)Cl] and [M(TPP)NO] (M = Fe, Co) have been studied using Hirshfeld surface analysis. It was revealed that intermolecular interactions are a significant factor in structure disorders in the three metalloporphyrins and phase changes in the nitrosyl complexes. At the phase change a significant void volume increase was gained by the gradual tilting of phenyl rings, enabling further thermal compression at low temperatures.

In the second half of this dissertation, mixed amide imide alkyl complexes $TaR_2(=NSiMe_3)[N(SiMe_3)_2]$ [tantalum alkyl amide imide] (R = Me or CH_2Ph [benzyl]) have

been synthesized and characterized. Their reactions with O_2 [dioxygen] have also been probed, revealing the unique nature of these reactions. Crystal structures of $Ta(CH_2Ph)_2(=NSiMe_3)[N(SiMe_3)_2]$ [tantalum benzyl amide imide] and the methoxy dimer $Ta_2(\mu\text{-}OMe)_2(=NSiMe_3)_2[N(SiMe_3)_2]_2Me_2$ [tantalum amide imide methyl methoxy dimer] have been solved and are discussed.

The mixed amide imide complexes $Ta(NR_2)(=NSiMe_3)[N(SiMe_3)_2]$ [tantalum amide imide] (R = Me or Et) have been synthesized from two different starting materials and characterized. One of the reactions involves a rare intramolecular imidation between two amide ligands. The intramolecular imidation has been studied further to gain an understanding of its mechanism.

Table of Contents

List of Tables

List of Figures

List of Schemes

Numbering Scheme for the Compounds in the Text

1	[Fe(TPP)Cl]
2	[Mn(TPP)Cl]
3	[Cr(TPP)Cl]
4	[Mn(TPP)]
5	[Fe(TPP)(NO)]
6	[Co(TPP)(NO)]
7	$TaCl_3(NSiMe_3)_2$
8	$\{Ta(\mu\text{-}Cl)Cl(=NSiMe_3)[N(SiMe_3)_2]\}_2$
9	$TaMe_2(=NSiMe_3)[N(SiMe_3)_2]$
10	$Ta(CH_2Ph)_2(=NSiMe_3)[N(SiMe_3)_2]$
***cis*-11**	$Ta_2(\mu\text{-}OMe)_2(=NSiMe_3)_2[N(SiMe_3)_2]_2Me_2$
***trans*-11**	$Ta_2(\mu\text{-}OMe)_2(=NSiMe_3)_2[N(SiMe_3)_2]_2Me_2$
12	$Ta(NMe_2)_2(=NSiMe_3)[N(SiMe_3)_2]$
13	$Ta(NEt_2)_2(=NSiMe_3)[N(SiMe_3)_2]$
14	[Fe(TPP)]

Part 1

Introduction

This dissertation covers two areas of my Ph.D. research: (1) Structures and magnetic properties of metalloporphyrins; (2) Syntheses and reactions of tantalum imide complexes. This part provides introduction to the two areas.

1.1. Studies of Magnetic Excitations Using Inelastic Neutron Scattering (INS)

Chemistry of metalloporphyrins is a rich and diverse one, as metalloporphyrins are found naturally in both biological and geological systems.[1-3] Many metalloporphyrins often have unpaired electrons, making the compounds paramagnetic. One intrinsic property of paramagnetic compounds is the zero-field splitting (ZFS). For compounds with spin $S \geq 1$, the interaction of the electron spins mediated by spin orbital coupling leads to a splitting of the spin states of otherwise degenerate states.[4-6] The spin Hamiltonian is given in Eq. 1.1:

$$\widehat{H}_s = D\left[\hat{S}_z^2 - \frac{1}{3}S(S+1)\right] + E[\hat{S}_x^2 - \hat{S}_y^2] \qquad \text{(Eq. 1.1)}$$

where *D* and *E* are the axial and rhombic ZFS parameters, respectively, which measure the magnetic anisotropy of the system.

ZFS occurs as a difference between otherwise degenerate energy levels in the absence of an external magnetic field. It is of fundamental importance to understanding molecular magnetism. While ZFS parameters have been actively studied, there is still a limited understanding on how ZFS parameters relate to the geometric and electronic structures of transition metals compounds, including how metal-ligand bonding affects ZFS.[4,5,7] Knowledge of the effects of metal-ligand bonding on ZFS also helps design

better single molecular magnets (SMMs) as data storage and quantum computing materials.[8] The *D* parameter, which dominates magnetic anisotropy and the *E* parameter which relates to the quantum tunneling of magnetization in low symmetry compounds are key to tuning SMM properties.[8]

ZFS, including that of metalloporphyrins, has been investigated by several techniques, including electron paramagnetic resonance (EPR), magnetic susceptibility measurement, NMR, far-IR, Mössbauer spectroscopy, and magnetic circular dichroism (MCD).[1c,6,8,9] Inelastic neutron scattering (INS), to our knowledge, has not been used to investigate ZFS. It is, however, one of two techniques that *directly* give both the magnitude of the *D* parameter and often its sign.

Neutron scattering has been used to probe the magnetic properties of metal complexes.[4g] This is mainly because neutrons have a spin = ½ and a magnetic moment that can interact with unpaired electrons (spin = ½). When neutrons are scattered inelastically, they transfer energy to molecules in the sample, leading to transitions between molecular energy levels. INS has been used to probe the magnetic properties of metal complexes, especially excitations among low-lying energy levels in the molecules. In such a process, incident neutrons transfer energy to the molecules, leading to the magnetic excitations that are observed in an INS spectrum.[4g]

1.2. Understanding Intermolecular Interactions in the Solid State

In biological systems, metalloporphyrins are found in heme proteins. The diverse biological functions of heme proteins are often attributed to the varying degree of changes in the local heme environment.[1] For example, nitric oxide (NO) is a vital cellular signaling

agent in many physiological and pathological processes.[10] Its coordination to heme proteins is involved in several fundamental processes such as neuronal communication,[11] muscle relaxation,[12] platelet deaggregation,[13] and myocardial function.[14] A key structural feature of the O_2-free hemes in hemoglobin and myoglobin is that the active center contains a five-coordinate Fe-porphyrin. Five-coordinate Fe-porphyrin systems[15-17] such as [Fe(TPP)Cl] (**1**) (TPP^{2-} = *meso*-tetraphenylporphyrinate, Figure 1.1) have thus been actively studied to provide insight into the physical and chemical properties of the hemes.[18-24]

The exact crystal structure of [Fe(TPP)Cl] (**1**) is not clear. The first reported crystal structure of **1** was incorrectly solved as [Fe(TPP)(OH)]·(H_2O) in the *I*4 space group.[18a] This structure was re-analyzed by Hoard *et al*. in the higher symmetry *I*4/*m* space group as [Fe(TPP)Cl] (**1**).[18b] Monoclinic [Fe(TPP)Cl] (**1**) crystals in the $P2_1/n$ space group were obtained by Scheidt *et al*. through decomposition of [Fe(TPP)(NO)] (**5**) in a CH_2Cl_2 solution containing nitrate and nitrite ions.[23] A structure of [Fe(TPP)Cl] (**1**) at 100 K, in the *I*4/*m* space group, was solved by Scheidt and coworkers.[25] Most recently [Fe(TPP)Cl] (**1**) at 293 K was refined in the *I*4 space group by Hadjikakou *et al*. with two superimposed independent molecules having different distances of the Fe atom to the plane defined by the four N atoms of the porphyrin.[26]

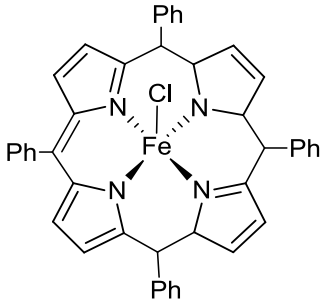

Figure 1.1. [Fe(TPP)Cl] (**1**).

Hirshfeld surface analysis, recently developed by Spackman and coworkers, allows for the comparison of molecular structures by examining interactions of an individual molecule with its nearest neighbor molecules while maintaining a whole-of-molecule approach.[27-29] A Hirshfeld surface is an isosurface calculated from the weight function $w(\boldsymbol{r})$ of the sum of spherical atom electron densities (Eq. 1.2);

$$w(\boldsymbol{r}) = \frac{\rho_{promolecule}(\boldsymbol{r})}{\rho_{procrystal}(\boldsymbol{r})} = \sum_{A \in molecule} \rho_A(\boldsymbol{r}) / \sum_{A \in crystal} \rho_A(\boldsymbol{r}) \qquad \text{(Eq. 1.2)}$$

where $\rho_{\text{promolecule}}(\boldsymbol{r})$ is the sum of the molecular electron density over the atoms in the molecule of interest (the promolecule) and $\rho_{\text{procrystal}}(\boldsymbol{r})$ is the similar sum over the crystal (the procrystal).[27-29]

The isosurface separates a molecule (promolecule) from its nearest neighbors (procrystal) at a given density level. From the Hirshfeld surface, distances to the nearest atoms outside (external), d_e, and inside (internal), d_i, are readily defined, and the surface gives a visual 3-*D* representation of the intermolecular close contacts in the crystal. Using the d_e,d_i pairs, the Hirshfeld surface can be reduced to a 2-*D* histogram, giving a unique fingerprint plot for molecular interactions in the crystal.[28,29] Void volumes in the crystal can be readily determined using the same isosurfaces of electron density, by looking at areas in the crystal where the electron density is the lowest.[30] Other earlier methods, in comparison, rely on the approximation of a molecule as a set of fused spheres with van der Waals radii and are thus limited in scope.[27-30] Hirshfeld surface analysis has been used to explore permanent voids, cavities, and channels in porous materials.[30] Hirshfeld

surface analysis is an excellent tool to compare compounds with respect to their molecular environment and interactions independent of the overall space group symmetry.

For example, the intermolecular interactions in squaraines were probed, shining light on how the π stacking in such dyes leads to semiconductor behavior in thin films.[31] Another example is spin crossover complexes, which can have large changes in their intermolecular interactions upon undergoing a spin change.[32]

1.3. Precursors to Metal Oxide Thin Films

Microelectronics is an integral part of modern society. Continued innovation in the microelectronic industry requires the use of new materials. For example, the gate insulator in transistors (Scheme 1.1), which acts a channel for the source and drain, has typically been SiO_2. However, with the continued decrease in transistor size dictated by Moore's law, SiO_2 becomes a poor insulator below a thickness of 2 nm.[33-40] This is due to the low dielectric constant of SiO_2 (k = 3.9) which allows current leakage below 2 nm.[33-40] In recent years, SiO_2 has been replaced by metal oxides such as HfO_2 and Ta_2O_5 that have high dielectric constants (k = 25 and 26, respectively).[40] The *Intel*®

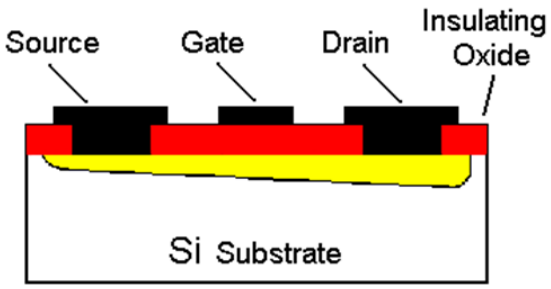

Scheme 1.1. A schematic of a transistor found in a microelectronic device.

Atom™ Processor and processors by Samsung and Apple are currently used in smartphones, SMART TVs, and tablet computers. They all contain HfO_2-based gate materials.

Metal oxide thin films for microelectronics are predominantly made using chemical vapor deposition (CVD) and atomic layer deposition (ALD).[41-45] CVD/ALD processes rely on the reactions between inorganic precursors and molecular oxygen or water. For CVD, these reactions take place in the gas phase making it difficult to determine the mechanism of the reactions. The inorganic precursors used to make metal oxide thin films in CVD/ALD processes are primarily d^0 metal complexes. In part due to the air-sensitive nature of d^0 metal complexes, their reactions with O_2 are not well understood.[46]

The reactions between O_2 and d^n middle and late transition metals typically involve metal oxidation.[47] For example, Kelley and Rohde in their studies of alkene oxygenation reactions were able to isolate and characterize an Ir(III) peroxo intermediate in the reaction between the [Ir^I{PhNC(NMe_2)NPh}(cod)] (cod = 1,5-cyclooctadiene) and O_2 (Scheme 1.2).[47j]

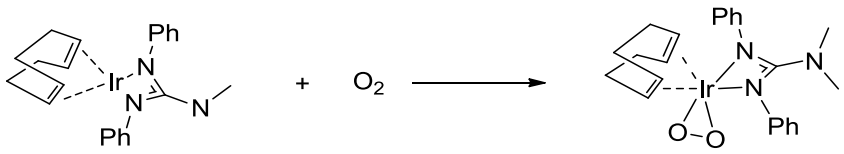

Scheme 1.2. Reaction of an Ir^I complex with O_2.[47]

For d^0 complexes there are very few reports on their reactions with O_2.[46] Since there are no valence d electrons in the d^0 complexes, the pathways in their reactions with O_2 are expected to be different from those of the reactions between d^n complexes and O_2. d^n complexes are usually oxidized in these reactions.

The majority of the reactions between d^0 complexes and O_2 in the literature involve oxygen insertion into metal alkyl bonds. For example, Schawrtz et al. reported oxygen insertion into the Zr-R bond in Cp_2ZrRCl to form $Cp_2Zr(OR)Cl$.[46c] Insertion of O_2 into the Zr-Si bond was observed in the reaction between O_2 and $Cp_2Zr(SiMe_3)Cl$.[46b]

Our group has reported the reaction between d^0 metal amides $M(NMe_2)_4$ (M = Zr, Hf) and O_2 with the formation of unusual trinuclear oxo aminoxide complexes $M_3(NMe_2)_6(\mu\text{-}NMe_2)_3(\mu_3\text{-}O)(\mu_3\text{-}ONMe_2)$ (M = Zr, Hf) (Scheme 1.3).[46n] Density functional theory calculations revealed the mechanistic pathways in the reactions of model complexes $Zr(NR_2)_4$ (R = H, Me) and $[Zr(NR_2)_4]_2$ (R = H, Me) with triplet O_2. Monomeric and dimeric reaction pathways were proposed.

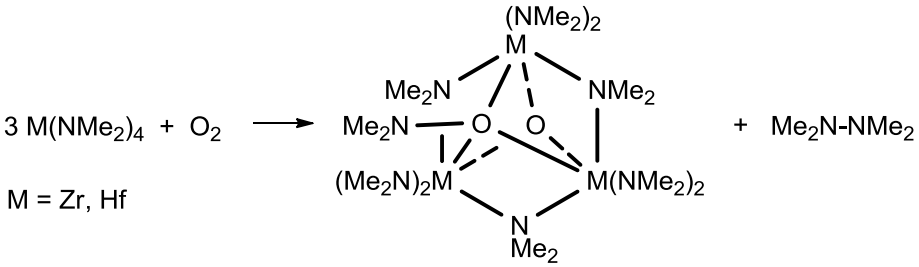

Scheme 1.3. Reactions of d^0 amides $M(NMe_2)_4$ with O_2.[46n]

Our group has also studied the reactions of Group 5 amides, $M(NMe_2)_5$ (M = Nb, Ta), with O_2 (Scheme 1.4).[46o,46p] $M(NMe_2)_5$ both give aminoxy monomer species

$(Me_2N)nM(\eta^2\text{-}ONMe_2)_{5-n}$ (M = Nb, Ta; n = 3, 4) and an oxo dimer $(Me_2N)_4M_2[\eta^2\text{-}N(Me)CH_2NMe_2]_2(\mu\text{-}O)_2$ (M = Nb, Ta). The reaction of the tantalum amide also gives the trinuclear species $(Me_2N)_6Ta_3[\eta^2\text{-}(N(Me)CH_2NMe_2]_2(\eta^2\text{-}ONMe_2)(\mu\text{-}O)_3$.

Our group has also studied the reactions between O_2 and d^0 complexes that contain guanidinate and amidinate ligands.[46x,46y] The amidinate and guanidinate ligands have been shown to stabilize complexes, making them better CVD and ALD precursors for microelectronic materials. Their reactions with O_2 give oxo complexes and polymers. Also, a rare peroxo complex, $\{(\mu\text{-}O_2)Zr[^i PrNC(Me)N^i Pr]_2\}_3$, was obtained from the reaction of O_2 with d^0 $(Me_2N)_2Zr[^i PrNC(Me)N^i Pr]_2$ (Scheme 1.5).[46y]

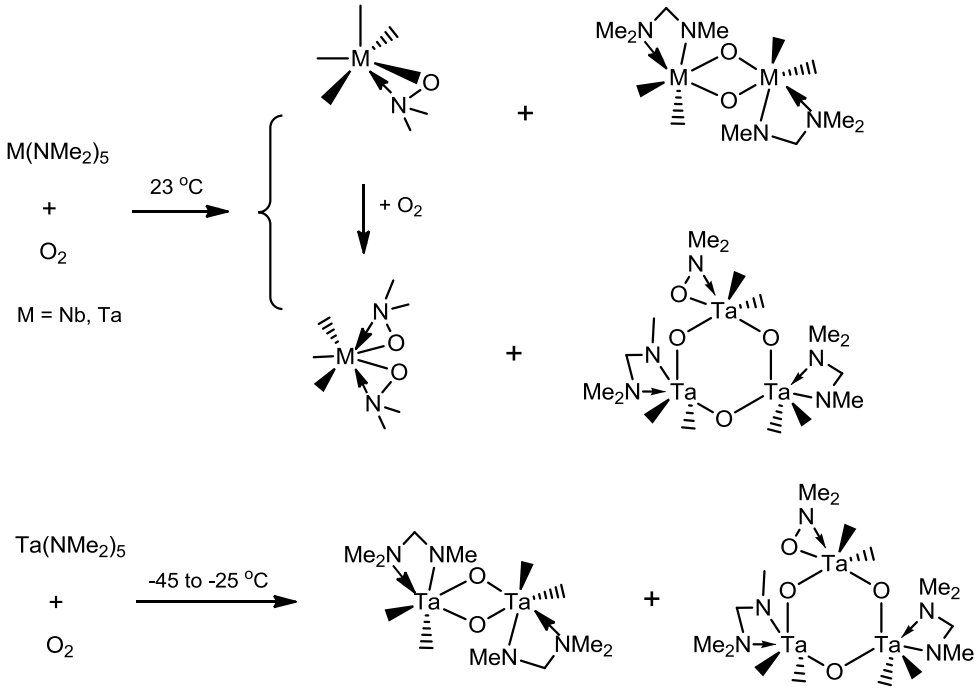

Scheme 1.4. Selective insertion in the reactions of $M(NMe_2)_5$ (M = Nb, Ta) with O_2.[46o,46p]

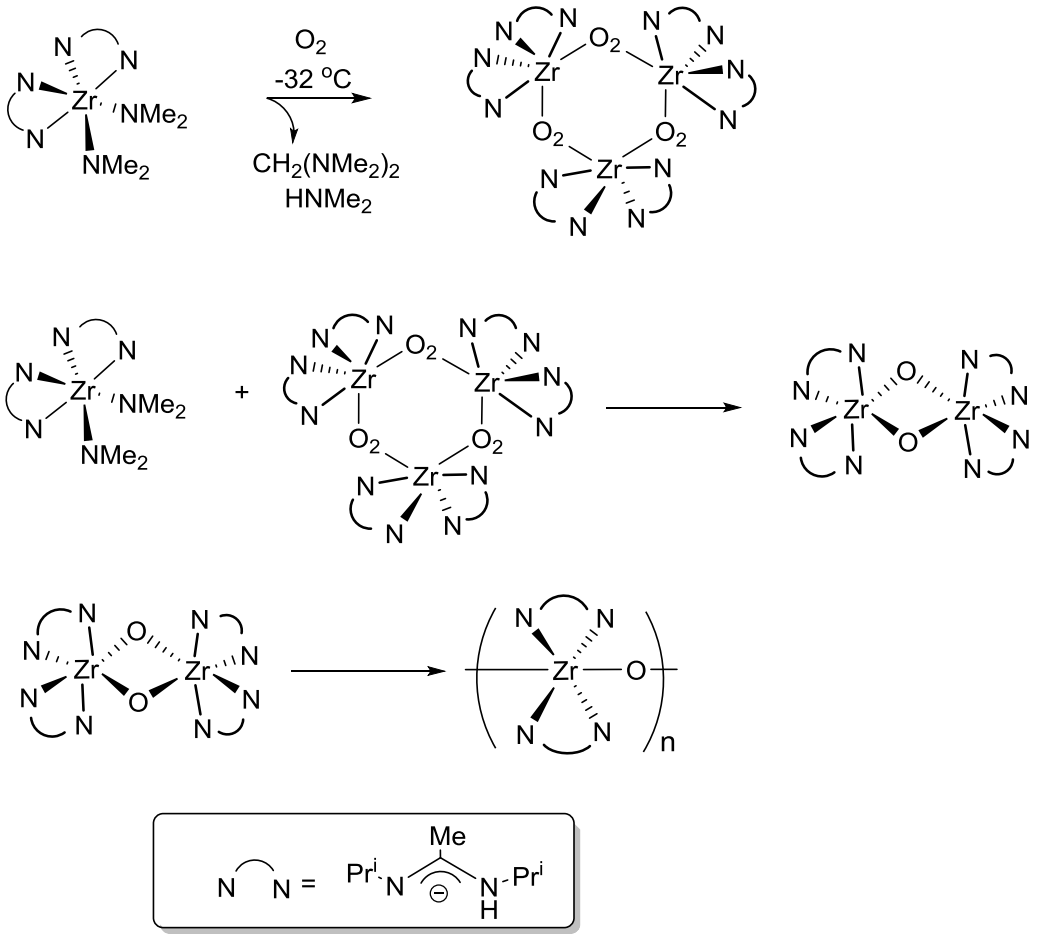

Scheme 1.5. Reactions between O_2 and d^0 amidinate amides yielding peroxo and oxo products.[46x,46y]

1.2. Current Dissertation

1.2.1. Part 2

Zero-field splitting (ZFS) parameters of several non-deuterated metalloporphyrins [M(TPP)Cl] (M = Fe, **1**; Mn, **2**; Cr, **3**) and [Mn(TPP)] (**4**) (TPP^{2-} = *meso*-tetraphenylporphyrinate) have been directly determined by inelastic neutron scattering (INS). The ZFS values are: D = 6.33(8) cm^{-1} for [Fe(TPP)Cl] (**1**), -2.24(3) cm^{-1} for [Mn(TPP)Cl] (**2**), 0.79(2) cm^{-1} for [Mn(TPP)] (**4**), and $|D|$ = 0.234(12) cm^{-1} for [Cr(TPP)Cl] (**3**). The work shows that compounds with magnetic excitations below ~30 cm^{-1} could be determined using non-deuterated samples. To our knowledge, this is the first use of INS to probe magnetic properties of biomimetic compounds.

1.2.2. Part 3

Variable-temperature (VT) crystal-structure study of [Fe(TPP)Cl] (**1**) and Hirshfeld surface analyses of its structures and previously published structures of [M(TPP)(NO)] (M = Fe, **5**; Co, **6**) reveal that intermolecular interactions are a significant factor in structure disorders in the three metalloporphyrins and phase changes in the nitrosyl complexes. These interactions cause, *e.g.*, an 8-fold disorder in the crystal structures of [M(TPP)(NO)] (**5**,**6**) at room temperature that obscures the M-NO binding. Hirshfeld analyses of the structure of [Co(TPP)(NO)] (**6**) indicate that the phase change from *I*4/*m* to *P*-1 leads to an increase in void-volume percentage, permitting additional structural compression through tilting of the phenyl rings to offset the close-packing interactions at the interlayer positions in the crystal structures with temperature decrease. X-ray and neutron structure studies of [Fe(TPP)Cl] (**1**) at 293, 143 and 20 K reveal a tilting of the

phenyl groups away from being perpendicular to the porphyrin ring as a result of intermolecular interactions. Structural similarities and differences among the three complexes are identified and described by Hirshfeld surface and void-volume calculations.

1.2.3. Part 4

The alkyl amide imide complexes $TaMe_2(=NSiMe_3)[N(SiMe_3)_2]$ (**9**) and $Ta(CH_2Ph)_2(=NSiMe_3)[N(SiMe_3)_2]$ (**10**) have been prepared from the reactions of $\{Ta(\mu\text{-}Cl)Cl(=NSiMe_3)[N(SiMe_3)_2]\}_2$ (**8**) with the appropriate organometallic reagents. **10** has been characterized by single-crystal X-ray diffraction and shows η^2 coordination of the phenyl ring on one of the benzyl ligands to the Ta center. The reaction of **9** and 0.5 equiv of O_2 leads to selective oxygen insertion into one Ta-Me bond, yielding an alkoxy bridged dimer $Ta_2(\mu\text{-}OMe)_2(=NSiMe_3)_2[N(SiMe_3)_2]_2Me_2$ as *cis*- and *trans*-isomers (***cis*-11** and ***trans*-11**). The ***trans*-11** isomer has been characterized by single-crystal X-ray diffraction. A mixture of ***cis*-11** and ***trans*-11** in benzene-d_6 was found to react with additional O_2 to give $\{Ta(\mu\text{-}OMe)(OMe)(=NSiMe_3)[N(SiMe_3)_2]\}_2$.

1.2.4. Part 5

Mixed amide imide compounds $Ta(NR_2)_2(=NSiMe_3)[N(SiMe_3)_2]$ (R = Me, **12**; Et, **13**) have been prepared by two different salt metathesis reactions from $TaCl_3[N(SiMe_3)_2]_2$ (**7**) or $\{Ta(\mu\text{-}Cl)Cl(=NSiMe_3)[N(SiMe_3)_2]\}_2$ (**8**). The pathway from **7** eliminates $Me_3Si\text{-}NR_2$ (R = Me or Et), converting the amide $N(SiMe_3)_2$ ligand to the imide $=NSiMe_3$ ligand. Such intramolecular imidations are rare. The mechanism of this process has been probed.

1.2.5. Part 6

A summary of the research in this dissertation is presented as well as suggested future work.

References

1. (a) *The Porphyrin Handbook*, Kadish, K. M.; Smith, K. M.; Guilard, R., Eds, 2000-2003, Academic Press, San Diego. (b) *Handbook of Porphyrin Science with Applications to Chemistry, Physics, Materials Science, Engineering, Biology and Medicine*, Kadish, K. M.; Smith, K. M., Guilard, R., Eds., 2010, World Scientific, Singapore. (c) *The Porphyrins*, Dolphin, D., Ed., 1978-1979, Academic Press, New York: Walker, F. A. Vol. 5, Ch. 36, pp. 81-183; La Mar, G. N.; Satterlee, J. D.; De Ropp, J. S. Vol. 5, Ch. 37, pp. 185-298; Cheek, J.; Dawson, J.H. Vol. 7, Ch. 53, pp. 339-369.
2. For geochemistry of porphyrins, See, e,g., Callot, H. J.; Ocampo, R., 2000, in Ref. 1a, Vol. 1, Ch. 7, pp. 349-398.
3. (a) Collman, J. P.; Boulatov, R.; Sunderland, C. J.; Fu, L. *Chem. Rev.* **2004**, *104*, 561. (b) Hoffman, B. M. *Proc. Nat. Acad. Sci. USA* **2003**, *100*, 3575. (c) Yang, F.; Shokhireva, T. K.; Walker, F. A. *Inorg. Chem.* **2011**, *50*, 1176. (d) Scheidt, W. R.; Barabanschikov, A.; Pavlik, J. W.; Silvernail, N. J.; Sage, J. T. *Inorg. Chem.* **2010**, *49*, 6240. (e) Decker, A.; Solomon, E. I. *Angew. Chem., Int. Ed.* **2005**, *44*, 2252. (f) de Visser, S. P.; Valentine, J. S. V.; Humphreys, K. J. *Pure Appl. Chem.* **1998**, *70*, 855. (g) Brand, H.; Arnold, J. *Coord. Chem. Rev.* **1995**, *140*, 137. (h) Fujii, H. *Coord. Chem. Rev.* **2002**, *226*, 51. (h) Richter-Addo, G. B. *Acc. Chem. Res.* **1999**, *32*, 529. (i) Zhang, P.; Wang, M.; Li, X. Qiang; C., Hong G.; Dong, J. F.; Sun, L. C. *Sci. China Chem.* **2012**, *55*, 1274.
4. (a) Boca, R. *Coord. Chem.* **2004**, *248*, 757. (b) Neese, F.; Solomon, E. I. in: Miller, J. S., Drillon, M. (Eds) *Magnetism* Vol. IV, Wiley-VCH, 2003, pp. 345-466. (c) Long,

J. R., in *Chemistry of Nano-structured Materials*; Yang, P., Ed.; World Scientific: Hong Kong, 2003; pp. 291-315. (d) Misra, S. K., in *Multifrequency Electron Paramagnetic Resonance*, Wiley-VCH: 2011; pp. 589-597. (e) McInnes, E. L., in *Single-Molecule Magnets and Related Phenomena*, Winpenny, R., Ed. Springer: 2006; Vol. 122, pp. 69-102. (f) Krzystek, J.; Ozarowski, A.; Telser, J. *Coord. Chem. Rev.* **2006**, *250*, 2308. (g) Gatteschi, D. *J. Phys. Chem. B* **2000**, *104*, 9780. (h) Reiff, W. M. *ACS Symp. Ser.* **1996**, 644, 115.

5. (a) Yoon, J.; Mirica, L. M.; Stack, T. D. P.; Solomon, E. I. *J. Am. Chem. Soc.* **2004**, *126*, 12586. (b) Her, J.-H.; Stephens, P. W.; Kennon, B. S.; Liu, C.; Miller, J. S. *Inorg. Chim. Acta* **2010**, *364*, 172. (c) Reisner, E.; Telser, J.; Lippard, S. J. *Inorg. Chem.* **2007**, *46*, 10754. (d) Krzystek, J.; Telser, J.; Pardi, L. A.; Goldberg, D. P.; Hoffman, B. M.; Brunel, L.-C. *Inorg. Chem.* **1999**, *38*, 6121. (e) Godwin, H. A.; Collman, J. P.; Marchon, J.-C.; Maldivi, P.; Yee, G. T.; Conklin, B. J. *Inorg. Chem.* **1997**, *36*, 3499. (f) Holman, T. R.; Juarez-Garcia, C.; Hendrich, M. P.; Que, Jr., L.; Miinck, E. *J. Am. Chem. Soc.* **1990**, *112*, 7611. (g) Schulz, C. E.; Song, H.; Mislankar, A.; Orosz, R. D.; Reed, C.A.; Debrunner, P. G.; Scheidt, W.R. *Inorg. Chem.* **1997**, *36*, 406. (h) Miyasaka, H.; Clérac, R.; Campos-Fernández, C. S.; Dunbar, K. R. *J. Chem. Soc., Dalton Trans.* **2001**, 858. (i) Ma, L.-H.; Liu, Y.; Zhang, X.; Yoshida, T.; Langry, K. C.; Smith, K. M.; La Mar, G. N. *J. Am. Chem. Soc.* **2006**, *128*, 6391. (j) Reynolds, P.A.; Moubaraki, B.; Murray, K.S.; Cable, J.W.; Engelhardt, L.M.; Figgis, B.N. *J. Chem. Soc., Dalton Trans.* **1997**, 263.

6. Browett, W. R.; Fucaloro, A. F.; Morgan, T. V.; Stephens, P. J. *J. Am. Chem. Soc.* **1983**, *105*, 1868.

7. Deaton, J. C.; Gebhard, M. S.; Solomon, E. I. *Inorg. Chem.* **1989**, *28*, 877.

8. Gatteschi, D.; Sessoli, R. *Angew Chem. Int. Ed.* **2003**, *42*, 268.

9. (a) *Magnetism: Molecules to Materials*; Miller, J.S.; Drillon, M., Eds.; Wiley-VCH, 2002. (b) *Applications of Physical Methods to Inorganic and Bioinorganic Chemistry*; Scott, R.A.; Lukehart, C.M., Eds.; Wiley, 2007, including Larese, J. Z., pp. 291-313

10. (a) Moncada, S.; Palmer, R. M.; Higgs, E. A. *Pharmacol. Rev.* **1991**, *43*, 109. (b) Ignarro, L.: *Nitric Oxide: Biology and Pathobiology*; Academic Press: San Diego, 2000. (c) Lehnert, N.; Berto, T. C.; Galinato, M. G. I.; Goodrich, L. E. *The Role of Heme-Nitrosyls in the Biosynthesis, Transport, Sensing, and Detoxification of Nitric Oxide (NO) in Biological Systems: Enzymes and Model Complexes*. In *The Handbook of Porphyrin Science*; Kadish, K. M., Smith, K. M., Guilard, R., Eds.; World Scientific: Hackensack, NJ, 2011; Vol. 14; Chap. 63, pp 1−247. (d) Goodrich, L. E.; Paulat, F.; Praneeth, V. K. K.; Lehnert, N. *Inorg. Chem.* **2010**, *49*, 6293. (e) Straub, A. C.; Lohman, A. W.; Billaud, M.; Johnstone, S. R.; Dwyer, S. T.; Lee, M. Y.; Bortz, P. S.; Best, A. K.; Columbus, L.; Gaston, B.; Isakson, B. E. *Nature*, **2012**, *491*, 473. (f) Gladwin, M. T.; Kim-Shapiro, D. B. *Nature*, **2012**, *491*, 344. (g) Silvernail, N. J.; Olmstead, M. M.; Noll, B. C.; Scheidt, W. R. *Inorg. Chem.* **2009**, *48*, 971. (h) Zheng, H. W.; Wang, R. B.; Qiao, L. K.; Du, Y. *Sci. China Technol. Sci*. **2014**, *57*, 857.

11. (a) Wang, H.; Zhong, F.; Pan, J.; Li, W.; Su, J.; Huang, Z.-X.; Tan, X., *J. Biolog. Inorg. Chem.* **2012**, *17*, 719. (b) Garthwaite, J. *Trends Neurosci.* **1991**, *14*, 60.

12. (a) Fritz, B. G.; Roberts, S. A.; Ahmed, A.; Breci, L.; Li, W.; Weichsel, A.; Brailey, J. L.; Wysocki, V. H.; Tama, F.; Montfort, W. R. *Biochemistry* **2013**, *52*, 156. (b) Rapoport, R. M.; Murad, F. *Circ. Res.* **1983**, *52*, 352. (c) Ignarro, L. J.; Adams, J. B.; Horwitz, P. M.; Wood, K. S. *J. Biol. Chem.* **1986**, *261*, 4997.
13. (a) Azuma, H.; Ishikawa, M.; Sekizaki, S. *Br. J. Pharmacol.* **1986**, *88*, 411. (b) Furlong, B.; Henderson, A. H.; Lewis, M. J.; Smith, J. A. *Br. J. Pharmacol.* **1987**, *90*, 687.
14. (a) Campbell, M. G.; Underbakke, E. S.; Potter, C. S.; Carragher, B.; Marletta, M. A. *Proc. Natl. Acad. Sci. USA* **2014**, *111*, 2960. (b) Ursu, O. N.; Sauter, M.; Ettischer, N.; Kandolf, R.; Klingel, K. *Cell. Physiol. Biochem.* **2014**, *33*, 52.
15. Behere, D. V.; Birdy, R.; Mitra, S. *Inorg. Chem.* **1982**, *21*, 386.
16. D'Angelo, P.; Lapi, A.; Migliorati, V.; Arcovito, A.; Benfatto, M.; Roscioni, O. M.; Meyer-Klaucke, W.; Della-Longa, S. *Inorg. Chem.* **2008**, *47*, 9905.
17. Scheidt, W. R.; Gouterman, M. in *Iron Porphyrins, Part One*, edited by A. B. P. Lever & H. B. Gray, Addison-Wesley, Reading, MA: 1983, pp. 89-139.
18. (a) Fleischer, E. B.; Miller, C. K.; Webb, L. E. *J. Am. Chem. Soc.* **1964**, *86*, 2342. (b) Hoard, J. L.; Cohen. G. H.; Glick, M. D. *J. Am. Chem. Soc.* **1967**, *89*, 1992.
19. Eaton, D. R.; LaLancette, E. A. *J. Chem. Phys.* **1964**, *41*, 3534.
20. Collman, J. P.; Hoard, J. L.; Kim, N.; Lang, G.; Reed, C. A. *J. Am. Chem. Soc.* **1975**, *97*, 2676.
21. Cheng, R. J.; Chen, P. Y.; Lovell, T.; Liu, T.; Noodleman, L.; Case, D. A. *J. Am. Chem. Soc.* **2003**, *125*, 6774.
22. Mao, J.; Zhang, Y.; Oldfield, E. *J. Am. Chem. Soc.* **2002**, *124*, 13911.

23. (a) Scheidt, W. R.; Finnegan, M. G. *Acta Cryst.* **1989**, *C45*, 1214. (b) Finnegan, M. G.; Lappin, A. G.; Scheidt, W. R. *Inorg. Chem.* **1990**, *29*, 181.
24. Hunter, S. C.; Podlesnyak, A. A.; Xue, Z. L. *Inorg. Chem.* **2014**, *53*, 1955.
25. Grande, L. M.; Noll, B. C.; Oliver, A. G.; Scheidt, W. R. *Inorg. Chem.* **2010**, *49*, 6552.
26. Corban, G.J.; Hadjikakou, S. K.; Tsipis, A. C.; Kubicki, M.; Bakas, T.; Hadjiliadis, N. *New J. Chem.* **2011**, *35*, 213.
27. Spackman, M. A.; Jayatilaka, D. *CrystEngComm* **2009**, *11*, 19.
28. Spackman, M. A.; McKinnon, J. J. *CrystEngComm* **2002**, *4*, 378.
29. McKinnon, J. J.; Jayatilaka, D.; Spackman, M. A. *Chem. Commun.* **2007**, 3814.
30. Turner, M. J.; McKinnon, J. J.; Jayatilaka, D.; Spackman, M. A. *CrystEngComm* **2011**, *13*, 1804.
31. Gsänger, M.; Kirchner, E.; Stolte, M.; Burschka, C.; Stepaneko, V.; Pflaum, J.; Würthner, F. *J. Am. Chem. Soc.* **2014**, *136*, 2351.
32. Guionneau, P. *Dalton Trans.* **2014**, *43*, 382.
33. Rockett, A. The Materials Science of Semiconductors, Springer Science+Business Media, LLC, New York, 2008.
34. Smith, R. C.; Ma, T.; Hoilien, N.; Tsung, L. Y.; Bevan, M. J.; Colombo, L.; Roberts, J.; Campbell, S. A.; Gladfelter, W. L. *Adv. Mater. Opt. Electron* **2000***, 10,* 105*.*
35. Wallace, R.; Wilk, G. D. *Crit. Rev. Solid State Mater. Sci.* **2003***, 28,* 231*.*
36. Wilk, G. D.; Wallace, R. M.; Anthony, J. M. *J. Appl. Phys.* **2001***, 89,* 5243*.*
37. Robertson*,* J. *Rep. Prog. Phys.* **2006**, *69*, *327.*
38. Arghavani, R.; Miner, G.; Agustin, M. *Semicond. Internal.* 2007, **30***,* 32*.*

39. Jones, A. C.; Aspinall, H. C.; Chalker, P. R.; Potter, R. J.; Kukli, K.; Rahtu, A.; Ritala, M.; Leskelae, M. *J. Mater. Chem*. **2004**, *14,* 3101.

40. Wallace, R.; Wilk, G. D. *MRS Bull*. **2002**, *27*, 192.

41. Campbell, S. A. *Science and Engineering of Microelectronic Fabrication,* ed. A. S. Sedra, Oxford University Press, Oxford, 2nd Ed., 2001.

42. Panda, D.; Tseng, T. –Y. *Thin Solid Films* **2013***, 531,* 1**.**

43. (a) Hitchman, M. L.; Jenson, K. F. *Chemical Vapor Deposition: Principles and Applications*. eds. Hitchman, M. L.; Jenson, K. F. Academic Press Ltd. London, UK, 1993, 1. (b) Jenson, K. F. *Chemical Vapor Deposition: Principles and Applications*. eds. Hitchman, M. L.; Jenson, K. F. Academic Press Ltd. London, UK, 1993, 31.

44. Pierson, H. O. *Handbook of Chemical Vapor Deposition: Principles, Technology, and Applications.* eds. Bunshah, R. F.; McGuire, G. E.; Rossnagel, S. M. Noyes Publications, Park Ridge, New Jersey,1992.

45. *Vapor Deposition*, eds. Powell, C. F.; Oxley, J. H.; Blocher, J. M. The Electrochemical Society, New York, 1966.

46. (a) Stanciu, C.; Jones, M. E.; Fanwick, P. E.; Abu-Omar, M. M. *J. Am. Chem. Soc.* **2007**, *129*, 12400. (b) Tilley, T. D. *Organometallics*, **1985**, *4*, 1452. (c) Blackburn, T. F.; Labinger, J. A.; Schwartz, J. *Tetrahedron Lett.* **1975**, *16*, 3041. (d) Lubben, T. V.; Wolczanski, P. T. *J. Am. Chem. Soc.* **1987**, *109*, 424. (e) Wang, R.; Folting, K.; Huffman, J. C.; Chamberlain, L. R.; Rothwell, I. P. *Inorg. Chim. Acta* **1986**, *120*, 81. (f) Gibson, V. C.; Redshaw, C.; Walker, G. L. P.; Howard, J. A. K.; Hoy, V. J.; Cole, J. M.; Kuzmina, L. G.; De Silva, D. S. *Dalton Trans.* **1999**, 161. (g)

Schaverien, C. J.; Orpen, A. G. *Inorg. Chem.* **1991**, *30*, 4968. (h) Liu, X.; Cui, D. *Dalton Trans.* **2008**, 3747. (i) Van Asselt, A.; Trimmer, M. S.; Henling, L. M.; Bercaw, J. E. *J. Am. Chem. Soc.* **1988**, *110*, 8254. (j) Brindley, P. B.; Hodgson, J. C. *J. Organomet. Chem.* **1974**, *65*, 57. (k) Boro, B. J.; Lansing, R.; Goldberg, K. I.; Kemp, R. A. *Inorg. Chem. Commun.* **2011**, *14*, 531. (l) Lu, F.; Zarkesh, R. A.; Heyduk, A. F. *Eur. J. Inorg. Chem.* **2012**, *3*, 467. (m) Chisholm, M. H.; Hammond, C. E.; Huffman, J. C. *Chem. Commun.* **1987**, 1423. (n) Wang, R.-T.; Zhang, X.-H.; Chen, S.-J.; Yu, X.-H.; Wang, C.-S.; Beach, D. B.; Wu, Y.-D.; Xue, Z.-L. *J. Am. Chem. Soc.* **2005**, *127*, 5204. (o) Chen, S.-J.; Zhang, X.-H.; Yu, X.; Qiu, H.; Yap, G. P. A.; Guzei, I. A.; Lin, Z.; Wu, Y. D.; Xue, Z.-L. *J. Am. Chem. Soc.* **2007**, *129*, 14408. (p) Chen, S.-J.; Zhang, J.; Yu, X.; Bu, X.; Chen, X.-T.; Xue, Z.-L. *Inorg. Chem.* **2010**, *49*, 4017. (q) Morton, L. A.; Miao, M.; Callaway, T. M.; Chen, T.; Chen, S.-J.; Tuinman, A. A.; Yu, X.-H.; Lu, Z.; Xue, Z.-L. *Chem. Commun.* **2013**, *49*, 9555. (r) Chen, T.-N.; Zhang, X.-H.; Wang, C.-S.; Chen, S.-J.; Wu, Z.-Z.; Li, L.-T.; Sorasaenee, K. R.; Diminnie, J. B.; Pan, H.-J.; Guzei, I. A.; Rheingold, A. L,; Wu, Y.-D.; Xue, Z.-L. *Organometallics* **2005**, *24*, 1214. (s) Qiu, H.; Chen, S.-J.; Wang, C.-S.; Wu, Y.-D.; Guzei, I. A.; Chen, X.-T.; Xue, Z.-L. *Inorg. Chem.* **2009**, *48*, 3073. (t) Yu, X.; Chen, X.-T.; Xue, Z.-L. *Organometallics* **2009**, *28*, 6642. (u) Chen, S.-J.; Yap, G. P. A.; Xue, Z.-L. *Sci. China: Chem.* **2009**, *52*, 1583. (v) Chen, S.-J.; Zhang, X.-H.; Lin, Z.; Wu, Y.-D.; Xue, Z.-L. *Sci. China: Chem.* **2009**, *52*, 1723. (w) Chen, S.-J.; Xue, Z.-L. *Organometallics* **2010**, *29*, 5579. (x) Sharma, B.; Callaway, T. M.; Lamb, A. C.; Steren, C. A.; Chen, S.-J.; Xue, Z.-L. *Inorg. Chem.*

2013, *52*, 11409. (y) Lamb, A. C.; Lu, Z.; Xue, Z.-L. *Chem. Commun.* **2014**, *50*, 10517.

47. (a) Que, L.; Tolman, W. B. *Nature* **2008**, *455*, 333. (b) Yokoyama, A.; Han, J. E.; Cho, J.; Kubo, M.; Ogura, T.; Siegler, M. A.; Karlin, K. D.; Nam, W. *J. Am. Chem. Soc.* **2012**, *134*, 15269. (c) Campbell, A. N.; Stahl, S. S. *Acc. Chem. Res.* **2012**, *45*, 851. (d) Shook, R. L.; Borovik, A. S. *Chem. Commun.* **2008**, 6095. (e) Monillas, W. H.; Yap, G. P. A.; MacAdams, L. A.; Theopold, K. H. *J. Am. Chem. Soc.* **2007**, *129*, 8090. (f) McQuilken, A. C.; Jiang, Y.; Siegler, M. A.; Goldberg, D. P. *J. Am. Chem. Soc.* **2012**, *134*, 8758. (g) Scheuermann, M. L.; Fekl, U.; Kaminsky, W.; Goldberg, K. I. *Organometallics* **2010**, *29*, 4749. (h) Khusnutdinova, J. R.; Rath, N. P.; Mirica, L. M. *J. Am. Chem. Soc.* **2012**, *134*, 2414. (i) Nguyen, K. T.; Rath, S. P.; Latos-Grazynski, L.; Olmstead, M. M.; Balch, A. L. *J. Am. Chem. Soc.* **2004**, *126*, 6210. (j) Kelley, M. R.; Rohde, J.-U. *Chem. Commun.* **2012**, *48*, 2876. (k) Frisch, J. R.; McDonnell, R.; Rybak-Akimova, E. V.; Que Jr., L. *Inorg. Chem.* **2013**, *52*, 2627.

48. Bergman, J. G.; Cotton, F. A. *Inorg. Chem.* **1966**, *5*, 1208.

Part 2

Magnetic Excitations in Metalloporphyrins by Inelastic Neutron Scattering. Determination of Zero-Field Splittings in Iron, Manganese and Chromium Complexes

This part is based on the following paper:

Hunter, S. C.; Podlesnyak, A. A.; Xue. Z.-L., Magnetic Excitations in Metalloporphyrins by Inelastic Neutron Scattering. Determination of Zero-Field Splittings in Iron, Manganese and Chromium Complexes. *Inorganic Chemistry* **2014**, *53*, 1955.

Abstract

Zero-field splitting (ZFS) parameters of several non-deuterated metalloporphyrins [M(TPP)Cl] (M = Fe, **1**; Mn, **2**; Cr, **3**) and [Mn(TPP)] (**4**) (TPP^{2-} = *meso*-tetraphenylporphyrinate) have been directly determined by inelastic neutron scattering (INS). The ZFS values are: D = 6.33(8) cm^{-1} for [Fe(TPP)Cl] (**1**), -2.24(3) cm^{-1} for [Mn(TPP)Cl] (**2**), 0.79(2) cm^{-1} for [Mn(TPP)] (**4**), and $|D|$ = 0.234(12) cm^{-1} for [Cr(TPP)Cl] (**3**). The work shows that compounds with magnetic excitations below ~30 cm^{-1} could be determined using non-deuterated samples.

2.1. Introduction

Metalloporphyrins are an important class of compounds, and they are found in both biological and geological systems.[1-3] Magnetic properties of paramagnetic metalloporphyrins, those with unpaired electrons, have been actively studied.[1c] One intrinsic magnetic property is the zero-field splitting (ZFS). For paramagnetic compounds with spin $S \geq 1$, there lies a splitting of the spin states of otherwise degenerate states as a result of the interaction of the electron spins mediated by the spin-orbital coupling.[4-6] The spin-Hamiltonian is given in Eq. 2.1.

$$\widehat{H}_s = D\left[\hat{S}_z^2 - \frac{1}{3}S(S+1)\right] + E[\hat{S}_x^2 - \hat{S}_y^2] \qquad \text{(Eq. 2.1)}$$

where *D* and *E* are the axial and rhombic ZFS parameters, respectively.

ZFS appears as small differences (usually a few cm^{-1}) among energy levels in the absence of an external magnetic field, and it is represented by the *D* and *E* parameters (Eq. 2.1). ZFS of single molecular magnets (SMMs) has been actively studied, as the *D* values are critical for their potential applications for, e.g., as new data storage materials.[7] ZFS, including those of metalloporphyrins, has been investigated using electron paramagnetic resonance (EPR), magnetic susceptibility, NMR, far-IR, Mössbauer, magnetic circular dichroism (MCD), and inelastic neutron scattering (INS).[1c,6-8] Among these techniques, INS is one of few that directly give both the magnitude of the *D* parameter and often its sign.

When a sample is placed in an incident neutron beam, neutrons may scatter by the sample elastically and inelastically. When neutrons are scattered inelastically, they

transfer energy to molecules in the sample, leading to transitions between molecular energy levels. INS has been used to study dynamics of molecules such as rotational motion of H_2 ligands.[9] It has also been used to probe the magnetic properties of metal complexes, especially excitations among low-lying energy levels. In such a process, incident neutrons transfer energy to the molecules, leading to the magnetic excitations that are observed in an INS spectrum.[4g] For example, the low-lying energy levels of magnetic clusters have been characterized by INS.[4g,10] Güdel and coworkers have determined *D* for single-molecule magnets $[Mn_4O_3X(OAc)_3(dbm)_3]$ (X = Br^-, Cl^-, OAc^-, and F^-) and studied how the *D* values change with the axial X^- ligands.[11a] Chaboussant, Christou, and Lechner have found out that reduction of the Mn_{12} cluster $[Mn_{12}O_{12}(O_2CC_6F_5)_{16}(H_2O)_4]$ suppresses the axial ZFS parameter *D*.[11b]

To our knowledge, few bioinorganic complexes have been studied by inelastic neutron scattering (INS). Traditionally neutron scattering studies have been conducted using deuterated samples, as D atoms have smaller incoherent scattering of neutrons than H atoms, reducing the background noise.[12] The Spallation Neutron Source (SNS) recently constructed at Oak Ridge National Laboratory (ORNL) in the USA provides the most intense pulsed neutron beams in the world for scientific research. State-of-the-art experimental stations at SNS have made it possible to probe magnetic properties of non-deuterated metal complexes in detail.[11h] We have used the Cold Neutron Chopper Spectrometer (CNCS)[13] at SNS to determine the *D* parameters for the non-deuterated metalloporphyrins [M(TPP)Cl] (H_2TPP = *meso*-tetraphenylporphyrin, M = Fe^{III}, **1**; Mn^{III}, **2**; and Cr^{III}, **3**) and [Mn(TPP)] (**4**). Our results are reported here.

Molecules of the complexes in the current studies have 4-fold symmetry (Scheme 2.1). If their crystals have a 4-fold symmetry as well in, e.g., a tetragonal space group, the spin-Hamiltonian in Eq. 2.1 is simplified into Eq. 2.2.

$$\widehat{H}_S = D\left[\hat{S}_z^2 - \tfrac{1}{3}S(S+1)\right] \qquad \text{(Eq. 2.2)}$$

In the absence of a magnetic field, electronic ground states of complexes with S = 5/2, 2, 3/2 and 1 are split (Scheme 2.2), as a result of ZFS by the combined effect of the spin-orbital coupling and the axial ligand field.[6]

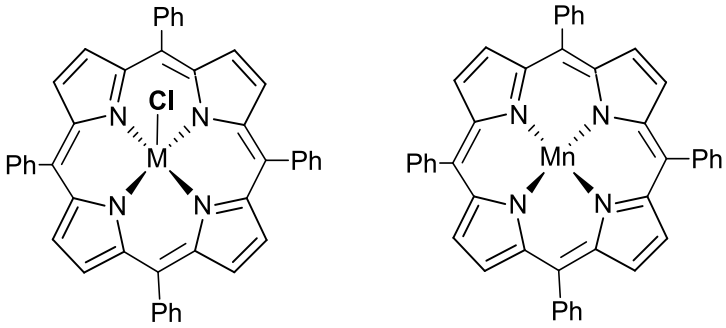

M = Fe, **1**; Mn, **2**; Cr, **3** **4**

Scheme 2.1. Structures of metalloporphyrins in the current studies.

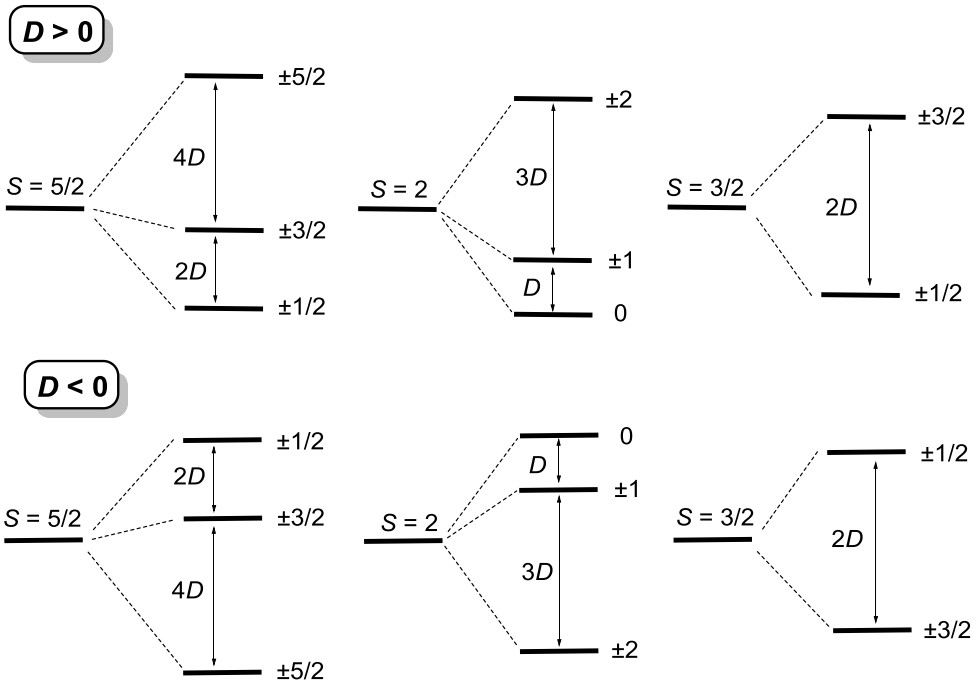

Scheme 2.2. Zero-field splittings (ZFS) in compounds with S = 5/2, 2 and 3/2. Top: D > 0; Bottom: D < 0.

2.2. Experimental Section

[Fe(TPP)Cl] (**1**) (Strem Chemicals, Lot# 19089600), [Mn(TPP)Cl] (**2**) (Sigma Aldrich, Lot# 01909MEV), and [Cr(TPP)Cl] (**3**) (Strem Chemicals; Lot# 21803900) were used as received. [Mn(TPP)] (**4**) was prepared through the reduction of [Mn(TPP)Cl] (**2**) by $NaBH_4$ by the literature methods.[14] The identities and purities of the samples were confirmed by UV-visible spectroscopy.[6,14,15]

The solid samples were characterized by powder X-ray diffraction. Suitable polycrystalline samples of the air-stable complexes [Fe(TPP)Cl] (**1**), [Mn(TPP)Cl] (**2**), and [Cr(TPP)Cl] (**3**) were placed on a zero-background plate sample holder. Air-sensitive [Mn(TPP)] (**4**) was placed on an air-sensitive sample holder with a zero background plate. The sample was covered with a 14 gauge DuPont Mylar C film.

Powder diffraction patterns were obtained on the PANalytical Empyrean diffractometer using Cu K_α radiation (λ = 1.5418 Å). Analysis and unit cell determination were performed using the PANalytical HighScore Plus analysis software and the McMaille method.[16] Diffraction patterns of [Fe(TPP)Cl][17] (**1**) and [Mn(TPP)Cl][18] (**2**) were matched to simulated diffraction patterns from their single crystal X-ray diffraction data.

The INS measurements were carried out on the CNCS at the SNS, Oak Ridge National Laboratory. The CNCS is a direct geometry, time-of-flight spectrometer that receives a beam from a coupled cryogenic H_2 moderator. For energy selection, the CNCS employs four chopper assemblies. The speeds and slit widths of the choppers can be varied, allowing adjustments in the instrumental resolution and intensity of the incident beam. Approximately 500 mg of each sample was loaded into 1/2 inch thick aluminum tubes and sealed under a helium atmosphere. The sample was mounted in a standard liquid helium cryostat with a base temperature of T = 1.5 K. An oscillating radial collimator was used to reduce background scattering from the tail of the cryostat. Vanadium was used as a standard for the detector efficiency correction.

The incident neutron energy for every measurement was chosen to cover the anticipated region of interest in both the energy *E* and scattering-vector *Q* space. The small incident energy is especially important to observe excitations near the elastic peak (at energy transfer = 0 cm^{-1}) as the full-width-at-half-maximum (FWHM) of the elastic peak, which is typically 1.5-2% of the incident energy, would be narrow, giving better energy resolution. As discussed below, the larger scattering angles reveal the change in the peak intensities vs |*Q*| and confirm whether a peak is magnetic or phonon in nature.

For [Fe(TPP)Cl] (**1**), measurements were performed at 1.5 and 20 K with incident neutron beam energies of 24.20, 80.66, and 201.64 cm^{-1} and resolutions at the elastic peak of 0.59, 3.1, and 10 cm^{-1}, respectively. For [Mn(TPP)Cl] (**2**), measurements were performed at 2.08, 5.1, 10.2, and 50.0 K with incident neutron beam energies of 12.58, 24.20, and 96.79 cm^{-1} and resolutions at the elastic peak of 1.9, 0.46, and 3.1 cm^{-1}, respectively. For [Mn(TPP)] (**4**), measurements were performed at 2.08, 5.1, 10.2, and 50.0 K with incident neutron beam energies of 12.58, 24.20, and 96.79 cm^{-1} and resolutions at the elastic peak of 0.18, 0.43, and 3.0 cm^{-1}, respectively. For [Cr(TPP)Cl] (**3**), the measurements were performed at 2.08, 10.2, and 50 K using incident neutron beam energies of 8.06 and 24.20 cm^{-1} and resolutions at the elastic peak of 0.097 and 0.43 cm^{-1}, respectively. It took approximately 24 h to run one sample at various temperatures and incident neutron energies. Data were then reduced and analyzed using the DAVE (Data Analysis and Visualization Environment) program package.[19]

The INS spectra were simulated by calculating the energies E_n and corresponding wavefunctions $|n\rangle$ via exact diagonalization of spin-Hamiltonian in Eq. 1. These can be used to get the INS intensity for a transition $i \rightarrow f$, which is proportional to the scattering function $S^{\alpha\beta}(\boldsymbol{Q},\omega)$:[20]

$$S^{\alpha\beta}(\boldsymbol{Q},\omega) = \sum_{j}^{j'} exp\{i\boldsymbol{Q}(r_j - r_{j'})\} \times \sum_i^f p_i \langle i|\hat{S}_{j,\alpha}|f\rangle\langle f|\hat{S}_{j',\beta}|i\rangle\delta(E_i - E_f) \quad \text{(Eq. 2.3)}$$

$S_{j,\alpha}$ is the α component of the spin operator S_j at position r_j where α, β stand for Cartesian coordinates *x, y, z*. The initial and final states of a transition with energy E_n are $|i\rangle$ and $|f\rangle$, respectively. $\boldsymbol{Q} = \boldsymbol{k}_i - \boldsymbol{k}_f$ is the scattering vector of the momentum transfer where $\boldsymbol{k}_i$ and $\boldsymbol{k}_f$

refer to the wavevector of the incoming and outgoing neutrons, respectively, and p_i is the Boltzmann population factor of state $|i\rangle$. For powder samples Eq. 2 has to be averaged in $\boldsymbol{Q}$ space using known equations.[21] The values of D and, if necessary, E were systematically scanned in order to find the best fit to the experimental spectra. The linewidths of the INS peaks lie within experimental accuracy determined by the instrumental resolution. The effective resolution function $R(Q,E)$ of CNCS is nearly Gaussian in energy.[13] Therefore, the INS intensities were fit assuming Gaussian line shapes with FWHM of the energy resolution for the CNCS spectrometer. The detailed analyses, using the plots with smaller stepsize points, and calculations of errors in the D values, are given for each complex in Appendix A.

2.3. Results and Discussion

2.3.1. [Fe(TPP)Cl] (1)

Powder X-ray diffraction of the sample at 296 K, Figure 2.1, is consistent with the simulated pattern predicted from the single crystal X-ray diffraction data at 20(2), 143(2) and 293(2) K, indicating that the solid sample is in the tetragonal crystal system (with the 4-fold symmetry).[17,22] Indexing of the powder X-ray diffraction data from the sample by the McMaille method also yielded the same tetragonal unit cell, Figure 2.2. Our earlier studies of the X-ray diffraction of a single crystal of [Fe(TPP)Cl] (**1**) revealed that the crystal remains in the tetragonal system between 296(2) and 20(2) K.[17] Although the X-ray diffraction studies were not conducted at 1.5 K, the INS studies discussed below suggest that the sample remained in the tetragonal crystal system between 1.5 and 20 K.

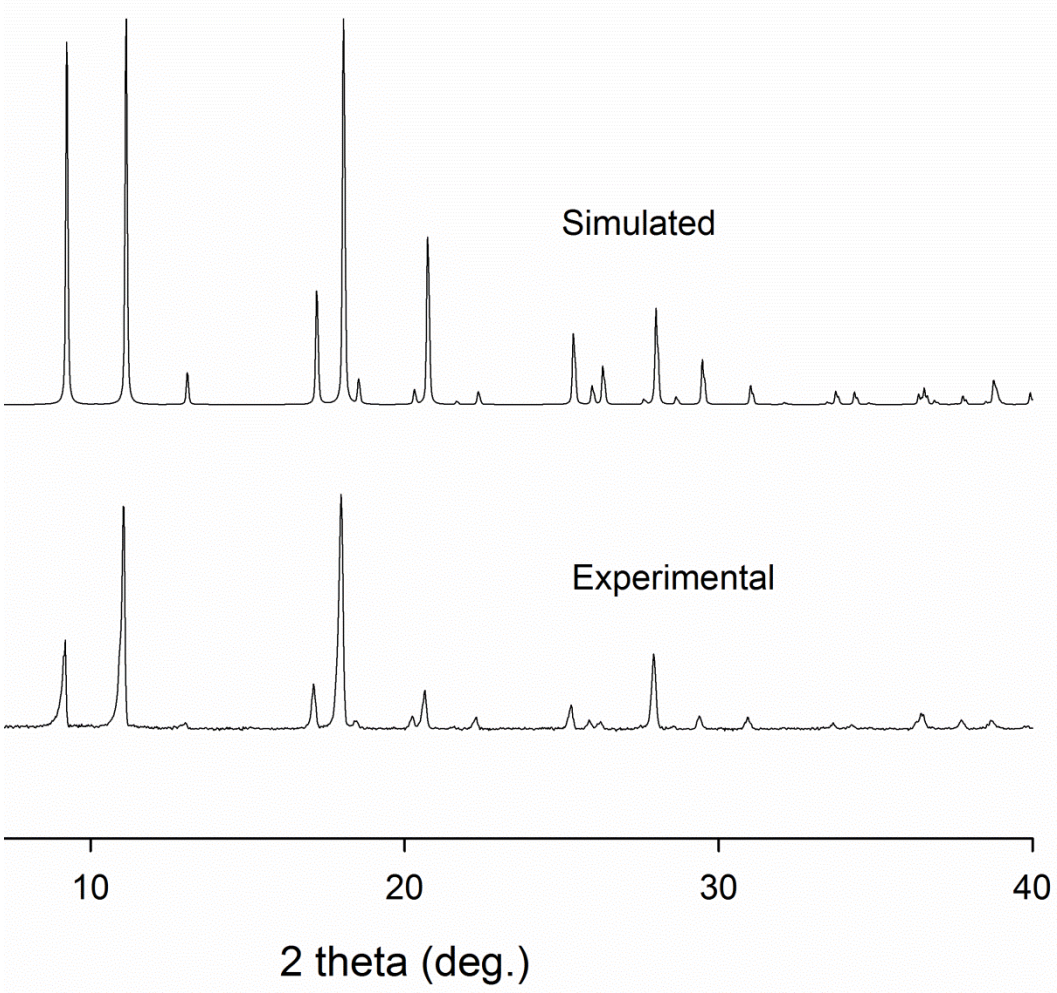

Figure 2.1. (Top) Simulated diffraction pattern of [Fe(TPP)Cl] (**1**) single crystal data. (Bottom) Diffraction pattern of **1** obtained from sample used for INS.

Table 2.1. Unit cell parameters determined by the McMaille indexing method

	a (Å)	*b* (Å)	*c* (Å)	*α* (°)	*β* (°)	*γ* (°)	Cell Volume (Å^3)	Not Indexed Lines	FOM[a]
[Fe(TPP)Cl] (**1**)	13.6091	13.6091	9.8764	90	90	90	1829.1840	0	45.18
[Mn(TPP)Cl] (**2**)	13.5302	13.5302	9.9387	90	90	90	1819.4410	0	34.30
[Cr(TPP)Cl][b] (**3**)	13.4405	13.4405	9.6810	90	90	90	1748.8440	6	88.55
[Cr(TPP)Cl][c] (**3**)	10.6576	8.5982	13.3577	90	90	90	1224.0490	1	532.22
[Mn(TPP)] (**4**)	15.5230	15.5230	7.3597	90	90	90	1773.4190	5	60.12

[a] FOM = Figure of Merit.

[b] Sample from recrystallization in methylene chloride.

[c] Sample used in the INS study.

In [Fe(TPP)Cl] (**1**), the Fe(III) ion has a high spin (S = 5/2) configuration, and its electronic ground state is split into three Kramers doublets: M_S = ±1/2, ±3/2, and ±5/2. The spacings among the three doublets are 2D and 4D, respectively (Scheme 2.2). The ZFS in [Fe(TPP)Cl] (**1**) has been the subject of several studies. Its D values have been determined by, e.g., magnetic susceptibility measurements,[23] far-IR,[24] NMR,[25] and Mössbauer,[26] MCD,[6] and EPR[27] spectroscopies. The D values obtained, ranging from 3.2 to 11.9 cm^{-1}, are summarized in Table 2.2.

Table 2.2. ZFS values for [Fe(TPP)Cl] (**1**)

D (cm^{-1})	Sample form	Technique
11.9	Powder	Magnetic susceptibility[23a]
8.0(5)	Powder	Magnetic susceptibility[23b]
6.0(1)	Single crystal	Magnetic susceptibility[23c,d]
6.5	Powder	Far IR[24]
11.3	Solution	NMR[25]
7.0(1.0)	Powder	Mössbauer[26]
6.9	Polystyrene film	MCD[6]
3.2	Doped in H_2TPP	EPR[27]
6.33(8)	Powder	INS (this work)

In the INS spectra of [Fe(TPP)Cl] (**1**), a peak at 12.65(8) cm^{-1} was observed (Figure 2.2, Left) at both 1.5 and 20 K. This corresponds to the ±1/2 → ±3/2 excitation (Scheme 2.2). At 20 K, a peak at -12.65(8) cm^{-1} is observed, indicating that the incident neutrons

gain energy from the sample in the process. In other words, at 20 K, the excited ±3/2 states in Scheme 2.2 are partially populated. During the scattering process, those molecules return to the ground ±1/2 states, transferring the energy to the neutrons.

INS is unique in that it is capable of distinguishing peaks of magnetic excitations from those of vibrations.[12] Peaks of magnetic excitations *decrease* in intensity with increased |*Q*|, while those from vibrations *increase* in intensity with increased |*Q*|.[12] The decrease in magnetic excitations follows the square of the magnetic form factor *F*(*Q*). Changes in peak intensities vs |*Q*| are given in Figure 2.2-Right. The intensity of the 12.65(8) cm^{-1} peak indeed decreases with increased |*Q*|, confirming that it is magnetic in nature. The intensities of the peaks >16 cm^{-1} increase with increased |*Q*|, indicating that they are vibrational peaks.

Earlier studies of [Fe(TPP)Cl] (**1**) have given positive *D* values, as summarized in Table 2.2. INS, however, can be used to confirm that the sign of the *D* parameter. If *D* > 0, the lowest energy level is ±1/2 and the first excitation is from this level to ±3/2 level with a peak at 2*D*, as shown in Scheme 2.2-Top. When the temperature is raised, the ±3/2 is populated and one expects to see the ±3/2 to ±5/2 transition with a peak at 4*D* at a higher energy. If *D* < 0, the lowest energy level is ±5/2 and the first excitation is from this level to ±3/2 level with a peak at 4*D*, as shown in Scheme 2.2-Bottom. When the temperature is raised, the ±3/2 is populated and one expects to see the ±3/2 to ±1/2 transition with a peak at 2*D* at a lower energy. Figure 2.3-Left shows the measured INS spectra with the incident neutron energy of 80.66 cm^{-1}. Although there is considerable phonon scattering at both temperatures, a new peak is visible at around 25.60 cm^{-1} in

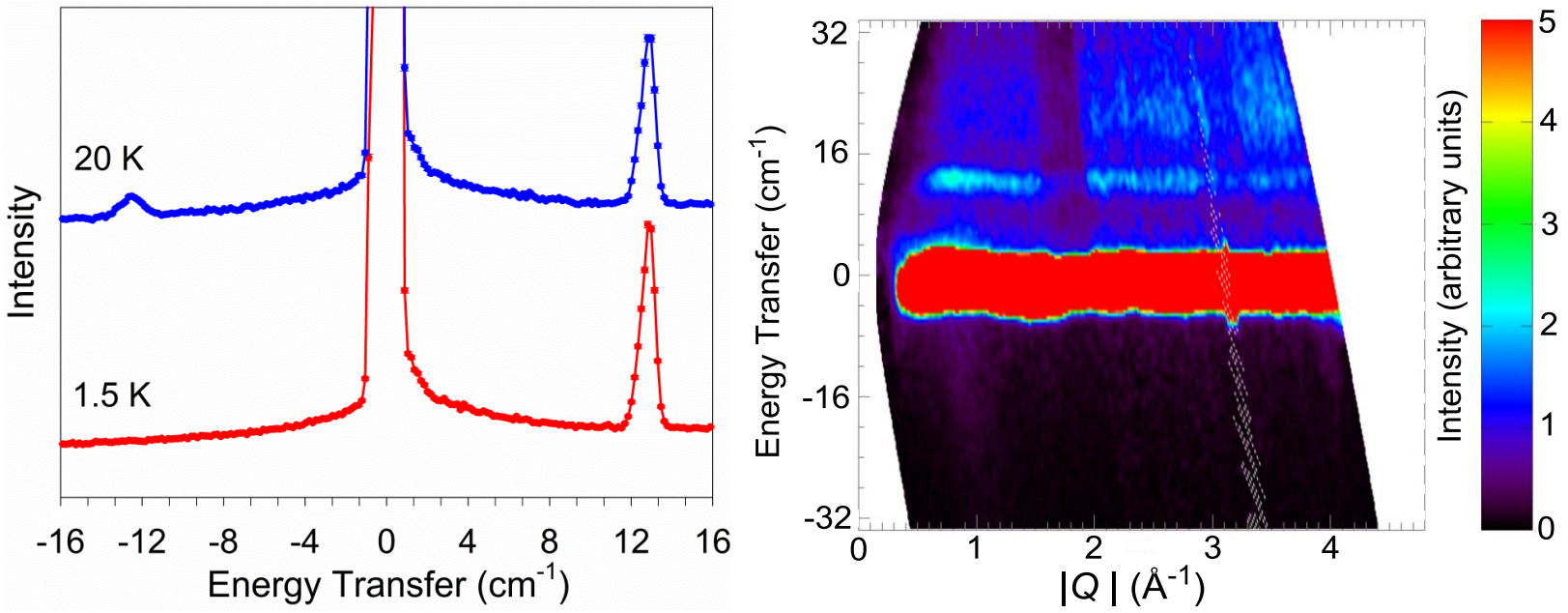

Figure 2.2. (Left) INS spectra of [Fe(TPP)Cl] (**1**) using a 24.20 cm^{-1} incident neutron beam. (Right) Change in the peak intensities vs |*Q*| at 1.5 K. Incident neutron energy: 80.66 cm^{-1}.

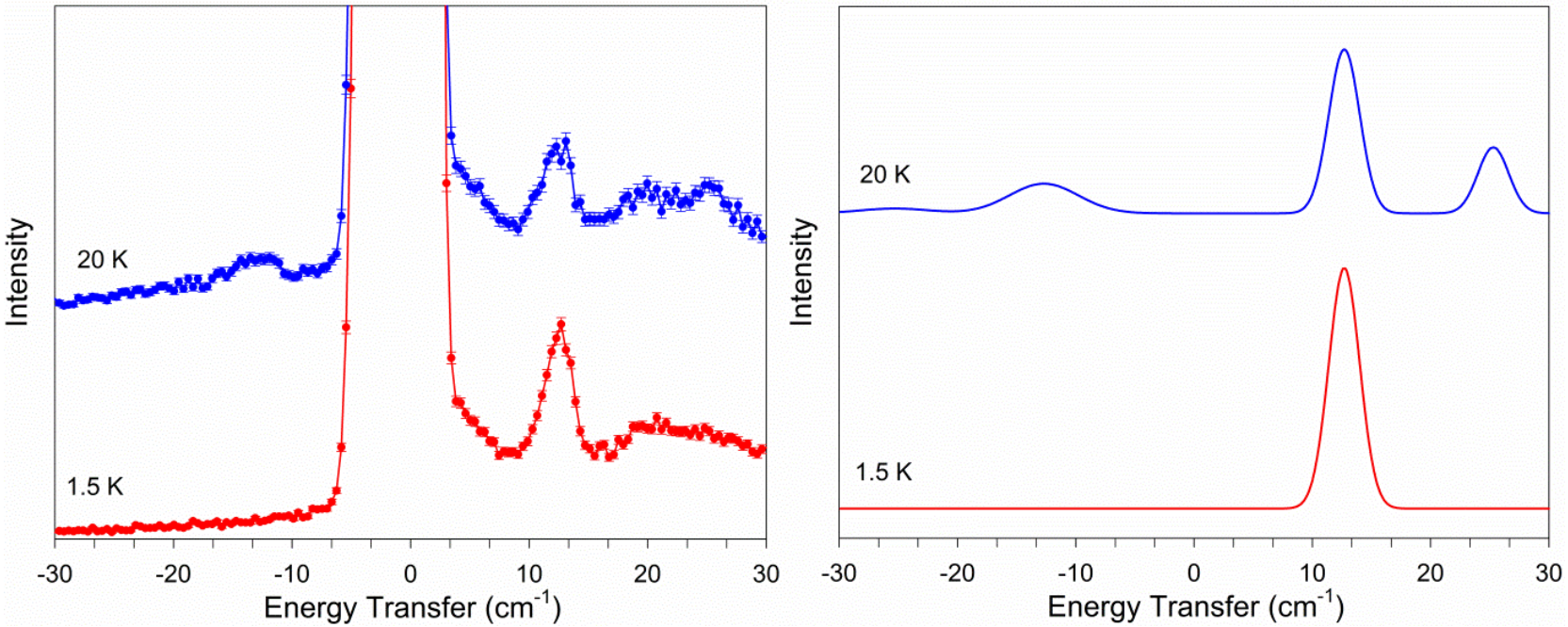

Figure 2.3. (Left) INS spectra of [Fe(TPP)Cl] (**1**) using a 80.66 cm^{-1} incident neutron energy. (Right) Theoretical INS spectra of an $S = 5/2$ spin system with $D = 6.33$ cm^{-1}.

the 20 K spectrum. This peak matches nicely with the theoretical INS spectra (Figure 2.3-Right).

Our single crystal diffraction studies of [Fe(TPP)Cl] (**1**) at 20(2) K in Part 2 indicate that the crystal is in a tetragonal system at this temperature. A comparison of the INS spectra at 1.5 and 20 K in Figure 2.2-Left shows no observable rhombic splitting(s) at 1.5 K, suggesting that the solid samples remained in the tetragonal crystal system at this temperature. Thus the INS studies here give $2D$ = 12.65(8) cm^{-1}, D = 6.33(8) cm^{-1} for **1**.

The D value of 6.33(8) cm^{-1} for [Fe(TPP)Cl] (**1**) is close to 6.95(14) cm^{-1} for protoporphyrin IX dimethyl ester Fe(III) chloride (Scheme 2.3) that Brackett and coworkers measured using far-IR spectroscopy.[28] The protoporphyrin complex in Scheme 2.3 does not have a 4-fold symmetry, and its $E/D \approx 0$, indicating there is nearly no rhombic splitting in this complex.

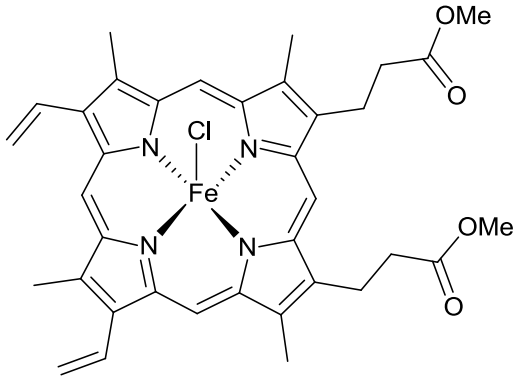

Scheme 2.3. Protoporphyrin IX dimethyl ester Fe(III) chloride.

2.3.2. [Mn(TPP)Cl] (2)

Single crystals of [Mn(TPP)Cl] (**2**) and [Fe(TPP)Cl] (**1**) are isomorphous.[17,18,22] Powder X-ray diffraction of the sample at 296 K, Figure 2.4, is consistent with the simulated pattern predicted from the single crystal X-ray diffraction data at 293(2) K, indicating that the solid sample is in the tetragonal crystal system (with the 4-fold symmetry).[18] Indexing of powder X-ray diffraction data from the sample by the McMaille method also yielded the same tetragonal unit cell, Table 2.1. As in [Fe(TPP)Cl] (**1**), powders of **2** likely remain in the tetragonal crystal system at 2.1 and 5.1 K used to conduct INS studies. The INS data discussed below are also consistent with the solid sample with the 4-fold symmetry.

[Mn(TPP)Cl] (**2**) is a d^4 complex with $S = 2$. Its integer spin electronic ground state is split into three levels: $M_S = 0, \pm1$, and ±2. The ZFS parameter for **2** was first obtained by Behere and coworkers through magnetic susceptibility measurements.[29] Using a single crystal they obtained $D = -2.3(2)$ cm^{-1}. When a powder sample was used, the D value obtained is -1.9 cm^{-1}.[29] [Mn(TPP)Cl] (**2**) is an "EPR silent" integer spin system and it was not until the use of high-field, high-frequency EPR (HFEPR) by Hoffman and coworkers that the ZFS of the complex could be probed to give the $D \approx -2.3$ cm^{-1}.[30]

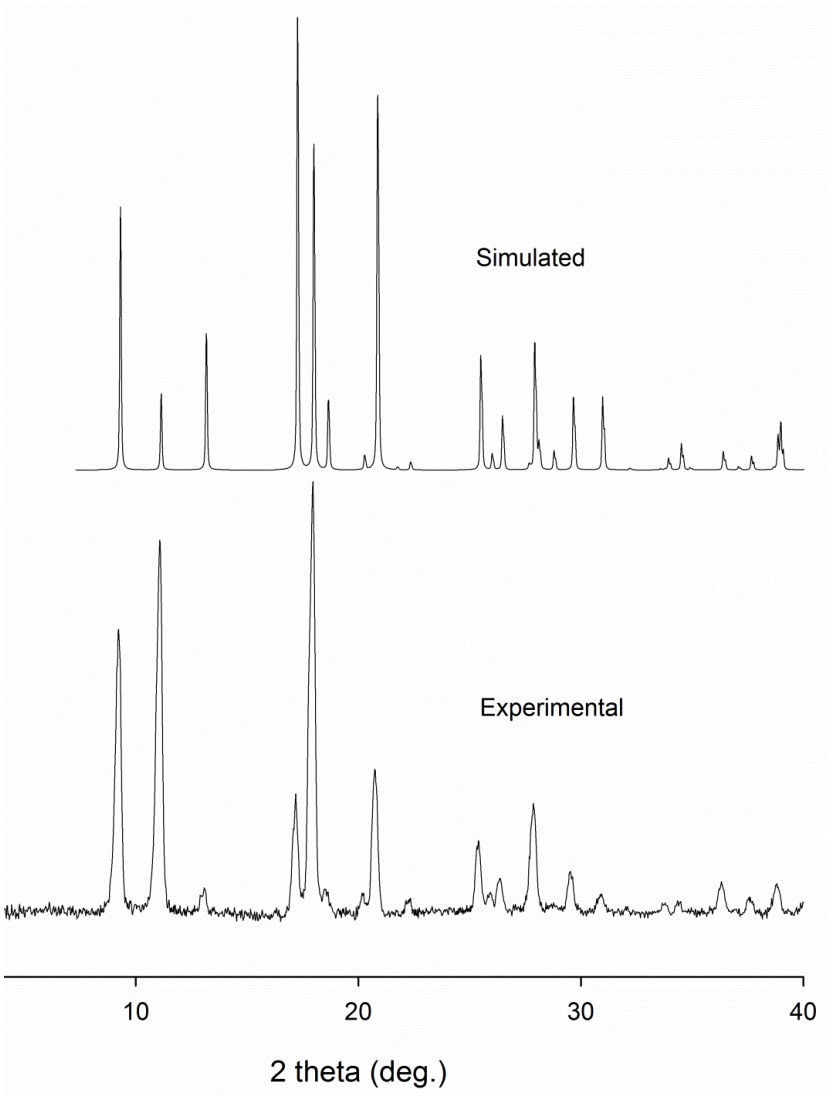

Figure 2.4. (Top) Simulated diffraction pattern of [Mn(TPP)Cl] (**2**) single crystal data. (Bottom) Diffraction pattern of **2** obtained from sample used for INS.

The measured and theoretical INS spectra of [Mn(TPP)Cl] (**2**) are shown in Figure 2.5. The small neutron incident energy (12.58 cm^{-1}) excludes vibrational peaks. At 2.1 K there is only one large peak at 6.70(3) cm^{-1}. When the temperature is increased to 5.1 K, a second peak becomes visible at 2.24(3) cm^{-1}. As in the INS spectra of [Fe(TPP)Cl] (**1**), the sign of D can be determined directly using INS for complexes with $S > 3/2$. If its D value is positive ($D > 0$), the ZFS would take the spacings among the three levels as illustrated in Scheme 2.2-Top. At 2.1 K, the peak at 6.698(15) cm^{-1} would correspond to the 0 → ±1 transition and equal to D. As the temperature is increased to 5.1 K, the ±1 level is populated, and a peak at $3D$ = 20.09 cm^{-1} corresponding to the ±1 → ±2 transition would be expected. If the D value is negative ($D < 0$), the ZFS would take the spacings among the three levels as illustrated in Scheme 2.2-Bottom. At 2.1 K, the peak at 6.698(15) cm^{-1} would correspond to the ±2 → ±1 transition and equal to $-3D$. As the temperature is increased to 5.1 K, the ±1 level is populated, and a peak at 2.23(3) cm^{-1} (= $-D$) corresponding to the ±1 → 0 transition would be expected. The fact that only the larger ±2 → ±1 transition is populated at the low temperature of 2.1 K in Figure 2.5 indicates that the D value is negative. Thus, for **2**, the INS study gives D = -2.24(3) cm^{-1}. This value is similar to D = -2.3(2) cm^{-1} and $D \approx -2.3$ cm^{-1} that Behere et al.[29] and Hoffman et al.[30] reported, respectively. This D value for **2** is also close to D = -2.48(7) cm^{-1} for [Mn(TPP)(O_2)] that does not have the C_{4v} symmetry.[31]

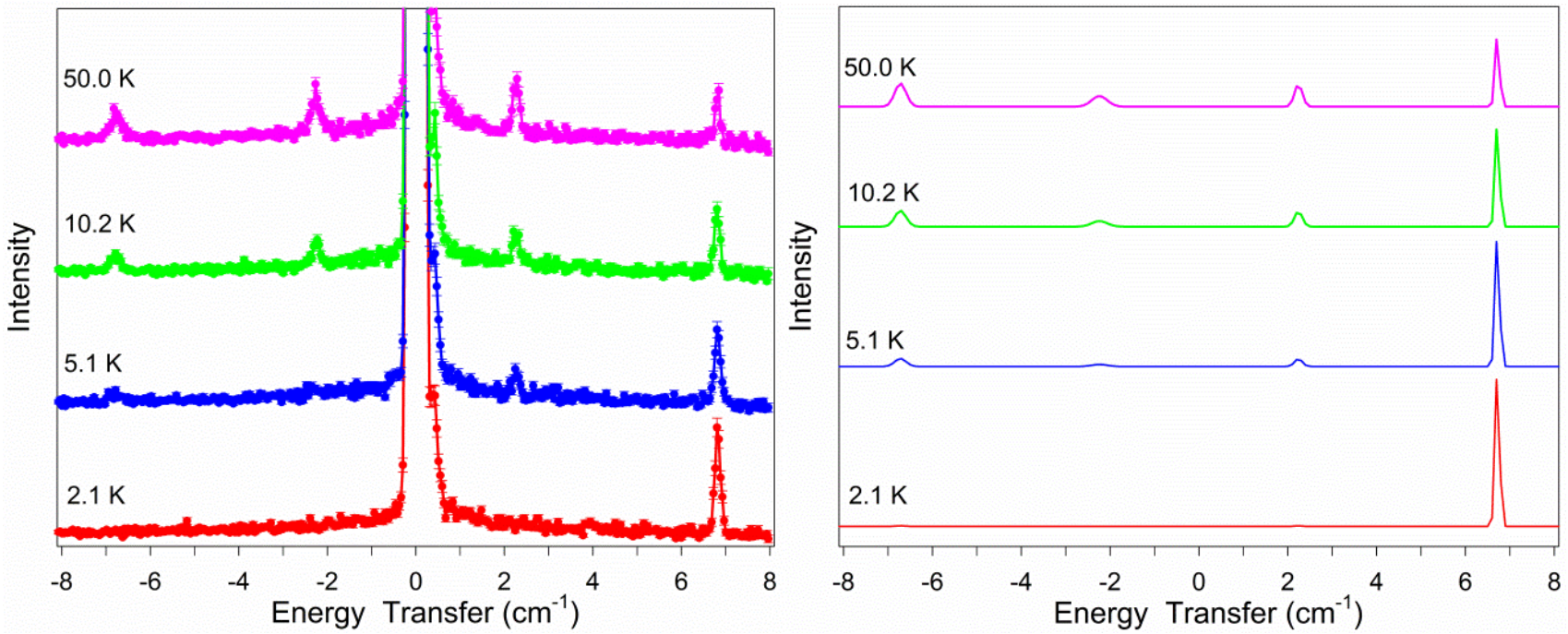

Figure 2.5. (Left) INS spectra of [Mn(TPP)Cl] (**2**) using a 12.58 cm^{-1} incident neutron beam. (Right) Theoretical INS spectra of an $S = 2$ spin system with $D = -2.24$ cm^{-1}.

2.3.3. [Mn(TPP)] (4)

[Mn(TPP)] (**4**) is an air-sensitive, d^5 complex. Unlike its chloride derivative [Mn(TPP)Cl] (**2**), there is no ligand in the axial position. Both **4** and its adducts [Mn(TPP)L] (L = THF, pyridine) and [Mn(TPP)L_2] (L = toluene, pyridine) have been actively studied.[23,31] ESR studies of [Mn(TPP)(py)] by Hoffman and coworkers gave D^{Mn} = ~0.55 cm^{-1}.[31]

Powder X-ray diffraction of the sample was conducted using an air-sensitive sample holder with a zero background plate, the pattern is shown in Figure 2.6. After removing the peak of the Mylar film at 2θ = 26.52°, the peaks by [Mn(TPP)] (**4**) were indexed by the McMaille method to give a tetragonal unit cell (Table 2.1).

The electronic ground state of [Mn(TPP)] (**4**) is split into three Kramers doublets: M_S = ±1/2, ±3/2, and ±5/2. If its D value is positive (D > 0), the ZFS would take the spacings among the three doublets as illustrated in Scheme 2.2. To our knowledge, ZFS of adduct-free **4** has not been reported. The measured and theoretical INS spectra for **4** are shown in Figure 2.7. It is assumed that the solid sample remained in the tetragonal crystal system at 2.1-50 K, as no observable rhombic splitting(s) was observed. At 2.1 K, the peak for the ±1/2 → ±3/2 excitation is very prominent at 1.57(2) cm^{-1}. At 5.1 K a second excitation peak is already visible at 3.14(2) cm^{-1} which corresponds to the ±3/2 → ±5/2 excitation. For [Mn(TPP)] (**4**), the INS measurements are consistent with a positive D value and they give $2D$ = 1.57(2) cm^{-1} and thus D = 0.79(2) cm^{-1}.

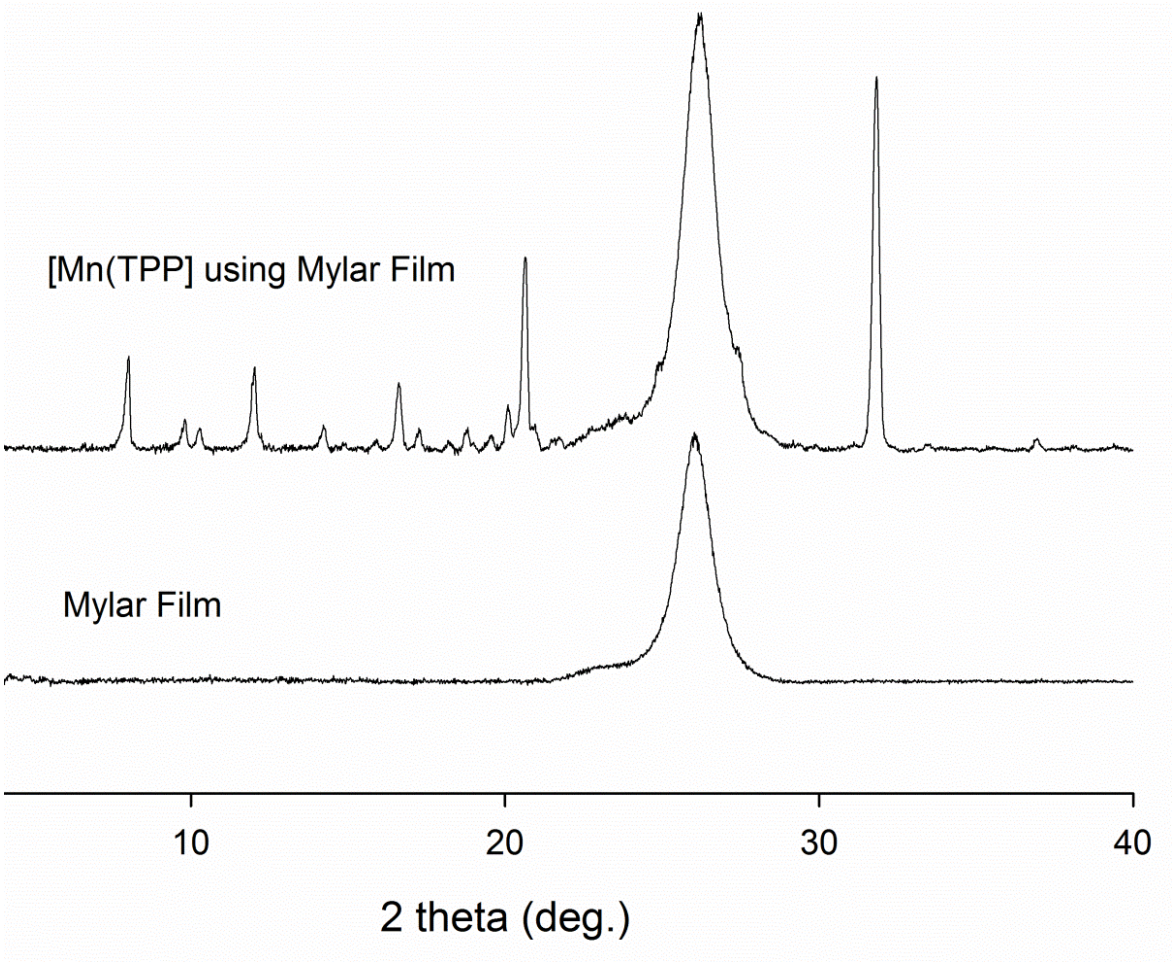

Figure 2.6. (Top) Diffraction pattern of air-sensitive [Mn(TPP)] (**4**) using a Mylar film. (Bottom) Diffraction pattern of the Mylar film alone.

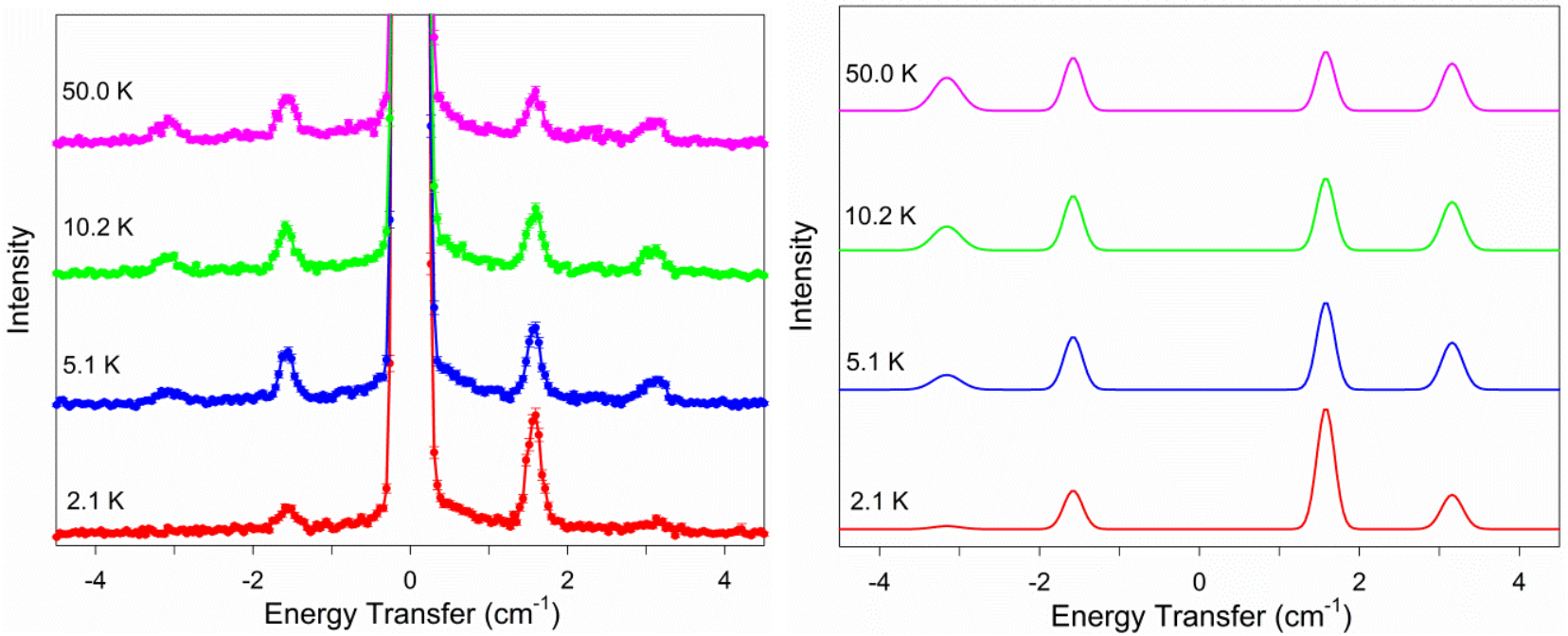

Figure 2.7. (Left) INS spectra of [Mn(TPP)] (**4**) using a 12.58 cm^{-1} incident neutron beam. (Right) Theoretical INS spectra of an $S = 5/2$ spin system with $D = 0.79$ cm^{-1}.

2.3.4. [Cr(TPP)Cl] (3)

Single crystal structure of [Cr(TPP)Cl] (**3**) or its powder X-ray diffraction pattern has not been reported. We have collected the powder X-ray diffraction of the sample at 296 K, and the results are given in Figure 2.8. Indexing of the powder X-ray diffraction data from the sample by the McMaille method yielded an orthorhombic unit cell (10.6576 Å, 8.5982 Å, 13.3577 Å), Table 2.1. In phase transformation of crystals, the trend is that at a lower temperature, crystals usually go to a lower symmetry phase.[32] Thus it is unlikely that the sample solids transformed to the tetragonal crystal system at 2.1-50 K, temperatures at which INS data were collected.

[Cr(TPP)Cl] (**3**) has a d^3 configuration (S = 3/2). If the solids of the sample have a 4-fold symmetry, the four states split into two Kramers doublets as shown in Scheme 2.2. To our knowledge, the ZFS for **3** has not been studied. However, using EPR spectroscopy, Hoffman and coworkers studied [CrTPP(Cl)(L)] (L = N, S, or O donors), a series of its adducts.[33] $|D|$ is ca. 0.156 cm^{-1} for N-donor ligands and 0.232 cm^{-1} for O- and S- donor ligands. The small D values are typical of other Cr(III) octahedral complexes, and this is mainly due to the small spin-orbital coupling of octahedral Cr(III) complexes. For an octahedral d^3 complex with a t_{2g}^3 configuration, the electron distribution is essentially spherical, making its D value near zero.[34] The largest D value recorded for a Cr(III) complex is the psuedooctahedral complex $[Cr(dmpe)_2(CN)I]^+$ [dmpe = 1,2-bis(dimethylphosphino)ethane], $|D|$ = 2.30 cm^{-1}, that Long and coworkers reported.[34]

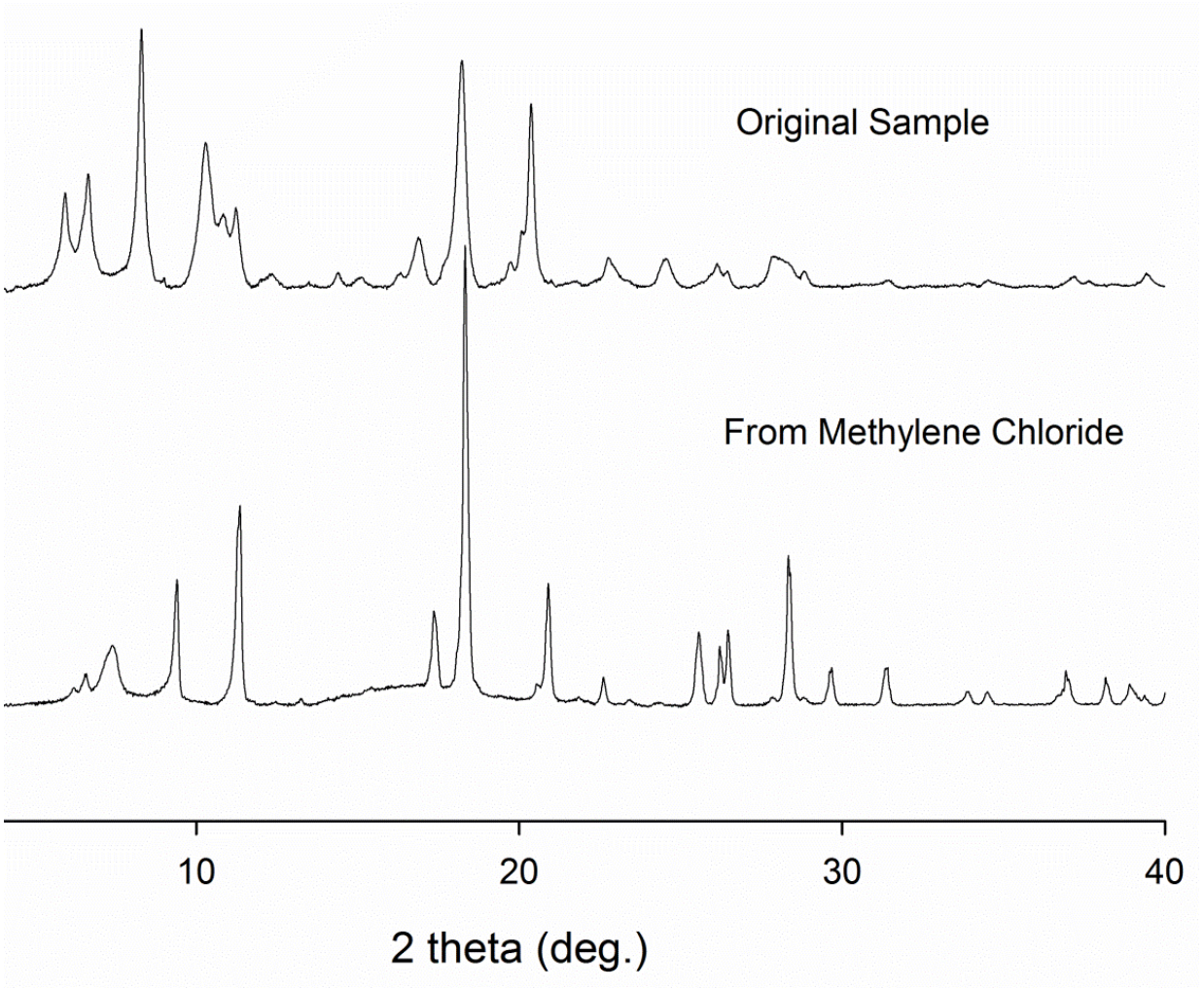

Figure 2.8. [Cr(TPP)Cl] (**3**): (Top) Diffraction pattern of the INS sample. (Bottom) Diffraction pattern of a sample recrystallized from methylene chloride. This pattern was indexed to a tetragonal phase which is similar to those of tetragonal [M(TPP)Cl] (M = Fe, **1**; Mn, **2**).

Figure 2.9 shows the experimental and theoretical INS spectra for [Cr(TPP)Cl] (**3**). The zero-field splitting for **3** is very small and almost at the limits for detection by CNCS.[13] A peak is clearly observed at 0.468(12) cm^{-1} which corresponds to the transition between the $\pm 3/2 \rightarrow \pm 1/2$ levels. The value was calculated using the peaks at 10.2 and 50.0 K. As mentioned earlier and shown in Scheme 2.2, the sign of D for complexes with $S = 3/2$ cannot be determined directly using INS. *If the solids of the sample had a 4-fold symmetry*, $|2D|$ would equal 0.468(12) cm^{-1}, and $|D|$ would be 0.234(12) cm^{-1}. Since the solids of the sample are in an orthorhombic crystal system, the peak at 0.468(12) cm^{-1} includes both the axial (D) and rhombic (E) ZFS parameters, as shown in Eq. 2.1. As 0.468(12) cm^{-1} is small and normally it is assumed that the ZFS parameters obey the relationship: $|D| \geq 3E \geq 0$,[4a,28] the E value is likely very small as well. The fitting procedure of the observed excitation as described in the Experimental Section yields the range of $|D|$ = 0.234(12)-0.203(12) cm^{-1} and the corresponding range E = 0.000-0.068(8) cm^{-1}. These data indicate small zero-field splittings for this square pyramidal complex with a d_{xy}^1 (b_2^1) and d_{xz}^1,d_{yz}^1 (e^1) configuration. If a sample of [Cr(TPP)Cl] (**3**) in the tetragonal crystal system is available, it is expected that INS studies using this sample will give the $|D|$ value. Then using the results from the current work, the E value may be calculated.

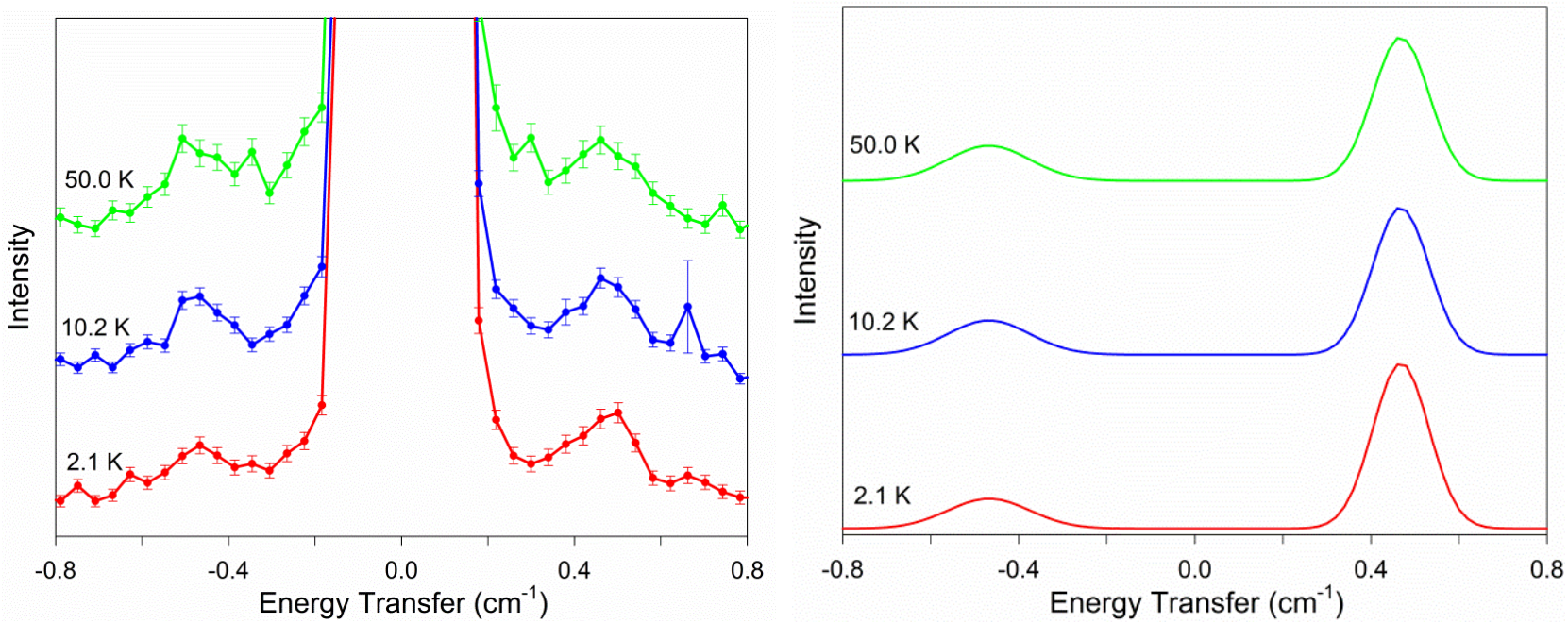

Figure 2.9. (Left) INS spectra: [Cr(TPP)Cl] (**3**). Incident neutron energy: 8.06 cm^{-1}. (Right) Theoretical INS spectra of an S = 3/2 spin system with D = 0.234 cm^{-1} and E = 0.

2.4. Concluding Remarks

Magnetic excitations of metalloporphyrins have been probed for the first time by INS. Due to the small energy of these excitations, nondeuterated samples were used. A positive D value, 6.33(8) cm^{-1} for [Fe(TPP)Cl] (**1**) and 0.79(2) cm^{-1} for [Mn(TPP)] (**4**), were determined for the two S = 5/2 complexes. Typical of Mn(III) S = 2 complexes a negative D, -2.24(3) cm^{-1}, was determined for [Mn(TPP)Cl] (**2**). For [Cr(TPP)Cl] (**3**), $|D|$ = 0.234(12) cm^{-1}, which is due in part to the spherical nature of the unpaired d electrons in this S = 3/2 spin system.

References

1. (a) *The Porphyrin Handbook*, Kadish, K. M.; Smith, K. M.; Guilard, R., Eds, 2000-2003, Academic Press, San Diego. (b) *Handbook of Porphyrin Science with Applications to Chemistry, Physics, Materials Science, Engineering, Biology and Medicine*, Kadish, K. M.; Smith, K. M., Guilard, R., Eds., 2010, World Scientific, Singapore. (c) *The Porphyrins*, Dolphin, D., Ed., 1978-1979, Academic Press, New York: Walker, F. A. Vol. 5, Ch. 36, pp. 81-183; La Mar, G. N.; Satterlee, J. D.; De Ropp, J. S. Vol. 5, Ch. 37, pp. 185-298; Cheek, J.; Dawson, J. H. Vol. 7, Ch. 53, pp. 339-369.
2. For geochemistry of porphyrins, See, e,g., Callot, H. J.; Ocampo, R., 2000, in Ref. 1a, Vol. 1, Ch. 7, pp. 349-398.
3. (a) Collman, J. P.; Boulatov, R.; Sunderland, C. J.; Fu, L. *Chem. Rev.* **2004**, *104*, 561. (b) Hoffman, B. M. *Proc. Nat. Acad. Sci. USA* **2003**, *100*, 3575. (c) Yang, F.; Shokhireva, T. K.; Walker, F. A. *Inorg. Chem.* **2011**, *50*, 1176. (d) Scheidt, W. R.; Barabanschikov, A.; Pavlik, J. W.; Silvernail, N. J.; Sage, J. T. *Inorg. Chem.* **2010**, *49*, 6240. (e) Decker, A.; Solomon, E. I. *Angew. Chem., Int. Ed.* **2005**, *44*, 2252. (f) de Visser, S. P.; Valentine, J. S. V.; Humphreys, K. J. *Pure Appl. Chem.* **1998**, *70*, 855. (g) Brand, H.; Arnold, J. *Coord. Chem. Rev.* **1995**, *140*, 137. (h) Fujii, H. *Coord. Chem. Rev.* **2002**, *226*, 51. (h) Richter-Addo, G. B. *Acc. Chem. Res.* **1999**, *32*, 529. (i) Zhang, P.; Wang, M.; Li, X. Qiang; C., Hong G.; Dong, J. F.; Sun, L. C. *Sci. China Chem.* **2012**, *55*, 1274.
4. (a) Boca, R. *Coord. Chem.* **2004**, *248*, 757. (b) Neese, F.; Solomon, E. I. in: Miller, J. S., Drillon, M. (Eds) *Magnetism* Vol. IV, Wiley-VCH, 2003, pp. 345-466. (c) Long,

J. R., in *Chemistry of Nano-structured Materials*; Yang, P., Ed.; World Scientific: Hong Kong, 2003; pp. 291-315. (d) Misra, S. K., in *Multifrequency Electron Paramagnetic Resonance*, Wiley-VCH: 2011; pp. 589-597. (e) McInnes, E. L., in *Single-Molecule Magnets and Related Phenomena*, Winpenny, R., Ed. Springer: 2006; Vol. 122, pp. 69-102. (f) Krzystek, J.; Ozarowski, A.; Telser, J. *Coord. Chem. Rev.* **2006**, *250*, 2308. (g) Gatteschi, D. *J. Phys. Chem. B* **2000**, *104*, 9780. (h) Reiff, W. M. *ACS Symp. Ser.* **1996**, 644, 115.

5. (a) Yoon, J.; Mirica, L. M.; Stack, T. D. P.; Solomon, E. I. *J. Am. Chem. Soc.* **2004**, *126*, 12586. (b) Her, J.-H.; Stephens, P. W.; Kennon, B. S.; Liu, C.; Miller, J. S. *Inorg. Chim. Acta* **2010**, *364*, 172. (c) Reisner, E.; Telser, J.; Lippard, S. J. *Inorg. Chem.* **2007**, *46*, 10754. (d) Krzystek, J.; Telser, J.; Pardi, L. A.; Goldberg, D. P.; Hoffman, B. M.; Brunel, L.-C. *Inorg. Chem.* **1999**, *38*, 6121. (e) Godwin, H. A.; Collman, J. P.; Marchon, J.-C.; Maldivi, P.; Yee, G. T.; Conklin, B. J. *Inorg. Chem.* **1997**, *36*, 3499. (f) Holman, T. R.; Juarez-Garcia, C.; Hendrich, M. P.; Que, Jr., L.; Münck, E. *J. Am. Chem. Soc.* **1990**, *112*, 7611. (g) Schulz, C. E.; Song, H.; Mislankar, A.; Orosz, R. D.; Reed, C.A.; Debrunner, P. G.; Scheidt, W.R. *Inorg. Chem.* **1997**, *36*, 406. (h) Miyasaka, H.; Clérac, R.; Campos-Fernández, C. S.; Dunbar, K. R. *J. Chem. Soc., Dalton Trans.* **2001**, 858. (i) Ma, L.-H.; Liu, Y.; Zhang, X.; Yoshida, T.; Langry, K. C.; Smith, K. M.; La Mar, G. N. *J. Am. Chem. Soc.* **2006**, *128*, 6391. (j) Reynolds, P.A.; Moubaraki, B.; Murray, K.S.; Cable, J.W.; Engelhardt, L.M.; Figgis, B.N. *J. Chem. Soc., Dalton Trans.* **1997**, 263.

6. Browett, W. R.; Fucaloro, A. F.; Morgan, T. V.; Stephens, P. J. *J. Am. Chem. Soc.* **1983**, *105*, 1868.

7. Yang, E. C.; Wernsdorfer, W.; Hill, S.; Edwards, R. S.; Nakano, M.; Maccagnano, S.; Zakharov, L. N.; Rheingold, A. L.; Christou, G.; Hendrickson, D. N. *Polyhedron* **2003**, *22*, 1727-1733.

8. (a) *Magnetism: Molecules to Materials*; Miller, J. S.; Drillon, M., Eds.; Wiley-VCH, 2002. (b) *Applications of Physical Methods to Inorganic and Bioinorganic Chemistry*; Scott, R.A.; Lukehart, C.M., Eds.; Wiley, 2007, including Larese, J.Z., pp. 291-313.

9. (a) Eckert, J.; Kubas, G. J.; Hall, J. H.; Hay, P. J.; Boyle, C. M. *J. Am. Chem. Soc.* **1990**, *112*, 2324. (b) Van der Sluys, L. S.; Eckert, J.; Eisenstein, O.; Hall, J. H.; Huffman, J. C.; Jackson, S. A.; Koetzle, T. F.; Kubas, G. J.; Vergamini, P. J.; Caulton, K. G. *J. Am. Chem. Soc.* **1990**, *112*, 4831. (c) Mojet, B. L.; Eckert, J.; van Santen, R. A.; Albinati, A.; Lechner, R. E. *J. Am. Chem. Soc.* **2001**, *123*, 8147. (d) Rowsell , J. L. C.; Eckert, J.; Yaghi, O. M. *J. Am. Chem. Soc.* **2005**, *127*, 14904. (b) Ma, S.; Eckert, J.; Forster, P. M.; Yoon, J. W.; Hwang, Y. K.; Chang, J.-S.; Collier, C. D.; Parise, J. B.; Zhou, H.-C. *J. Am. Chem. Soc.* **2008**, *130*, 15896. (c) Sumida, K.; Horike, S.; Kaye, S. S.; Herm, Z. R.; Queen, W. L.; Brown, C. M.; Grandjean, F.; Long, G. J.; Dailly, A.; Long, J. R. *Chem. Sci.* **2010**, *1*, 184.

10. Clemente-Juan, J. M.; Andres, H.; Borrás-Almenar, J. J.; Coronado, E.; Güdel, H. U.; Aebersold, M.; Kearly, G.; Büttner, H.; Zolliker, M. *J. Am. Chem. Soc.* **1999**, *121*, 10021.

11. (a) Andres, H.; Basler, R.; Güdel, H.-U.; Aromi, G.; Christou, G.; Büttner, H.; Ruffle, B. *J. Am. Chem. Soc.* **2000**, *122*, 12469. (b) Basler, R.; Sieber, A.; Chaboussant, G.; Güdel, H. U.; Chakov, N. E.; Soler, M.; Christou, G.; Desmedt, A.; Lechner, R.

Inorg. Chem. **2005**, *44*, 649. (c) Piligkos, S.; Rajaraman, G.; Soler, M.; Kirchner, N.; van Slageren, J.; Bircher, R.; Parsons, S.; Güdel, H.-U.; Kortus, J.; Wernsdorfer, W.; Christou, G.; Brechin, E.K. *J. Am. Chem. Soc.* **2005**, *127*, 5572. (d) Clemente-Juan, J. M.; Coronado, E. *Coord. Chem. Rev.* **1999**, *193-195*, 361. (e) Dreiser, J.; Waldmann, O.; Carver, G.; Dobe, C.; Güdel, H.-U.; Weihe, H.; Barra, A.-L. *Inorg. Chem.* **2010**, *49*, 8729. (f) Kittilstved, K. R.; Hauser, A. *Coord. Chem. Rev.* **2010**, 254, 2663. (g) Blake, A. B.; Anson, C. E.; arapKoske, S. K.; Cannon, R. D.; Jayasooriya, U. A.; Saad, K.; White, R. P.; Summerfield, D. *J. Chem. Soc., Dalton Trans.* **1997**, 2039. (h) Wang, C. H.; Lumsden, M. D.; Fishman, R. S.; Ehlers, G.; Hong, T.; Tian, W.; Cao, H.; Podlesnyak, A.; Dunmars, C.; Schlueter, J. A.; Manson, J. L.; Christianson, A. D. *Phys. Rev. B* **2012**, *86*, 064439/1.

12. (a) Bacon, G. E. *Neutron Scattering in Chemistry*; Butterworth: London, 1977. (b) Squires, G. L. *Introduction to the Theory of Thermal Neutron Scattering*; Cambridge University Press, 2012.
13. Ehlers, G.; Podlesnyak, A.; Niedziela, J. L.; Iverson, E. B.; Sokol, P. E. *Rev. Sci. Instrum.* **2011**, *82*, 085108.
14. Jones, R. D.; Summerville, D. A.; Basolo, F. *J. Am. Chem. Soc.* **1978**, *100*, 4416.
15. (a) Hill, C. L.; Williamson, M. W. *Inorg. Chem.* **1985**, *24*, 3024. (b) Liston, D. J.; West, B. O. *Inorg. Chem.* **1985**, *24*, 1568.
16. Le Bell, A. *Powder Diffr.* **2004**, *19*, 249.
17. Dougan, B. A., Ph. D. Dissertation, The University of Tennessee, Knoxville. December 2009, Ch. 5.

18. Cheng, B.; Scheidt, W. R. *Acta Crystallogr., Sect. C: Cryst. Struct. Commun.* **1996**, *52*, 361.

19. Azuah, R. T.; Kneller, L. R.; Qiu, Y.; Tregenna-Piggott, P. L. W.; Brown, C. M.; Copley, J. R. D.; Dimeo, R. M. *J. Res. Natl. Inst. Stand. Technol.* **2009**, *114*, 341.

20. Basler, R.; Boskovic, C.; Chaboussant, G.; Güdel, H. U.; Murrie, M.; Ochsenbein, S. T.; Sieber, A. *ChemPhysChem* **2003**, *4*, 910.

21. Waldmann, O.; Güdel, H. U. *Phys. Rev. B* **2005**, *72*, 094422/1.

22. Hoard, J. L.; Cohen, G. H.; Glick, M. D. *J. Am. Chem. Soc.* **1967**, *89*, 1992.

23. (a) Maricondi, C.; Swift, W.; Straub, D. K. *J. Am. Chem. Soc.* **1969**, *91*, 5205. (b) Behere, D. V.; Mitra, S. *Indian J. Chem.* **1980**, *19A*, 505. (c) Behere, D. V.; Mitra, S. *Inorg. Chem.* **1979**, *18*, 1723. (d) Behere, D. V.; Marathe, V. R.; Mitra, S. *J. Am. Chem. Soc.* **1977**, *99*, 4149.

24. Uenoyama, H. *Biochim. Biophys. Acta* **1971**, *230*, 479.

25. La Mar, G. N.; Eaton, G. R.; Holm, R. H.; Walker, F. A. *J. Am. Chem. Soc.* **1973**, *95*, 63.

26. Dolphin, D. H.; Sams, J. R.; Tsin, T. B.; Wong, K. L. *J. Am. Chem. Soc.* **1978**, *100*, 1711.

27. Sato, M.; Rispin, A. S.; Kon, H. *Chem. Phys.* **1976**, *18*, 211.

28. Brackett, G. C.; Richards, P. L.; Caughey, W. S. *J. Chem. Phys.* **1971**, *54*, 4383.

29. (a) Behere, D. V.; Mitra, S. *Inorg. Chem.* **1980**, *19*, 992. (b) Behere, D. V.; Marathe, V. R.; Mitra, S. *Chem. Phys. Lett.* **1981**, *81*, 57.

30. (a) Goldberg, D. P.; Telser, J.; Krzystek, J.; Montalban, A. G.; Brunel, L.-C.; Barrett, A. G. M.; Hoffman, B. M. *J. Am. Chem. Soc.* **1997**, *119*, 8722. (b) Krzystek, J.;

Telser, J.; Pardi, L. A.; Goldberg, D. P.; Hoffman, B. M.; Brunel, L.-C. *Inorg. Chem.* **1999**, *38*, 6121. (c) Krzystek, J.; Pardi, L. A.; Brunel, L.-C.; Goldberg, D. P.; Hoffman, B. M.; Licoccia, S.; Telser, J. *Spectrochim. Acta, Part A* **2002**, *58*, 1113.

31. Hoffman, B. M.; Weschler, C. J.; Basolo, F. *J. Am. Chem. Soc.* **1976**, *98*, 5473.
32. White, R. M.; Geballe, T. H. *Long Range Order in Solids*, Solid State Physics, Supplement 15, Academy Press, 1979
33. Summerville, D. A.; Jones, R. D.; Hoffman, B. M.; Basolo, F. *J. Am. Chem. Soc.* **1977**, *99*, 8195.
34. Karunadasa, H. I.; Arquero, K. D.; Berben, L. A.; Long, J. R. *Inorg. Chem.* **2010**, *49*, 4738.

Part 3

Intermolecular Interactions in Solid-State Metalloporphyrins and Their Impacts on Crystal and Molecular Structures

This part is based on the following paper:

Hunter, S. C.; Smith B. A.; Hoffmann, C. M.; Wang, X.; Chen, Y.-S.; McIntyre; G. J.; Xue, Z,-L, Intermolecular Interactions in Solid-State Metalloporphyrins and Their Impacts on Crystal and Molecular Structures. *Inorganic Chemistry* **2014**, *53*, 11552.

Abstract

Variable-temperature (VT) crystal-structure study of [Fe(TPP)Cl] (**1**, TPP^{2-} = *meso*-tetraphenylporphyrinate) and Hirshfeld surface analyses of its structures and previously published structures of [M(TPP)(NO)] (M = Fe, **5**; Co, **6**) reveal that intermolecular interactions are a significant factor in structure disorder in the three metalloporphyrins and phase changes in the nitrosyl complexes. These interactions cause, *e.g.*, an 8-fold disorder in the crystal structures of [M(TPP)(NO)] at room temperature that obscures the M-NO binding. Hirshfeld analyses of the structure of [Co(TPP)(NO)] (**6**) indicate that the phase change from *I*4/*m* to *P*-1 leads to an increase in void-volume percentage, permitting additional structural compression through tilting of the phenyl rings to offset the close-packing interactions at the interlayer positions in the crystal structures with temperature decrease. X-ray and neutron structure studies of [Fe(TPP)Cl] (**1**) at 293, 143 and 20 K reveal a tilting of the phenyl groups away from being perpendicular to the porphyrin ring as a result of intermolecular interactions. Structural similarities and differences among the three complexes are identified and described by Hirshfeld surface and void-volume calculations.

3.1. Introduction

A key structural feature of the O_2-free hemes in hemoglobin and myoglobin is that the active center contains a five-coordinate Fe-porphyrin. In both proteins, O_2 binds to the iron atom, turning the five-coordinate heme into a six-coordinate complex. Five-coordinate Fe-porphyrin systems[1-3] such as [Fe(TPP)Cl] (**1**) (Figure 3.1) have thus been actively studied to provide insight into the physical and chemical properties of the hemes.[4-10] The first reported structure of [Fe(TPP)Cl] (**1**) was incorrectly solved as [Fe(TPP)(OH)]·(H_2O) in the *I*4 space group.[4a] This structure was re-analyzed by Hoard *et al*. in the higher symmetry *I*4/*m* space group as [Fe(TPP)Cl] (**1**).[4b] Monoclinic [Fe(TPP)Cl] (**1**) crystals in the $P2_1/n$ space group were obtained by Scheidt *et al*. through decomposition of [Fe(TPP)(NO)] (**5**) in a CH_2Cl_2 solution containing nitrate and nitrite ions.[9] A structure of [Fe(TPP)Cl] (**1**) at 100 K, in the *I*4/m space group, was solved by Scheidt and coworkers.[11] Most recently [Fe(TPP)Cl] (**1**) at 293 K was refined in the *I*4 space group by Hadjikakou *et al*. with two superimposed independent molecules having different distances of the Fe atom to the plane defined by the four N atoms of the porphyrin.[12]

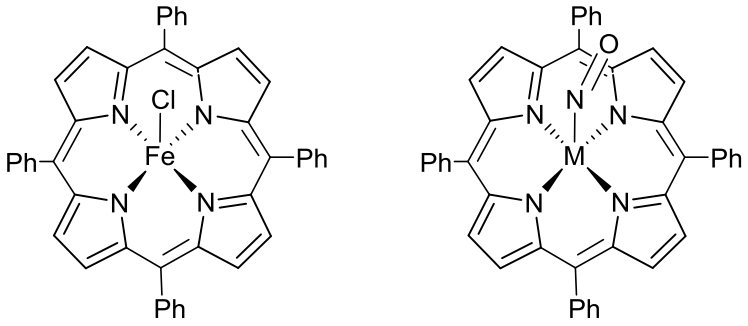

Figure 3.1. [Fe(TPP)Cl] (**1**) and [M(TPP)(NO)] (M = Fe, **5**; Co, **6**).

Nitric oxide (NO) is a vital cellular signaling agent in many physiological and pathological processes.[13] Its coordination to heme proteins is involved in several fundamental processes such as neuronal communication,[14] muscle relaxation,[15] platelet deaggregation,[16] and myocardial function.[17] Five-coordinate Fe-NO porphyrins are active complexes in the signaling events. The nitrosyl metalloporphyrins [M(TPP)(NO)] (M = Fe, **5**; Co, **6**) were first synthesized and characterized by Scheidt *et al*. about 40 years ago.[18] These two complexes, displaying tilted M-NO binding, provided the initial insight into the coordination chemistry of nitric oxide to metalloporphyrins. However, both complexes crystalize in the tetragonal *I*4/*m* space group with 8-fold disorder of the O atom in the NO ligand at room temperature, significantly obscuring the binding of NO to Fe or Co atoms and the structure features of the complexes.[11,13g,18] Electronic and vibrational properties of the complexes and their structures, including the tilted binding and dynamics of the NO ligands on the complexes have also been studied.[13d,19] Recently, the structures have been investigated by VT X-ray diffraction[11,13g] and DFT calculations.[19a] Both species were found to undergo a lowering of the space-group symmetry from tetragonal *I*4/*m* to the triclinic *P*-1, upon lowering of the temperature. From bond-length and angle analysis no clear benefit could be identified, and it is thus not obvious why the phase changes occur.[11,13g]

We have studied VT X-ray and neutron structures of [Fe(TPP)Cl] (**1**) and used the Hirshfeld surface analysis for the crystal structures of [Fe(TPP)Cl] (**1**) and [M(TPP)(NO)] (M = Fe, **5**; Co, **6**). We chose these two nitrosyl compounds for comparison with [Fe(TPP)Cl] (**1**) where the symmetric Cl can be juxtaposed to the asymmetric NO ligand and iron can be contrasted to cobalt as the central atom. The Hirshfeld surface analysis,

recently developed by Spackman and coworkers, allows for the comparison of molecular structures by examining interactions of an individual molecule with its nearest neighbor molecules while maintaining a whole-of-molecule approach.[20-22] A Hirshfeld surface is an isosurface calculated from the weight function $w(\boldsymbol{r})$ of the sum of spherical atom electron densities (Eq. 3.1);

$$w(\boldsymbol{r}) = \frac{\rho_{promolecule}(\boldsymbol{r})}{\rho_{procrystal}(\boldsymbol{r})} = \sum_{A \in molecule} \rho_A(\boldsymbol{r}) / \sum_{A \in crystal} \rho_A(\boldsymbol{r}) \qquad \text{(Eq. 3.1)}$$

where $\rho_{promolecule}(\boldsymbol{r})$ is the sum of the molecular electron density over the atoms in the molecule of interest (the promolecule) and $\rho_{procrystal}(\boldsymbol{r})$ is the similar sum over the crystal (the procrystal).[20-22]

The isosurface separates a molecule (promolecule) from its nearest neighbors (procrystal) at a given density level. From the Hirshfeld surface, distances to the nearest atoms outside (external), d_e, and inside (internal), d_i, are readily defined, and the surface gives a visual 3-*D* representation of the intermolecular close contacts in the crystal. Using the d_e,d_i pairs, the Hirshfeld surface can be reduced to a 2-*D* histogram, giving a unique fingerprint plot for intermolecular interactions in the crystal.[21,22] Void volumes in the crystal can be readily determined using the same isosurfaces of electron density, by looking at areas in the crystal where the electron density is the lowest.[23] Other earlier methods, in comparison, rely on the approximation of a molecule as a set of fused spheres with van der Waals radii and are thus limited in scope.[20-23] Hirshfeld surface analysis has been used to explore permanent voids, cavities, and channels in porous materials such as

MOFs (Metal-Organic Frameworks) and COFs (Covalent Organic Frameworks).[23] Hirshfeld surface analysis is an excellent tool to compare compounds with respect to their molecular environment and interactions independent of the overall space group symmetry. The Hirshfeld surface and void volume analyses of the crystal structures of [Fe(TPP)Cl] (**1**) and [M(TPP)(NO)] (M = Co, **6**; Fe, **5**) in the current work provide an understanding of their crystal and molecular structures at room and lower temperatures and, more importantly, the phase changes in [M(TPP)(NO)]. These analyses show that intermolecular interactions lead to the observed disorders at room temperature in [M(TPP)(NO)] and their phase changes at lower temperatures, affecting both their structures and the dynamics of the NO ligand rotation. Without the use of Hirshfeld analyses, it is difficult to describe the structure changes in the nitrosyl complexes in a comprehensive manner, as the phase changes involve different space groups ($I4/m \rightarrow P\text{-}1$).[11,13g]

Part of the research reported here, mainly the collection of X-ray and neutron diffraction data for [Fe(TPP)Cl] (**1**), was performed by Brenda A. Dougan, a previous member of our group. Her synthesis of **1**, diffraction data collection, and structure determination are copied below so the work is presented in its entity. The diffraction data have been reanalyzed in the current work using the Hirshfeld surface analysis.

3.2. Experimental

3.2.1 Synthesis[24]

[Fe(TPP)Cl] (**1**), purchased from Strem Chemicals, and solvents (Analytical Reagents) were used without further purification. [Fe(TPP)Cl] (**1**) was also prepared by

modified published procedures.[4b] Wet chloroform was prepared by adding water to chloroform (Certified ACS), and the mixture was shaken and then allowed to settle. Wet chloroform at the bottom was then removed for the use below.

[Fe(TPP)Cl] (**1**) (0.05 mmol) was dissolved in wet chloroform (4 mL) and layered with a 1:3 wet chloroform:absolute ethanol mixture (4 mL). The sample container was sealed with parafilm. After the layers had completely diffused together - in ca. 5-7 days - the solution was allowed to evaporate very slowly for ca. additional 7 days. Crystals of sizes up to $1 \times 2 \times 2$ mm^3 were observed and collected. This procedure gave consistently disordered crystals with a slight asymmetric occupancy (ca. 0.40:0.60) of the Fe-Cl part, as discussed below.

3.2.2 Diffraction Data Collection

X-ray diffraction data at 293(2) and 143(2) K were collected on a Bruker AXS Smart 1000 X-ray diffractometer equipped with a CCD area detector and a graphite-monochromated Mo source (K_α radiation, 0.71073 Å) and fitted with an upgraded Nicolet LT-2 low-temperature device (SMART APEX II systems; Precision Cryogenic Systems Inc.). A suitable crystal of size $0.50 \times 0.20 \times 0.10$ mm^3 was coated with Paratone-N^{TM} oil (Exxon Chemical Americas, Houston, Texas) and mounted on a glass fiber.

The lowest temperature synchrotron X-ray diffraction data were collected on another crystal at 20(2) K on a Bruker D8 diffractometer on the ChemMatCARS beam line at the Advanced Photon Source/Argonne National Laboratory (APS/ANL).[25] The diffractometer is equipped with a Bruker 6000 CCD detector. The crystal was coated with

Paratone-N^{TM} oil (Exxon) and mounted on a glass fibre and measured under a stream of helium at 20(2) K.

Global refinements for the unit cell and data reduction were performed with the SAINT program for the X-ray diffraction data collected at 293(2) K and 143(2) K.[26] Cell refinement and data reduction for the X-ray data at 20(2) K were carried out using the APEX2 program package.[27] Empirical absorption correction was performed with SADABS.[28] The space group for structure solution and refinement was determined from systematic absences using XPREP.[26]

Neutron diffraction data of [Fe(TPP)Cl] (**1**) were collected at 20(0.2) K on a 1.5 × 1.0 × 1.0 mm^3 tetragonal bipyramidal crystal on the four-circle diffractometer D9 at the Institut Laue-Langevin, Grenoble, France, in a beam of wavelength 0.8387(2) Å obtained by reflection from a Cu(220) monochromator. D9 is equipped with a small two-dimensional area detector, whose main advantage for this measurement was to allow optimal delineation of the peak from the considerable background due to the large proportion of H atoms in this sample.[29] To avoid strain while cooling, the crystal was wrapped in Al foil before being glued to a V pin and mounted in a closed-cycle He refrigerator. Two equivalents of most unique reflections to 0.68 Å^{-1} in $\sin\theta/\lambda$ were collected at 20(0.2) K. For all data, background corrections following the method of Wilkinson *et al*.[30] as well as Lorentz corrections were applied. Absorption corrections were made by Gaussian integration using the calculated attenuation coefficient μ = 0.112 mm^{-1}, with account taken of the absorption for hydrogen atoms[31,32] with transmission range 0.852-0.891. A total of 1901 independent reflections were collected.[31,32]

3.2.3. Structure Determination

X-ray structures of [Fe(TPP)Cl] (**1**) at 293, 143, and 20 K were solved by direct methods using SHELXS and refined using the SHELXTL proprietary software package.[33] The neutron structure at 20 K was refined using SHELX97.[33] Non-H atoms in all data and the H atoms in the neutron data were refined with anisotropic displacement parameters. C and H atoms in the disordered phenyl ring were refined with distance constraints. For the X-ray data, H atoms were placed at calculated positions, with isotropic displacement parameters constrained to the equivalent isotropic displacement parameters of the connected C atoms [U_{iso}(H) = 1.2U_{eq}(C)]. The structures were checked using PLATON.[34] Crystal data and structural refinement details are given in Table 3.1. Bond lengths and angles are given in Table 3.2.

3.2.4. Hirshfeld Surface Calculations

Hirshfeld surfaces, fingerprint plots, and void volumes were calculated using CrystalExplorer (version 3.1) software from the crystal-structure coordinates supplied in the format of crystallographic information file (CIF).[35] The X-ray CIF files of [Fe(TPP)Cl] (**1**) from the current work and in the literature were used.[9a,11,12] For [Fe(TPP)(NO)] (**5**) and [Co(TPP)(NO)] (**6**), the published CIFs were used.[13g,11] Hirshfeld surfaces were calculated at an isovalue of 0.5 e au^{-3}. Void volumes were calculated using an isovalue of 0.002 e au^{-3}.[23]

3.3. Results and Discussion

3.3.1. Crystal and Molecular Structures of [Fe(TPP)Cl] (1) at 293, 143, and 20 K[24]

For detailed structure comparison, it is important to look at the specific point group symmetry of the molecules with respect to the overall structure symmetry. The Fe(III) ion in the [Fe(TPP)Cl] (**1**) molecule is five-coordinated with apical Cl and four N of the planar porphyrin ligand on the mirror plane perpendicular to the *c*-axis. Due to the asymmetric coordination, the Fe atom moves about 0.39 Å out of the porphyrin plane towards the Cl atom to give an idealized C_{4v} point-group symmetry. The porphyrin plane holds four phenyl rings at 90° to the plane. For the crystal structure reported in the *I*4/*m* space group,[4b] the origin (0,0,0) is at the center of the planar porphyrin with overall idealized C_{4h} point-group symmetry. The crystal site symmetry at the origin is higher than the C_{4v} symmetry for a single ordered [Fe(TPP)Cl] (**1**) molecule. The apparent higher site symmetry imposes a 50:50 disorder of the axial Fe-Cl part above and below the porphyrin plane in the *I*4/*m* structure. Since the porphyrin ring of the TPP^{2-} ligand is rigid and prefers planar symmetry with all atoms located on the mirror plane,[36] it leaves only two C (and the associated H) atoms of the connected phenyl rings on the general positions above and below the mirror plane to respond freely to physical restraints imposed by decreasing temperature and rotate with respect to the porphyrin plane.

The [Fe(TPP)Cl] (**1**) X-ray structure at 293 K (Figure 3.2a) can be refined in space group *I*4/*m* in full agreement with the previously reported room-temperature structure[4b] but we found that the crystal structure refinement significantly improves in the space group *I*4 with a decrease in *R*1 value from 0.0620 to 0.0318. At this temperature the porphyrin ring is perpendicular to the *c* axis within error. The disordered Fe-Cl part above

and below the porphyrin plane shows a slight asymmetry in distance from the porphyrin plane (0.33 Å vs. 0.49 Å) and occupancy [0.363(1):0.637(1)], deviating significantly from the 0.5:0.5 ratio imposed by the C_{4h} site symmetry in $I4/m$. At 143 K the mean tilt of the phenyl group plane in $I4$ is 2.8(1)°. The refined residual values in $I4$ are $R1$ = 0.0481 and w$R2$ = 0.1487. The X-ray structure at 20 K was refined against extensive high-resolution synchrotron data and the agreement indices $R1$, $wR2$ [$I > 2\sigma(I)$], S are 0.0352, 0.1092, 1.004, respectively. The site-occupancy ratio for the disordered Fe-Cl part was refined to 0.4084(5):0.5916(5). The phenyl-ring tilt follows the Fe-Cl disorder distribution, and the mean planes of the two disordered phenyl groups are now tilted 6.8(1)° for the major component and 7.7(2)° for the minor component, respectively. As shown in Figure 3.4, the phenyl rings tilt away from the chloride ligand, a point discussed later.

The neutron structure at 20 K confirms the $I4$ space group symmetry with comparable residual values of $R1$ = 0.0399, $wR2$ = 0.0757 and S = 1.137. The coordinates, equivalent isotropic displacement parameters, and the bond lengths and angles for the non-H atoms are within three combined standard deviations of those calculated from X-ray diffraction data at 20 K. The observed tilt angle of the phenyl ring away from the c axis is 6.74(9)° and 10.7(3)° for the major and minor components, respectively. The small differences between the X-ray and neutron refinements might be explained by our use of a larger crystal from a different batch for the latter. Figure 3.4 demonstrates the two configurations of the Fe-Cl part with a slightly asymmetric tilting of the phenyl rings away from the c axis at 20 K, breaking the mirror symmetry in the ab plane.

In contrast to the reported structure of [Fe(TPP)Cl] (**1**) in *I*4/*m* at 100 K,[11] the uneven, ca. 40/60, distribution of the disordered Fe-Cl part on both sides of the porphyrin plane in our structures reveals that the true structure symmetry is *I*4. In addition, the large number of high-resolution data collected at the synchrotron source at 20 K, especially the high-angle data, allow a better determination of the thermal vibrations than the lower-resolution data using a typical home-source X-ray diffractometer, and refines more accurately the occupancy ratio of the disordered Fe–Cl group, *vide supra*.

Our VT study also revealed the nature of a static disorder of the porphyrin ligand. The out-of-plane phenyl C atoms (C7, C8, C10, and C11) were found disordered in two positions about a common plane parallel to the *c* axis. The disorder becomes noticeable at 143 K and evident at 20 K, as shown in Figure 3.5. Examining the thermal-ellipsoid elongation parallel to the mirror plane by the ratio of U_{max}/U_{min} further elucidates the trend of distortion of the refined structure model. The variation of the displacement parameters with temperature is plotted in Figure 3.6. The ratio in *I*4/*m* increases from 2.48 at 293 K to 2.64 at 143 K and doubles to 5.34 at 20 K. However, U_{max}/U_{min} in the refinements in *I*4 increases at a negligible rate (2.53_{293K}, 2.63_{143K}, 2.83_{20K}) over the same temperature range. This supports the symmetry *I*4 with a static disorder model especially at the low temperature. Alternatively, this trend can be described by the distances between the disordered pairs of carbon atoms C7 and C7′, and C8 and C8′. There is no apparent separation at 293 K, while the distance between C7 and C7′ (as well as C8 and C8′) increases to 0.053 Å at 143 K and further to ca. 0.16 Å at 20 K. The increase in separation distance Δd (Å) with cooling and the “freezing out” of the atomic

Table 3.1. Comparison of crystal data and structural refinement (chemical formula: $FeN_4C_{44}H_{28}Cl$; M_r: 704.00).

Space group	*I*4/*m*	*I*4	*I*4/*m*	*I*4	*I*4	*I*4
Temperature (K)	293(2)		143(2)		20(2)	20(2)
a (Å)	13.5374(2)		13.504(3)		13.4830(5)	13.4761(6)
c (Å)	9.8247(2)		9.731(10)		9.6849(6)	9.6889(6)
V (Å^3)	1800.49(5)		1774.5(19)		1760.63(14)	1759.56(16)
Z	2		2		2	2
Radiation type	Mo K_α		Mo K_α		Synchrotron	Neutron
Wavelength (Å)	0.71073		0.71073		0.41328	0.83880(2)
μ (mm^{-1})	0.530		0.538		0.288	0.112
Crystal size (mm^3)	0.70 × 0.20 × 0.10		0.50 × 0.20 × 0.10		0.04 × 0.04 × 0.04	1.50 × 1.00 × 1.00
No. of measured, unique and observed [$I > 2\sigma(I)$] reflections	9622, 1154, 1099	9622, 2120, 2015	7976, 1106, 1009	7973, 2002, 1772	36372, 11751, 10231	1893, 1263, 1045

Table 3.1. Continued

Space group	*I*4/*m*	*I*4	*I*4/*m*	*I*4	*I*4	*I*4
R_{int}	0.0169	0.0165	0.0593	0.0536	0.0488	0.0286
R [$F^2 > 2\sigma(F^2)$], $wR(F^2)$, S	0.0620, 0.1627, 1.291	0.0318, 0.0885, 1.059	0.0749, 0.2113, 1.229	0.0481, 0.1487, 1.062	0.0352, 0.1092, 1.004	0.0399, 0.0757, 1.137
No. of reflections	1154	2120	1106	2002	11751	1263
No. of parameters	74	119	74	120	136	194
No. of restraints	0	1	0	1	18	52
$\Delta\rho_{max}$, $\Delta\rho_{min}$ (e Å^{-3} or fm Å^{-3})	0.259, -0.253	0.213, -0.261	0.489, -0.396	0.427, -0.316	0.707, -0.512	0.543, -1.114
Fe-Cl occupancy: Minor:Major		0.363(1):0.637(1)		0.367(2):0.633(2)	0.4084(5):0.5916(5)	0.39(2):0.61(2)

Computer programs: Bruker *APEX2*, Bruker *SAINT*, *SHELXL97*,[27] Bruker SHELXTL.

(a) 293 K

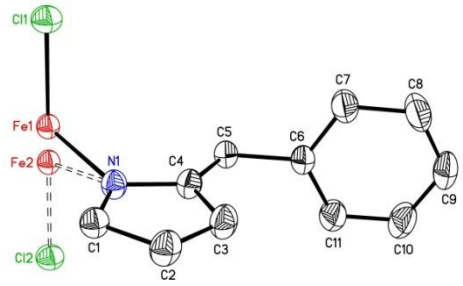

(b) 143 K

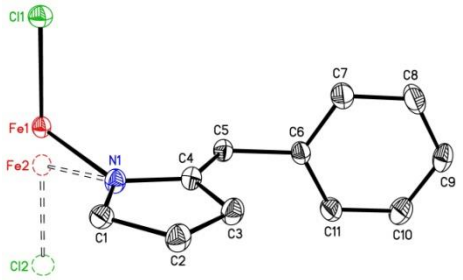

(c) 20 K

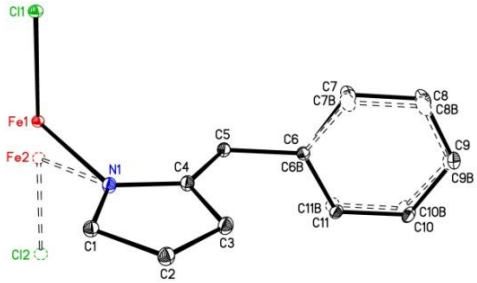

Figure 3.2. ORTEP drawings of the asymmetric unit of [Fe(TPP)Cl] (**1**) in *I*4 from X-ray diffraction. Thermal ellipsoids are drawn at the 30% probability level. H atoms were omitted for clarity. Disordered atoms are drawn in dash lines.

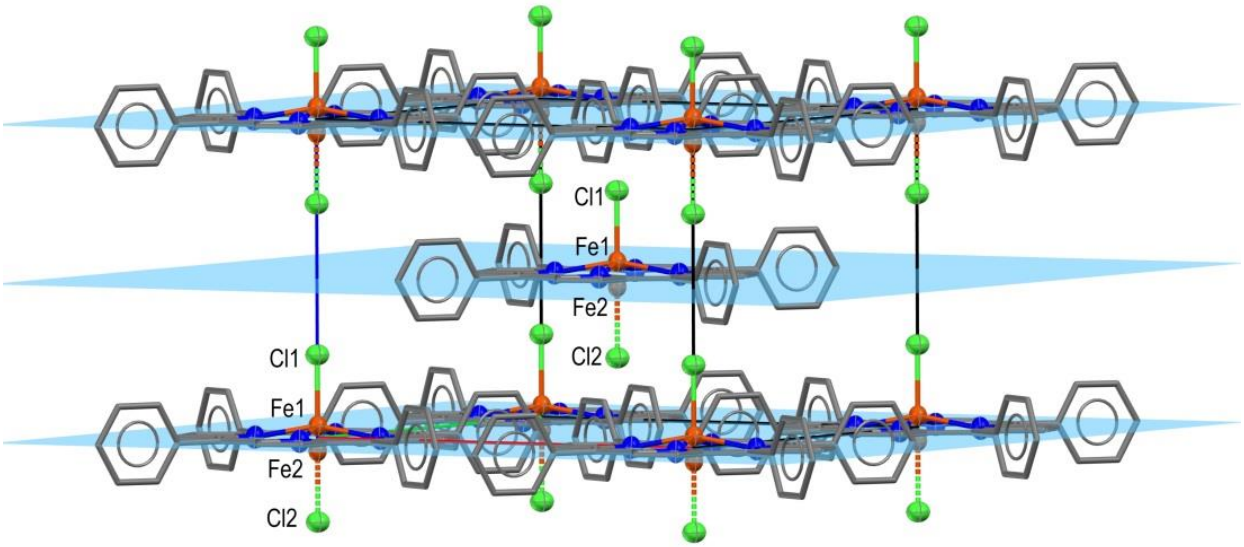

Figure 3.3. Stacking plot of [Fe(TTP)Cl] (**1**) at 293 K showing the disorder of Fe−Cl along the *c* axis (red: Fe, blue: N, green: Cl, gray: C).

positions is also displayed in Figure 3.6. The disorder behavior of C10 and C11 mirrors that of C7 and C8 and is therefore not described separately.

The cell volume and parameters decrease as expected from 1800.49(5) $Å^3$ at 293 K [*a* = 13.5374(2) Å, *c* = 9.8247(2) Å], to 1774.5(19) $Å^3$ at 143 K [*a* = 13.504(3) Å, *c* = 9.731(10) Å, and 1760.63(14) $Å^3$ at 20 K [*a* = 13.4830(5) Å, *c* = 9.6849(6) Å]. However, the percentage decrease in the *c* axis (1.4% from 293 to 20 K) is three times as large as the percentage decrease in the *a* axis, as a consequence of the tilting of the phenyl rings, allowing a tighter layer packing along the *c* axis.

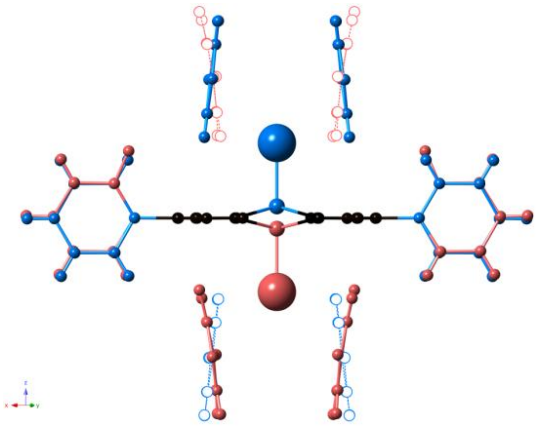

Occupancy/configuration: Blue: 0.4073(6)
Red: 0.5927(6)

Figure 3.4. Plot of the disorder in phenyl groups of [Fe(TPP)Cl] (**1**) at 20 K (X-ray).

Filled or empty spheres represent the associated or opposing phenyl rings, respectively.

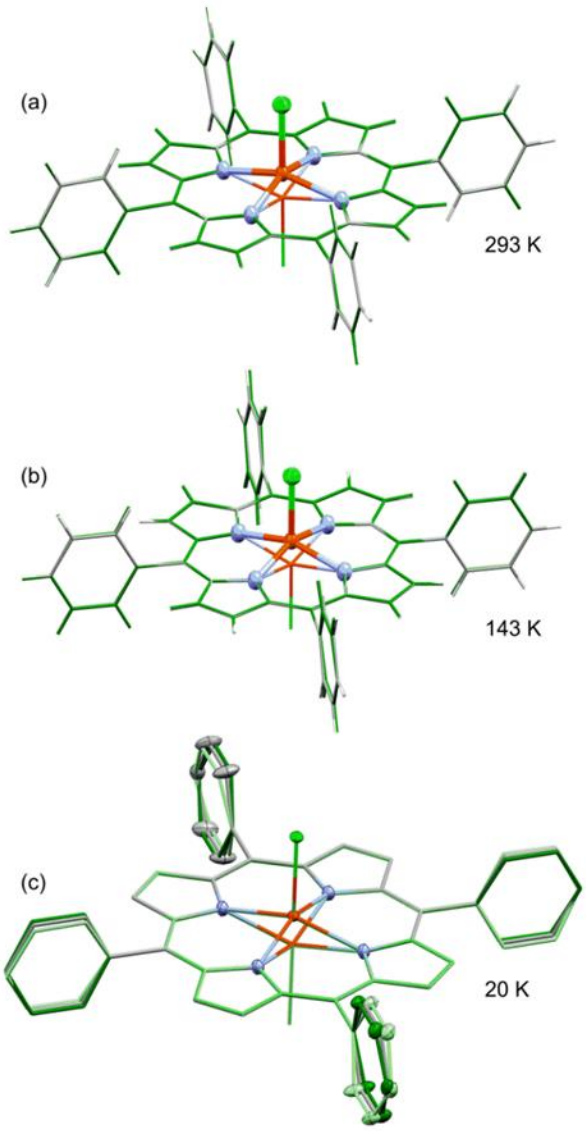

Figure 3.5. Diagram overlapping the X-ray structures of **1** refined in *I*4 and *I*4/*m* at (a) 293 K, (b) 143 K and (c) 20 K. The phenyl groups in gray are in the plane perpendicular to the porphyrin ring as defined by the *I*4/*m* symmetry. The phenyl groups in green are tilted out of plane, in the lower symmetry *I*4. Thermal ellipsoids of Fe, Cl and N atoms and the disordered phenyl C atoms are shown at the 30% probability level. The disordered C atoms are plotted in gray for the *I*4/*m* and green for the *I*4 refinement for the 20 K structure. H atoms are omitted for clarity.

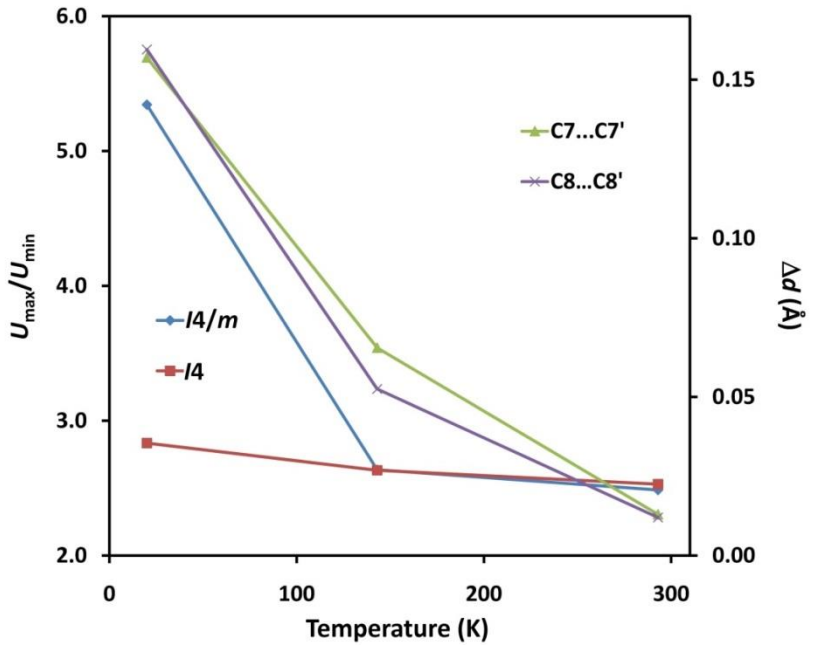

Figure 3.6. Graph showing changes, with temperature, of the thermal-ellipsoid distortion ratio (U_{max}/U_{min}) in *I*4/*m* and *I*4 (left axis) and the C7–C7′ and C8–C8′ distances of the phenyl ring (right axis).

Table 3.2. Comparison of bond lengths (Å) and angles (°) of [Fe(TPP)Cl] (**1**) from X-ray diffraction at 20, 143, and 293 K in *I*4.

Temperature (K)	293	143	20
Fe···Fe	0.779(1)	0.791(2)	0.7891(3)
Fe-Cl1	2.191(3)	2.175(5)	2.2004(5)
Fe-N1	2.049(1)	2.052(2)	2.0581(3)
N-C1	1.380(2)	1.382(2)	1.3826(4)
N-C4	1.381(2)	1.384(2)	1.3833(4)
C3-C4	1.435(2)	1.439(2)	1.4430(5)
C4-C5	1.394(2)	1.401(2)	1.4014(5)
C5-C6	1.497(2)	1.502(2)	1.4968(4)
Fe1-N-C1	126.31(9)	126.32(12)	126.22(2)
Fe1-N-C4	126.34(9)	126.41(12)	126.20(2)
C1-N-C4	105.87(10)	105.72(14)	105.91(3)
C3-C4-C5	124.60(13)	124.70(16)	124.23(3)
N-C4-C5	125.73(12)	125.45(16)	125.73(3)
C4-C5-C6	117.51(12)	117.41(16)	117.93(3)
C5-C6-C7	120.2(2)	120.4(3)	121.1(2)

Table 3.3. Hydrogen bonds from neutron data of [Fe(TPP)Cl] (**1**) at 20 K

D-H...A	d(D-H) (Å)	d(H...A) (Å)	d(D...A) (Å)	<(DHA) (deg)
C(7)-H(7)...C(3)#9	1.092(9)	2.780(13)	3.632(7)	134.8(9)
C(8)-H(8)...C(1)#9	1.095(19)	2.86(2)	3.826(6)	146.5(12)
C(8)-H(8)...N(1)#9	1.095(19)	2.80(2)	3.788(5)	150.0(16)
C(8)-H(8)...Cl(2)#10	1.095(19)	2.605(15)	3.274(6)	118.6(10)
C(10)-H(10)...Cl(1)#10	1.073(14)	3.061(13)	3.452(5)	102.2(8)
C(10)-H(10)...C(1)#10	1.073(14)	2.736(15)	3.766(6)	160.9(12)
C(11)-H(11)...C(3)#10	1.085(12)	2.795(15)	3.668(7)	137.4(10)

Symmetry transformations used to generate equivalent atoms:

#1 -x,-y,z #2 y,-x,z #3 -y,x,z #4 x,y,z+1

#5 -x,-y,z+1 #6 -y,x,z+1 #7 y,-x,z+1 #8 x,y,z-1

#9 -x+1/2,-y+1/2,z+1/2 #10 -x+1/2,-y+1/2,z-1/2

#11 y,-x+1,z

3.3.2 Hirshfeld Surface Analysis of the Crystal Structures of [Fe(TPP)Cl] (1)

Crystal structure analyses above indicate a gradual hardening of the phenyl-ring position into two distinct conformations with cooling. Hirshfeld surface analyses of the current and previously reported *I*4[12] and *P*2$_1$/*n* structures[9] have been used to provide further insight.

Hirshfeld surfaces of our crystal structure of [Fe(TPP)Cl] (**1**) at 293 K are given in Figure 3.7. Such surfaces at 143 and 20 K are given in Figure 3.8, revealing the development of close-contact sites with temperature. The Hirshfeld volume and surface area of our 293 K structure, 888.55 Å^3 and 677.40 Å^2, respectively, are very similar to 893.18 Å^3 and 677.52 Å^2 of the reported *I*4 structure at 293 K.[12] The reported monoclinic *P*2$_1$/*n* structure,[9a] used as a baseline comparison here, is more compact with a significantly smaller Hirshfeld volume and surface area, 840.26 Å^3 and 655.38 Å^2, respectively.[9a] The fingerprint plots for our room-temperature *I*4 and the monoclinic *P*2$_1$/*n* structures in Figures 3.9a-9b (H···H close contacts) and 3.9c-9d (Cl···H close contacts) reveal distinctly different shapes, reflecting the molecular stacking of parallel layers for the former and a herringbone arrangement for the latter. The Cl···H contacts are further apart in the monoclinic structure and contribute significantly less to the Hirshfeld surface than those in the tetragonal structure (Figure 3.11). A less-strained monoclinic structure is favored by larger axial Br$^-$ and I$^-$ ligands {[Fe(TPP)Br] in *P*2$_1$/*c*;[37] [Fe(TPP)I] in *P*2$_1$/*n*[38]}. Tetragonal structures predominate for smaller halides F$^-$ {in [Fe(TPP)F][39]} and Cl$^-$.

It has been reported that the phenyl rings tilt in the structure of [Co(TPP)Cl] as a result of intermolecular interactions.[40] We have investigated how phenyl rings tilt in the iron analog [Fe(TPP)Cl] (**1**) and separated two phenyl tilt options,[41] towards or away from

the Cl ligand, in our 20 K X-ray structure to give two Hirshfeld fingerprint plots emphasizing close intermolecular Cl⋯H contacts (Figure 3.12). The plots show two significantly different contacts: (a) 2.7018 Å (Figure 3.12a) with a void volume of 336.24 $Å^3$ when the phenyl rings tilt *towards* the chloride; (b) 3.966 Å (Figure 3.12b) with a void volume of 325.51 $Å^3$ when the phenyl rings tilt *away* from the chloride. The larger void volume in (a) accompanies the shorter contact of 2.7018 Å. This distance is smaller than the sum of the Van der Waal radii of H (1.20 Å) and Cl (1.75 Å) atoms,[42] and the close proximity prohibits further tilting and compression. The opposite tilting in (b) provides a comfortable distance and has room for further tilt. Both considerations make the configuration in (a) unlikely and prefer (b) where the Cl and H atoms are further away from each other.

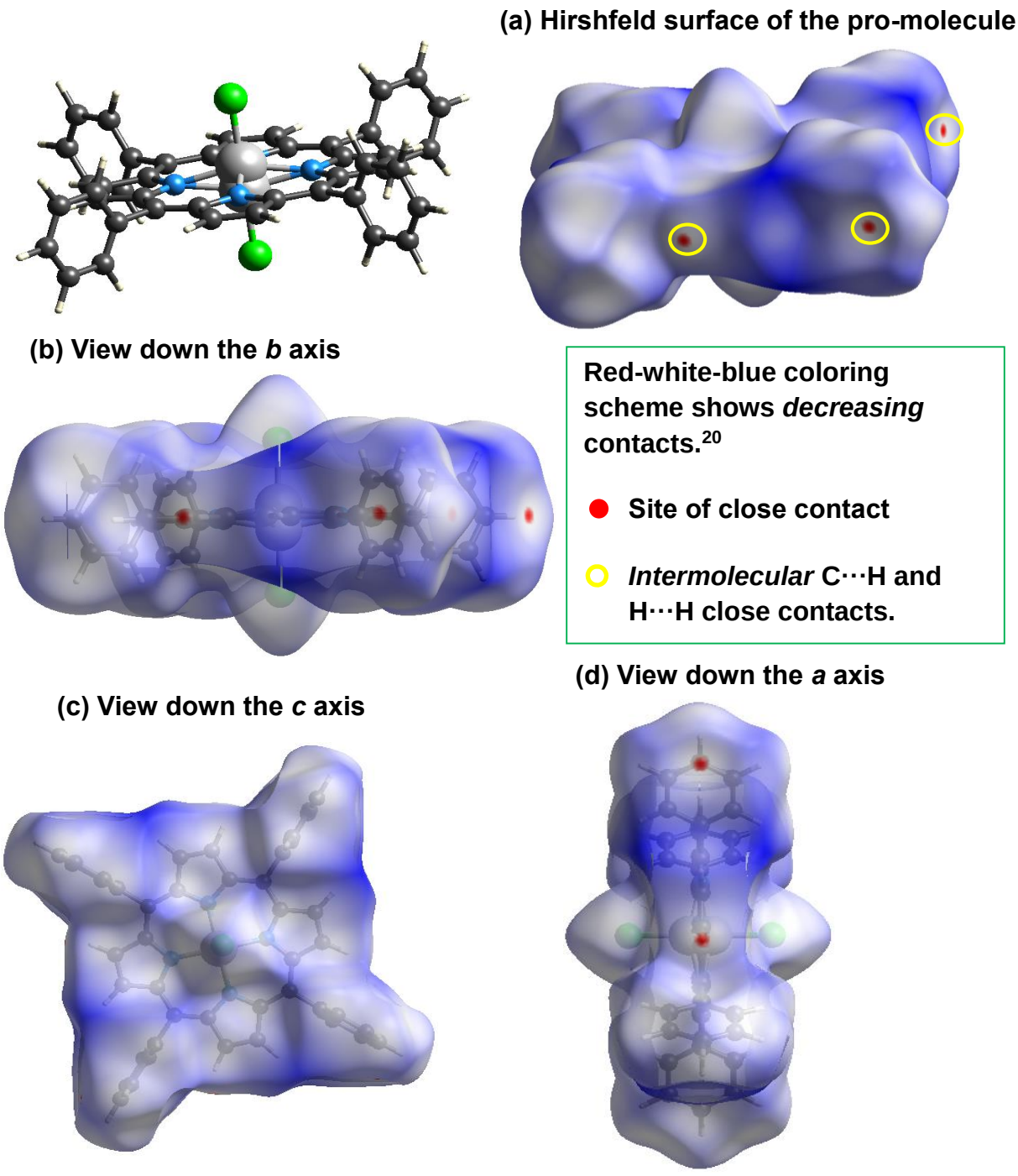

Figure 3.7. Hirshfeld surface of [Fe(TPP)Cl] (**1**) showing normalized close distances of the pro-molecule and neighboring molecules at 293 K. Semi-transparent showing the enclosed molecule.

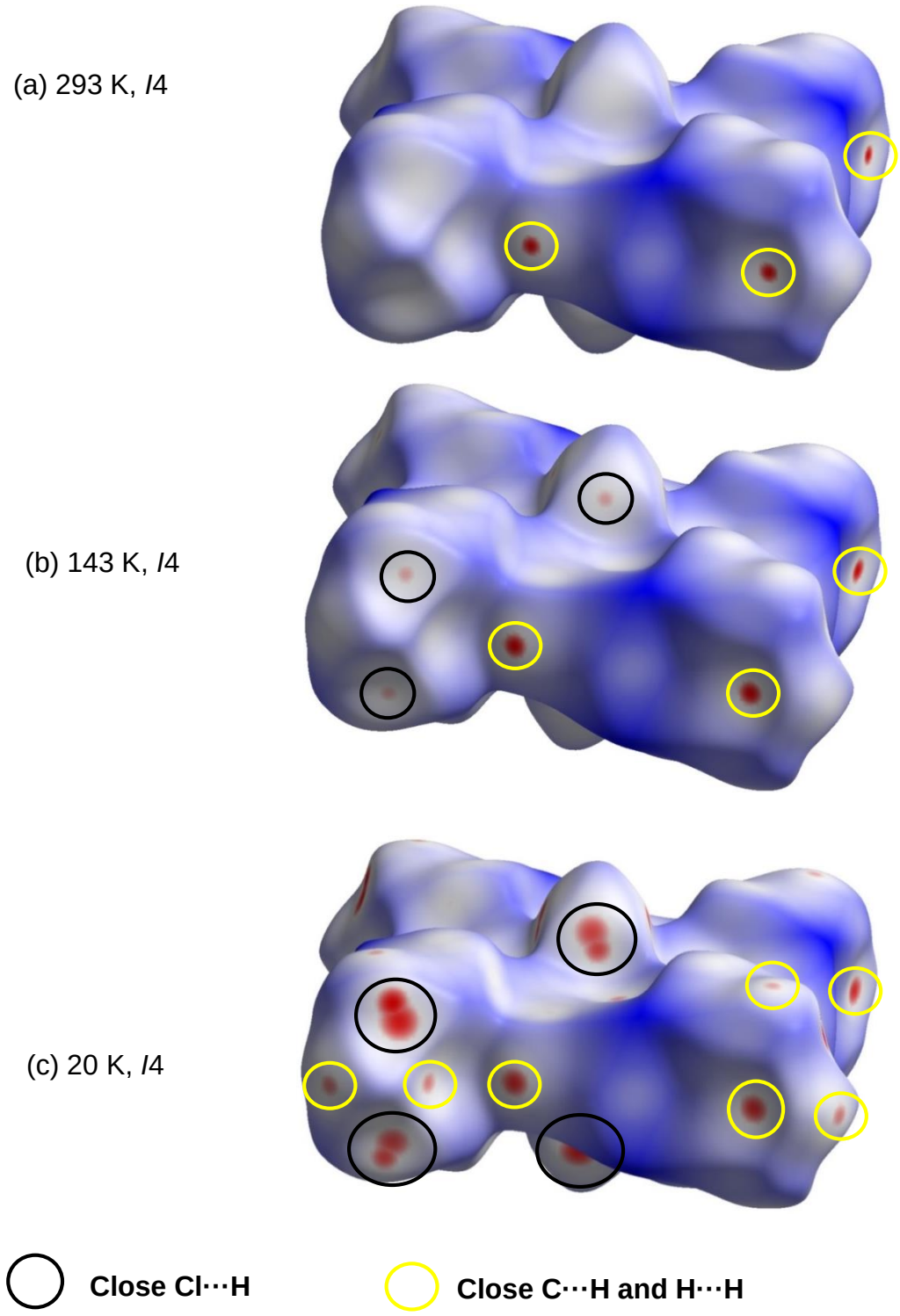

Figure 3.8. Hirshfeld surfaces of [Fe(TPP)Cl] (**1**) at 293, 143 and 20 K. The surface at 293 K is shown in Figure 3.7 and is reproduced here for comparison.

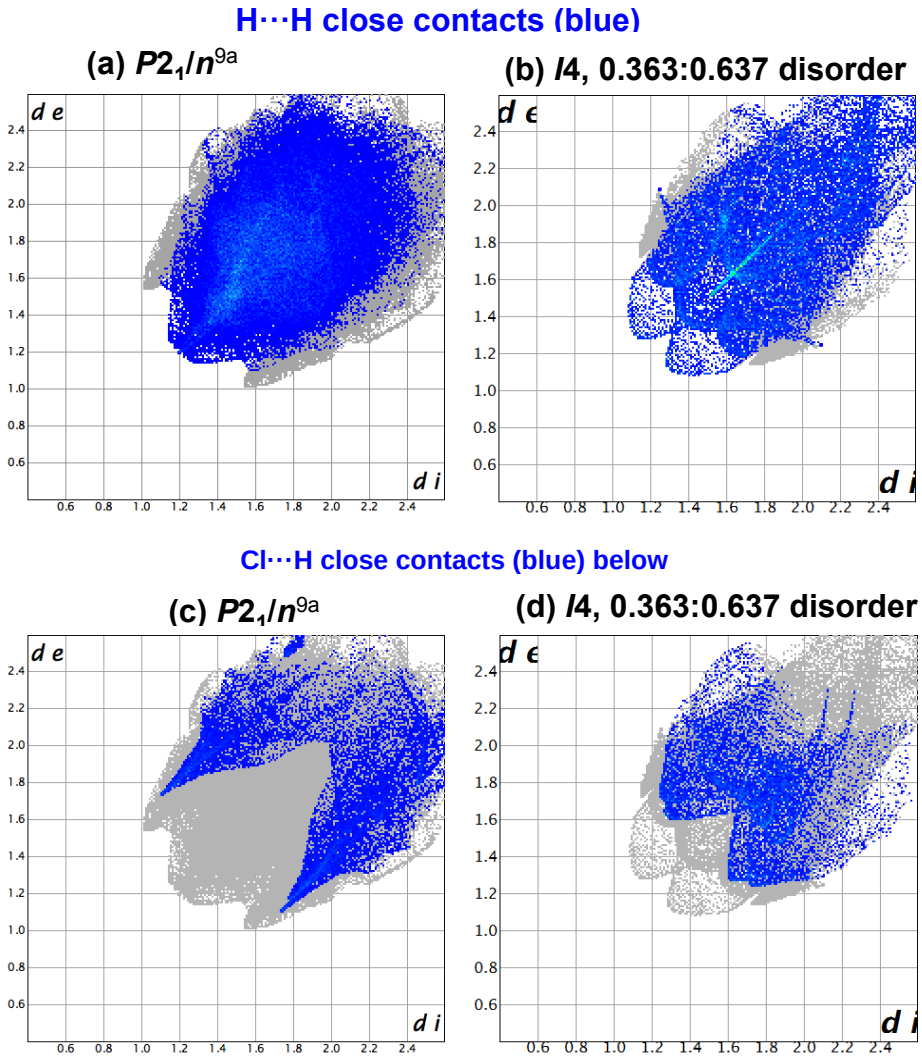

Figure 3.9. Hirshfeld fingerprint plots for the [Fe(TPP)Cl] (**1**) structures at 293 K in $P2_1/n$[9a] and $I4$ from the current work. The closest contacts correspond to the minimum values of d_e+d_i in each plot, e.g., 2.8 Å for Cl···H in (c) and 2.9 Å for Cl···H in (d).

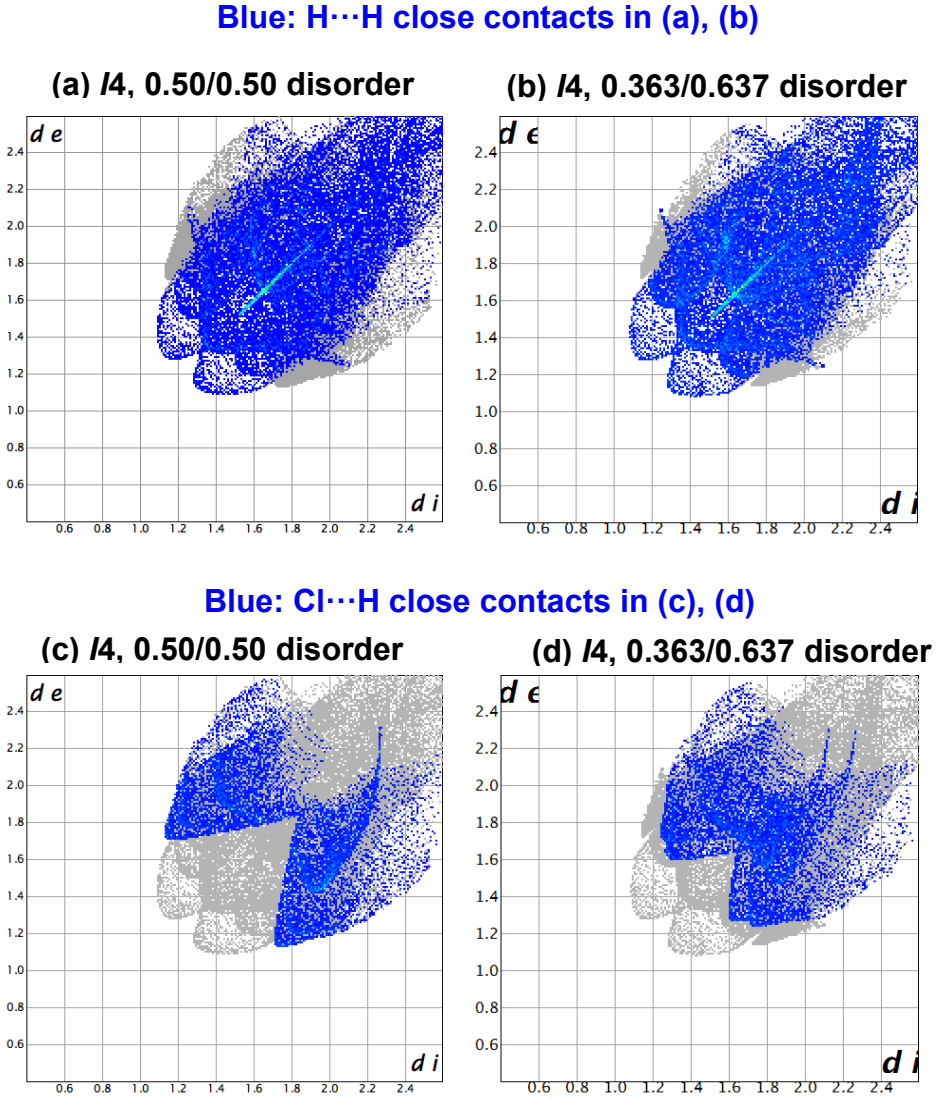

Figure 3.10. (a)-(b) Hirshfeld fingerprint plots showing the H···H close contacts in blue for the two tetragonal room temperature crystals. (c)-(d) Plots showing the Cl···H close contacts in blue for the two tetragonal room temperature structures of [Fe(TPP)Cl] (**1**). (a) and (c): *I*4, 0.50/0.50 disorder involving two independent molecules;[12] (b) and (d): *I*4, 0.363/0.637. The two *I*4 structures are nearly identical, except for the Cl···H contacts. The 0.50/0.50 structure has closer intermolecular Cl···H contacts (~2.8 Å) than that (~3 Å) in the 0.363/0.637 structure.

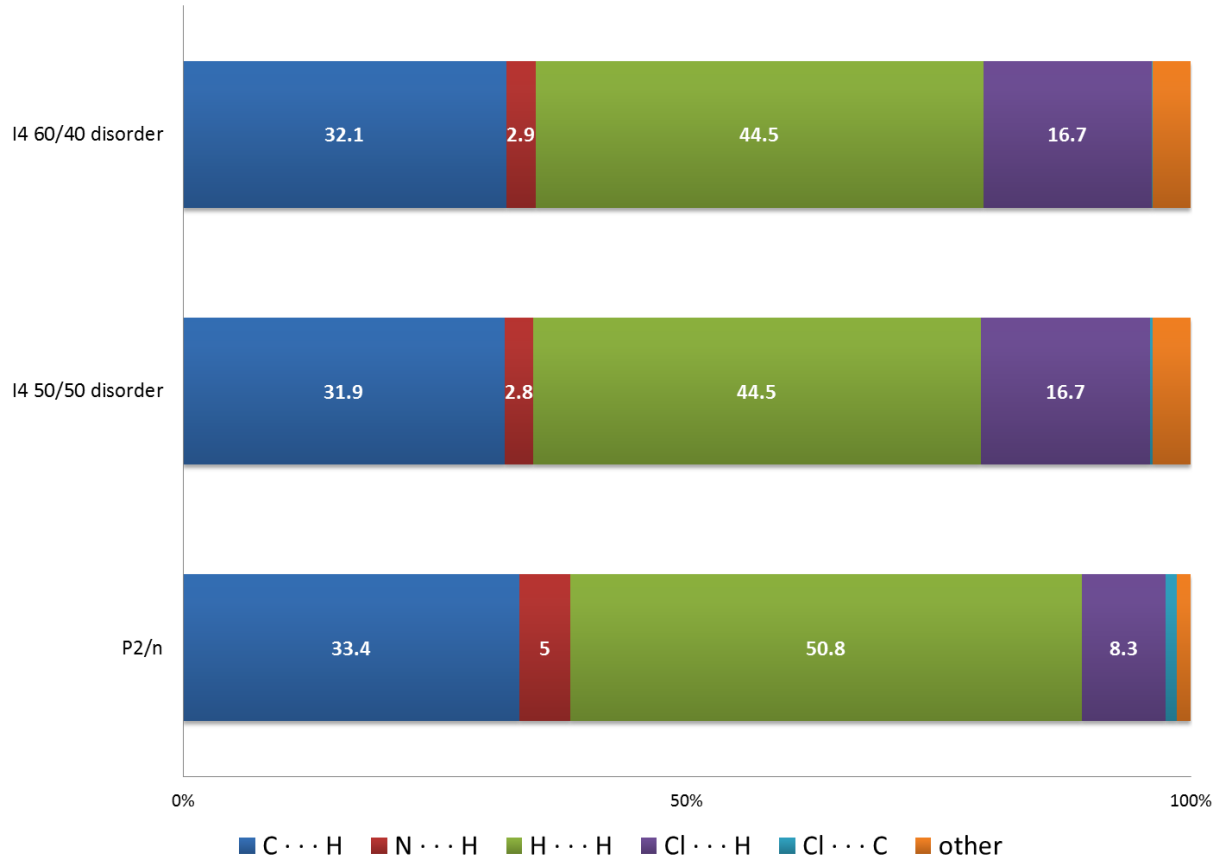

Figure 3.11. Percentage contributions to the Hirshfeld surface area for the various close intermolecular contacts in the three room-temperature crystal structures of [Fe(TPP)Cl] (**1**).

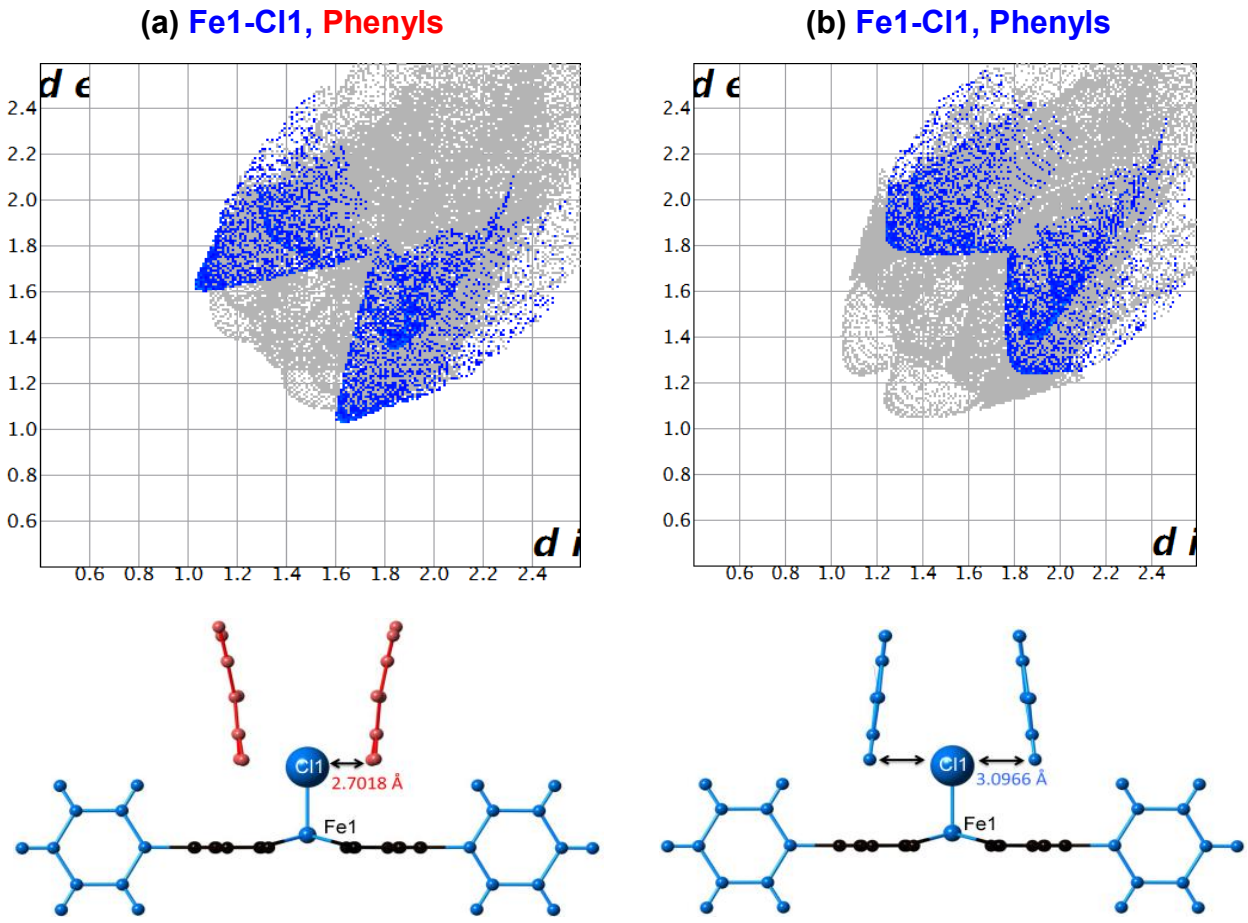

Figure 3.12. Hirshfeld fingerprints of Cl···H close contacts in the X-ray [Fe(TPP)Cl] (**1**) structure at 20 K in *I*4 with parts of Figure 3.4 reproduced, indicating that the configuration in (b) is preferred.[41]

3.3.3. Hirshfeld Surface Analysis of the Crystal Structure of [Co(TPP)(NO)] (6)

VT studies have been published on crystal structures of [Fe(TPP)(NO)] (**5**) and [Co(TPP)(NO)] (**6**),[11,13g,18] focusing on the structural disorder of the NO ligand at room temperature and gradual ordering of the NO ligand with cooling, resulting in a phase change with symmetry lowering from *I*4/*m* to *P*-1.[11,13g] Hirshfeld surface area and volume for [Co(TPP)(NO)] (**6**) change little and contract only 1.3% and 2.5%, respectively, with decreasing temperature, despite the phase change and the reduction in the disorder of the nitrosyl ligand (Table 3.4). Close to the phase transition at 195 K, significant intermolecular contacts between the nitrosyl oxygen and the hydrogen atoms on the phenyl rings of the adjacent molecules are noticeable (Figure 3.13a, red spots). After the phase transition (Figure 3.13b), a decrease in these close intermolecular contacts is immediate and obvious. In the tetragonal *I*4/*m* phase, the NO ligand is disordered in four positions above and four positions below the porphyrin plane, a total of eight-fold disorder. The disorder is taken into account for the Hirshfeld surface calculations according to McKinnon *et al.*[22] The nearest O···H contacts (~2.5 Å) in *P*-1 are further away than the close contacts (~2.3 Å) in *I*4/*m* (Figure 3.14). This decrease in intermolecular contacts can be explained by the tilting of the phenyl rings which in effect traps the disordered NO ligand. By 180 K, the disordered NO ligand is trapped into a single position above and below the porphyrin plane, which are related to each other by an inversion center. This phase change in [Co(TPP)(NO)] (**6**) is abrupt, immediately increasing both the Hirshfeld surface and void volume by more than 1%. The void-volume percentage in the cell increases from 15.42% at 195 K before to 16.47% at 190 K after the phase transition (Table 3.4, Figure 3.15).

Table 3.4. Comparison of the Hirshfeld surfaces and void volumes

Complex	Temperature (K)	Space group	Hirshfeld volume ($Å^3$)	Hirshfeld area ($Å^2$)	% of the void volume in the cell volume
[Fe(TPP)Cl] (**1**)	293 K	*I*4	888.55	677.40	17.21
-	143 K	*I*4	875.55	674.85	16.42
-	100 K[11]	*I*4/*m*	865.71	668.79	15.84
-	20 K	*I*4	868.02	674.29	10.19
[Co(TPP)(NO)][11] (**6**)	250	*I*4/*m*	854.01	663.56	15.27
-	195	*I*4/*m*	859.31	667.66	15.42
-	190	*P*-1	868.55	671.18	16.47
-	180	*P*-1	855.31	664.72	16.20
-	100	*P*-1	833.01	655.22	14.71
[Fe(TPP)(NO)][13g] (**5**)	293 K	*I*4/*m*	875.44	675.08	16.16
-	180 K	*P*-1	860.04	668.09	16.00
-	90 K	*P*-1	849.32	664.76	15.14
-	33 K	*P*-1	845.26	663.53	14.79

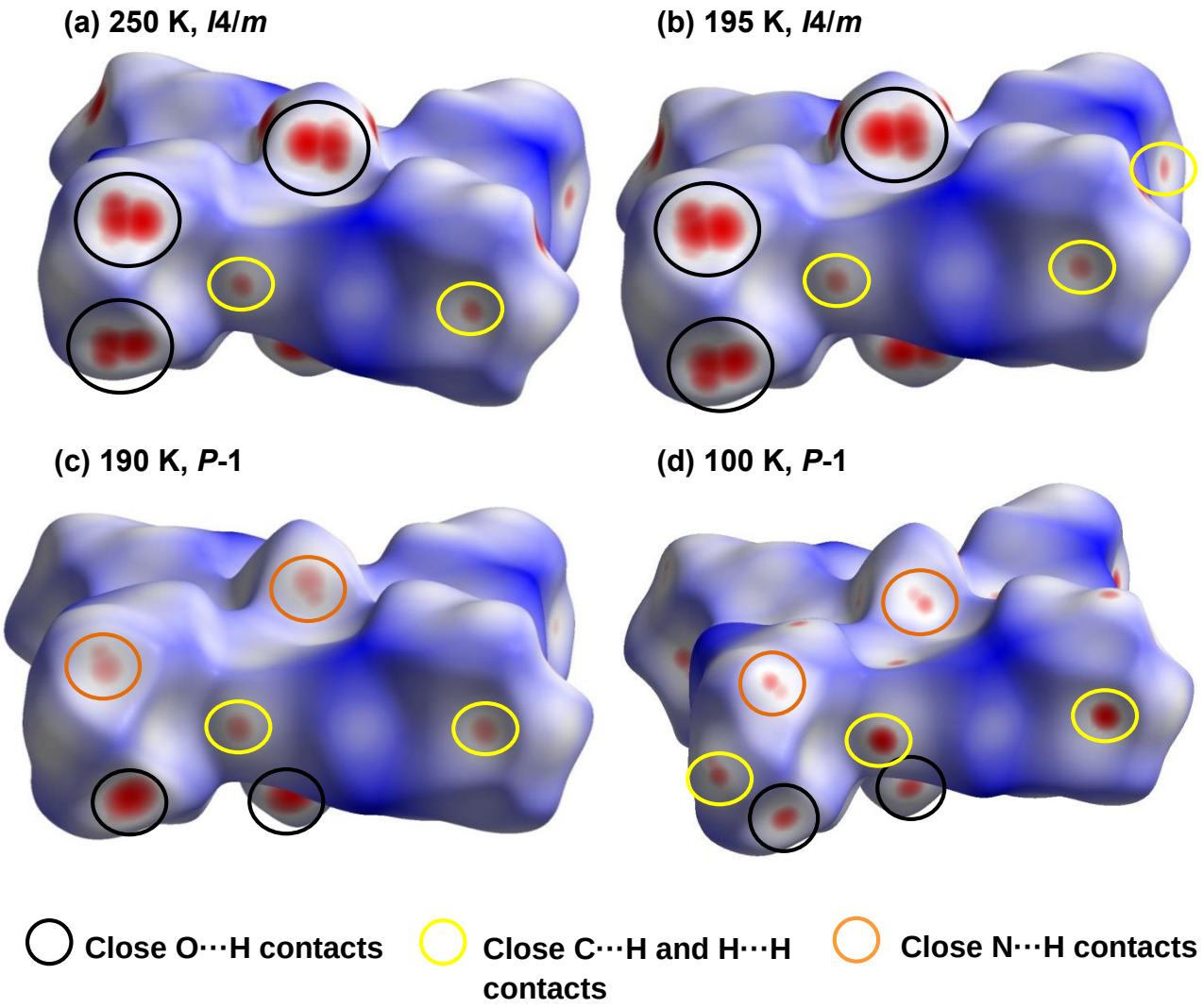

Figure 3.13. Hirshfeld surfaces for the crystal structures of [Co(TPP)(NO)] (**6**) at 250, 195, 190, and 100 K.

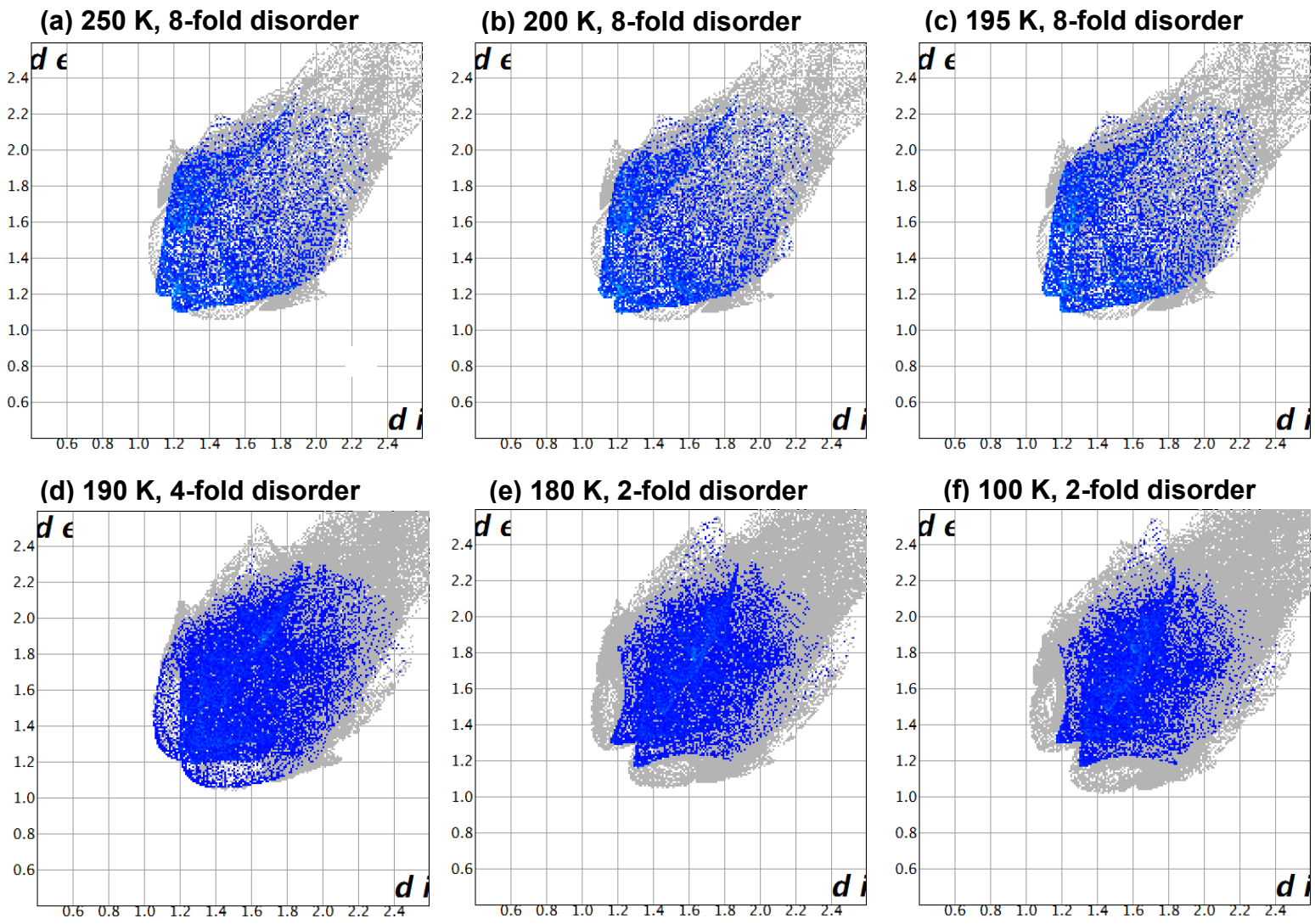

Figure 3.14. Hirshfeld fingerprint plots of [Co(TPP)(NO)] (**6**) (O···H close contacts).

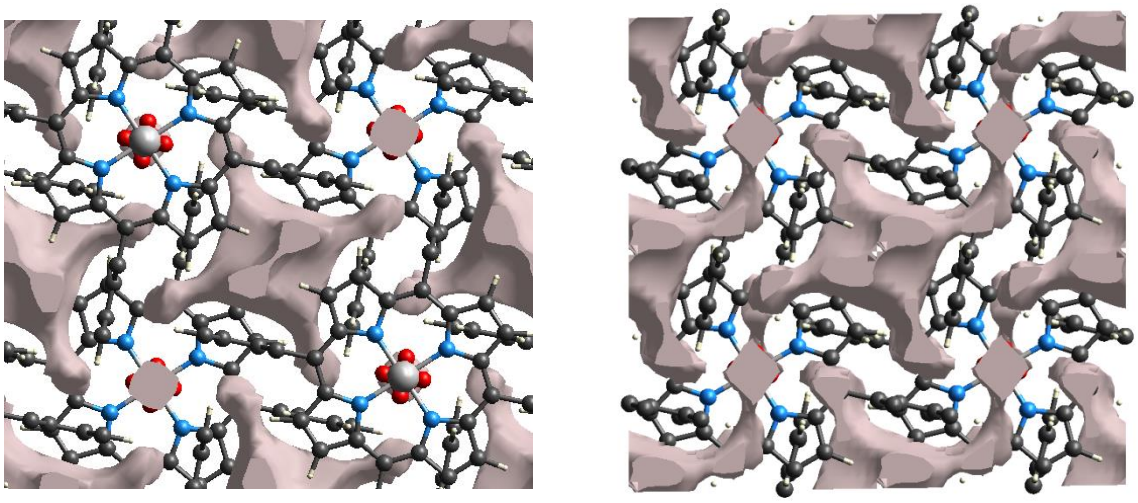

Figure 3.15. The voids of [Co(TPP)(NO)] (**6**) at 195 K (left, *I*4/*m*) and 190 K (right, *P*-1) using an isovalue of 0.002 e au^{-3}.

A contraction of the crystal lattice is expected with cooling. This is apparent in the relative contributions of the close intermolecular contacts to the Hirshfeld surface (Figure 3.16). The percent H···H and C···H close contacts gradually increase with decreasing temperature. Interestingly, after the phase change, the percent O···H close contacts are reduced while the N···H close contacts are increased significantly, signifying the ordering of the nitrosyl ligand with the phenyl tilt. The closest N···H contacts are 2.957 Å before the phase change and 2.696 Å after the phase change (Figure 3.17).

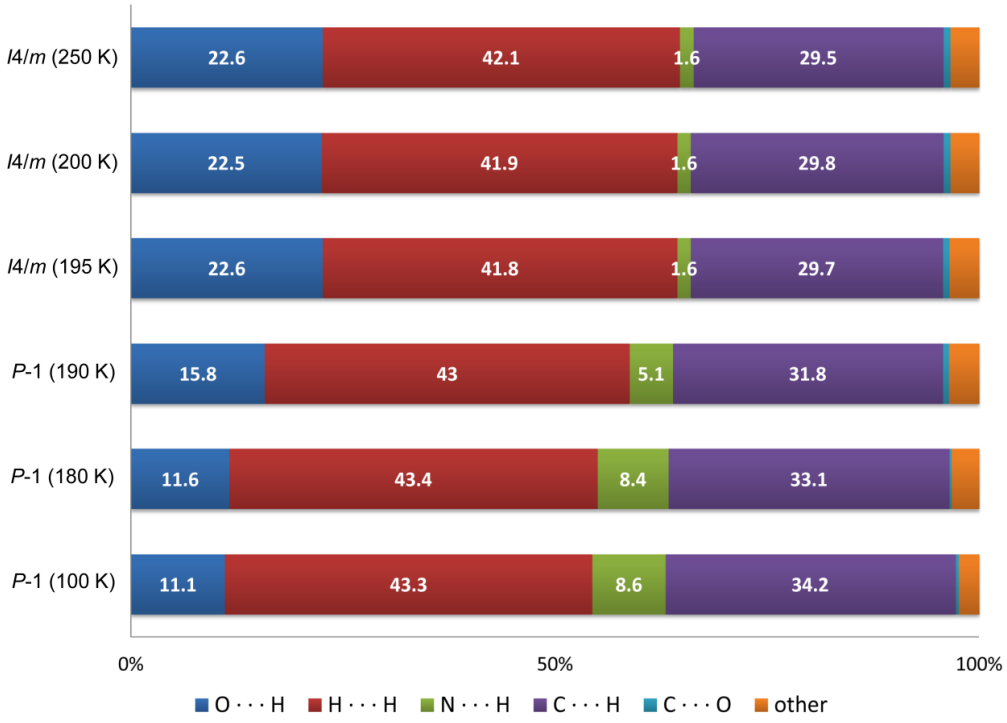

Figure 3.16. Percentage contributions to the Hirshfeld surface area for various intermolecular close contacts for [Co(TPP)(NO)] (**6**) molecules.

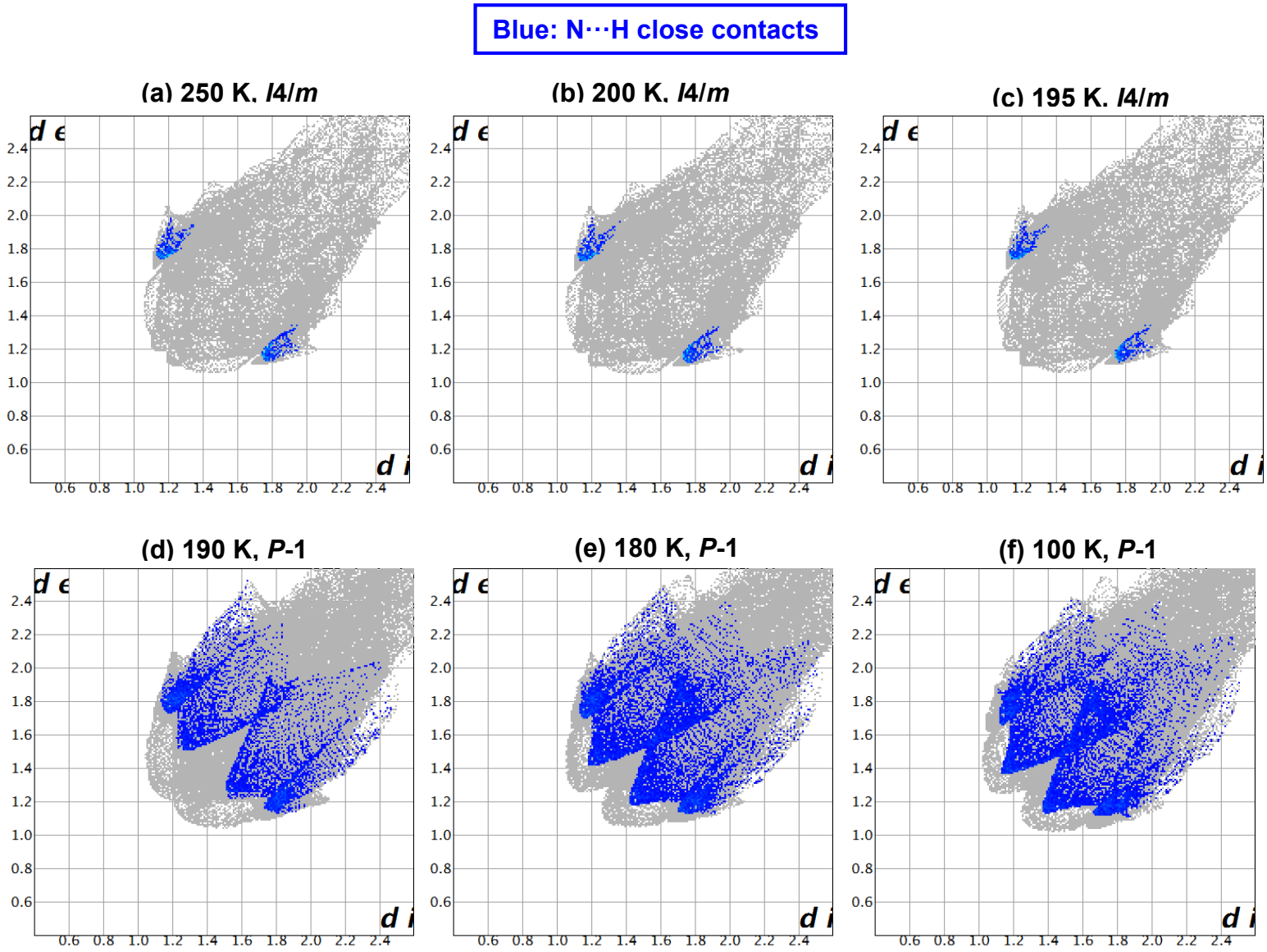

Figure 3.17. Hirshfeld fingerprint plots of [Co(TPP)(NO)] (**6**) (N···H close contacts).

3.3.4. Hirshfeld Surface Analysis of the Crystal Structure of [Fe(TPP)(NO)] (5)

Crystal structures of [Fe(TPP)(NO)][13g] (**5**) and [Co(TPP)(NO)][11] (**6**) are isomorphous. Unlike [Co(TPP)(NO)] (**6**) with a clear phase change at 190-195 K,[11] the change in [Fe(TPP)(NO)] (**5**) is gradual.[13g] Hirshfeld fingerprint plots showing the intermolecular close contacts are given in Figure 3.19. The Hirshfeld surface area and volume for [Fe(TPP)(NO)] (**5**) only slightly contract, by 1.7% and 3.4% respectively, with cooling. At 293 K, the 4-fold disorder of the NO ligand leads to very close contacts with four adjacent phenyls (red areas in Figure 3.18a). The tilted four phenyl groups surrounding the NO ligand below the phase change at 33 K are shown in Figure 3.20. The top is a view along the *c* axis with all four rings, and the left shows the phenyl rings A and B parallel to the nitrosyl ligand. The closest H atoms on the A and B phenyl rings are equal in distance (2.8130 and 2.8133 Å, respectively) to the O atom on the nitrosyl ligand. However, the N atom of the nitrosyl ligand is much closer to the H atom on B (2.5609 Å) than to the H atom on A (3.4074 Å). The structure on the right shows the phenyl rings C and D, perpendicular to the nitrosyl bond. The tilting of D towards the nitrosyl leads to a short distance (2.6411 Å) of its nearest H atom to the O atom and a fairly long distance (3.3095 Å) to the N atom. In C, the opposite is true, the nearest H atom is much closer to the N atom (2.6874 Å) than to the O atom (3.1594 Å).

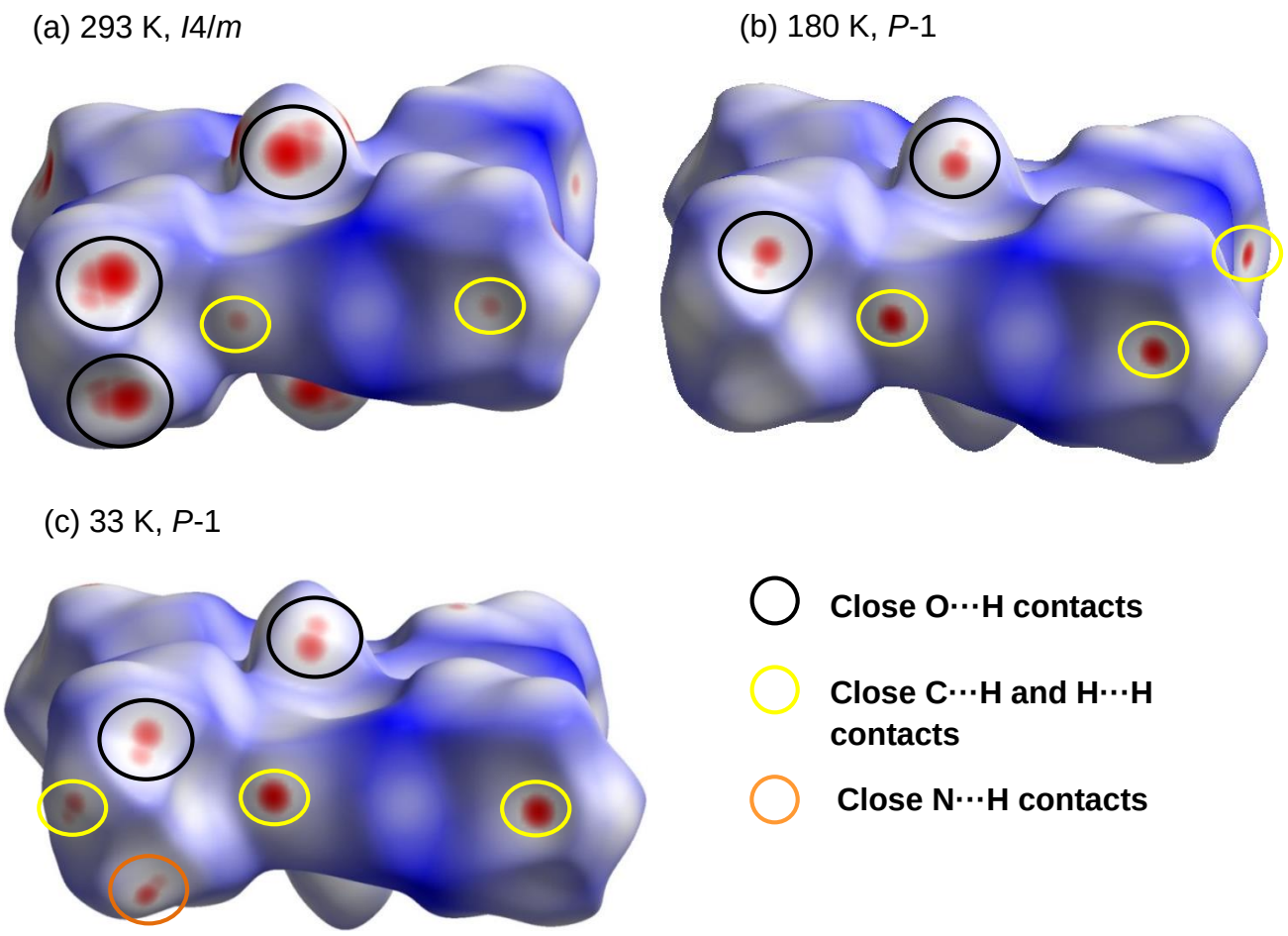

Figure 3.18. Hirshfeld surfaces of the crystals of [Fe(TPP)(NO)] (**5**) at 293, 180 and 33 K.

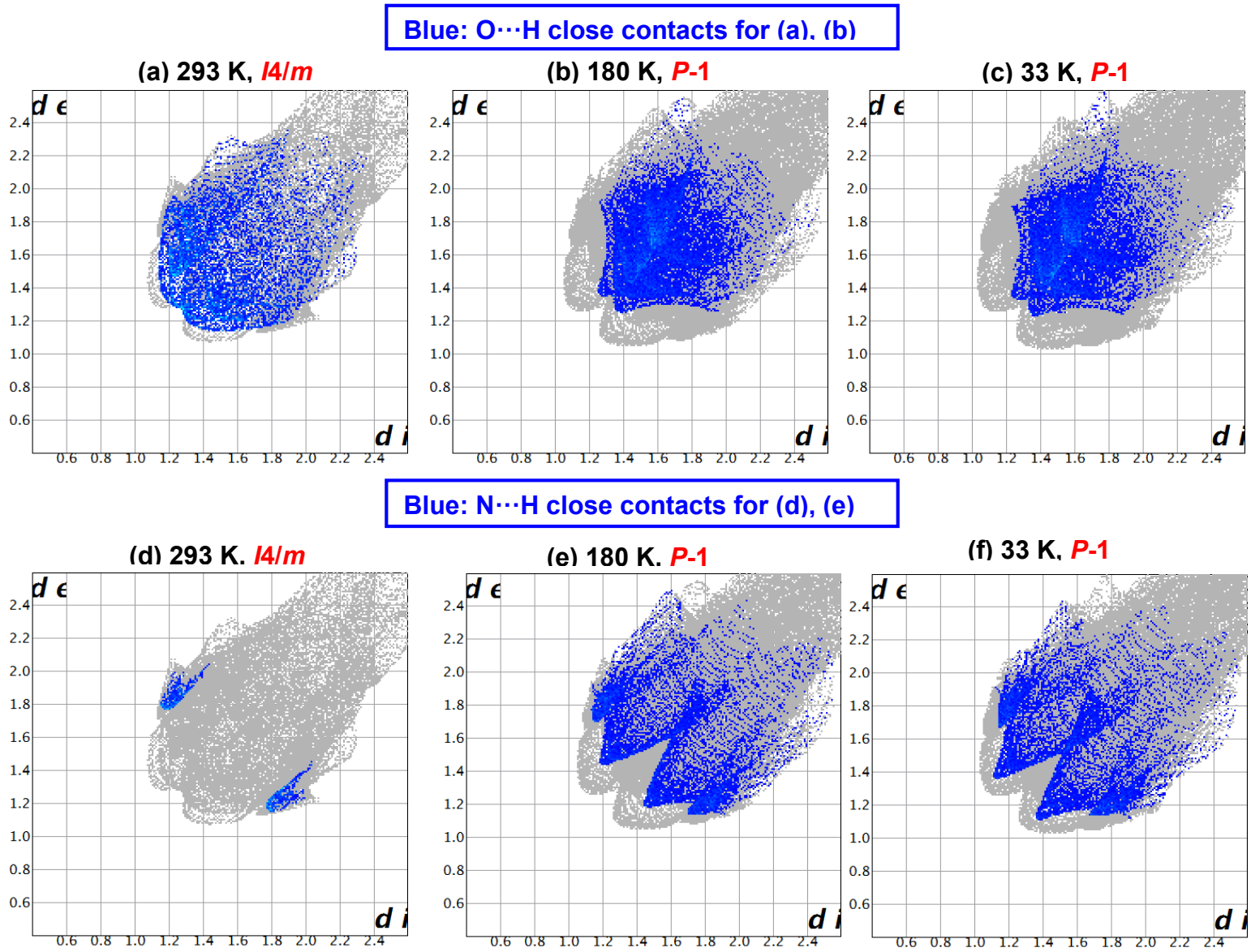

Figure 3.19. Hirshfeld fingerprint plots of [Fe(TPP)(NO)] (**5**) at 293 K, 180 K, and 33 K.

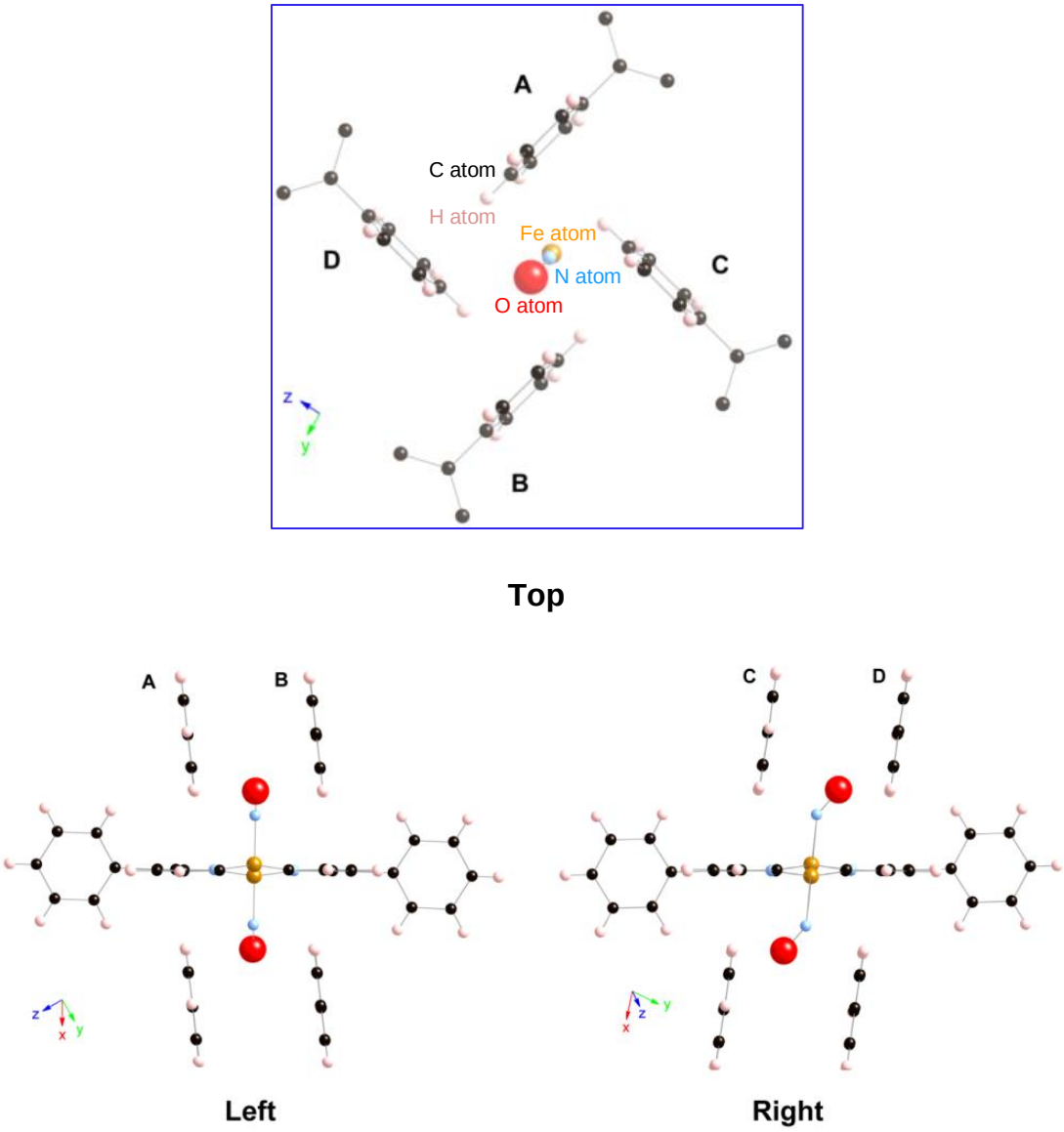

Figure 3.20. The phenyl-ring tilt in [Fe(TPP)(NO)] (**5**) at 33 K. (Top) Phenyl rings surrounding a NO ligand. (Left) Tilting of the phenyl rings A and B which are parallel to the nitrosyl bond. Phenyl rings C and D and other atoms are omitted for clarity. (Right) Tilting of the phenyl rings C and D which are perpendicular to the nitrosyl bond. Phenyl rings A and B and other atoms are omitted.

3.3.5. Comparison of the Hirshfeld Surface Analyses of [M(TPP)X] (M = Fe, X = Cl, 1; M = Co, 6; Fe, 5; X = NO) 7

[Co(TPP)(NO)] (**6**), the characteristic increase of the Hirshfeld volume or void-volume percentage after the phase change from *I*4/*m* to *P*-1 in [Fe(TPP)(NO)] (**5**) could not be observed. The Fe(III) ion is slightly larger than the Co(III) ion.[43] As a result, the Fe-ligand bonds in [Fe(TPP)(NO)] (**5**) are less ionic than those in [Co(TPP)(NO)] (**6**), perhaps leading to the structural softness in the former.

More importantly, the phase change in both nitrosyl complexes involves phenyl tilting as in [Fe(TPP)Cl] (**1**). Independent of the symmetric (Cl) or asymmetric (NO) apical ligand, the tilting is associated with cooling and plays a noticeable role in the ability of these metalloporphyrins to structurally compress. In the previous, traditional structural analyses (without considering the Hirshfeld surface analysis), the phenyl contribution to the phase change is overshadowed by the disorder in the asymmetric NO ligands.

3.4. Concluding Remarks

Metalloporphyrins have been studied intensely for decades. The basic structural analyses, typically focused on bond distances and angles, do not show significant changes in these parameters with cooling or phase changes. Such analyses, however, hardly reveal “available space” found in voids that become important to explain options for structural compression and phase changes. Furthermore, it has proved difficult to use the structural analyses when significant symmetry changes accompany phase changes. Hirshfeld analysis is employed in the current work to showcase how conformational changes appear in the molecular structures and to identify driving forces for such changes that are otherwise not obvious as a result of disorder or twinning.

Studies here illustrate the temperature-dependent structural characteristics to help understand the intricate interplay of structural and conformational flexibility of the metalloporphyrins, revealing that the disorders in the crystal structures of [Fe(TPP)(NO)] (**5**) and [Co(TPP)(NO)] (**6)** at room temperature and phase changes at lower temperatures are a result of intermolecular interactions in the solid state. The phase changes in [Fe(TPP)(NO)] (**5**) and [Co(TPP)(NO)] (**6**), accompanied by the phenyl tilting, lead to reduced intermolecular interactions by gradual movement of the phenyl groups into the open voids. The same occurs in [Fe(TPP)Cl] (**1**) with no phase change.

Hirshfeld surface analyses as a whole-of-molecule approach allow for an objective way to compare crystal structures of different crystal symmetries but with similar molecular forces and interactions. The phase change appears to be as much driven by phenyl tilting away from the *c* axis into the void space as by the ordering of the nitrosyl ligand. It is the void volume, not the increase in the individual molecular density, that accommodates further thermal compression with cooling. The analyses of the three compounds suggest that other metalloporphyrins with the general formula [M(TPP)X] in the tetragonal system may show analogous behavior of the phenyl rings contributing considerably to phase changes at low temperatures.

References

1. Behere, D. V.; Birdy, R.; Mitra, S. *Inorg. Chem.* **1982**, *21*, 386.
2. D'Angelo, P.; Lapi, A.; Migliorati, V.; Arcovito, A.; Benfatto, M.; Roscioni, O. M.; Meyer-Klaucke, W.; Della-Longa, S. *Inorg. Chem.* **2008**, *47*, 9905.
3. Scheidt, W. R.; Gouterman, M. in *Iron Porphyrins, Part One*, edited by A. B. P. Lever & H. B. Gray, Addison-Wesley, Reading, MA: 1983, pp. 89-139.
4. (a) Fleischer, E. B.; Miller, C. K.; Webb, L. E. *J. Am. Chem. Soc.* **1964**, *86*, 2342. (b) Hoard, J. L.; Cohen. G. H.; Glick, M. D. *J. Am. Chem. Soc.* **1967**, *89*, 1992.
5. Eaton, D. R.; LaLancette, E. A. *J. Chem. Phys.* **1964**, *41*, 3534.
6. Collman, J. P.; Hoard, J. L.; Kim, N.; Lang, G.; Reed, C. A. *J. Am. Chem. Soc.* **1975**, *97*, 2676.
7. Cheng, R. J.; Chen, P. Y.; Lovell, T.; Liu, T.; Noodleman, L.; Case, D. A. *J. Am. Chem. Soc.* **2003**, *125*, 6774.
8. Mao, J.; Zhang, Y.; Oldfield, E. *J. Am. Chem. Soc.* **2002**, *124*, 13911.
9. (a) Scheidt, W. R.; Finnegan, M. G. *Acta Cryst.* **1989**, *C45*, 1214. The CIF file was obtained from the Cambridge Crystallographic Data Centre using the DOI of the paper: doi:10.1107/S0108270189000715 (b) Finnegan, M. G.; Lappin, A. G.; Scheidt, W. R. *Inorg. Chem.* **1990**, *29*, 181.
10. Hunter, S. C.; Podlesnyak, A. A.; Xue, Z. L. *Inorg. Chem.* **2014**, *53*, 1955.
11. Grande, L. M.; Noll, B. C.; Oliver, A. G.; Scheidt, W. R. *Inorg. Chem.* **2010**, *49*, 6552.

12. Corban, G.J.; Hadjikakou, S. K.; Tsipis, A. C.; Kubicki, M.; Bakas, T.; Hadjiliadis, N. *New J. Chem.* **2011**, *35*, 213. The CIF file deposited in the Cambridge Crystallographic Data Centre (CCDC No. 783326) was used.

13. (a) Moncada, S.; Palmer, R. M.; Higgs, E. A. *Pharmacol. Rev.* **1991**, *43*, 109. (b) Ignarro, L.: *Nitric Oxide: Biology and Pathobiology*; Academic Press: San Diego, 2000. (c) Lehnert, N.; Berto, T. C.; Galinato, M. G. I.; Goodrich, L. E. *The Role of Heme-Nitrosyls in the Biosynthesis, Transport, Sensing, and Detoxification of Nitric Oxide (NO) in Biological Systems: Enzymes and Model Complexes*. In *The Handbook of Porphyrin Science*; Kadish, K. M., Smith, K. M., Guilard, R., Eds.; World Scientific: Hackensack, NJ, 2011; Vol. 14; Chap. 63, pp 1−247. (d) Goodrich, L. E.; Paulat, F.; Praneeth, V. K. K.; Lehnert, N. *Inorg. Chem.* **2010**, *49*, 6293. (e) Straub, A. C.; Lohman, A. W.; Billaud, M.; Johnstone, S. R.; Dwyer, S. T.; Lee, M. Y.; Bortz, P. S.; Best, A. K.; Columbus, L.; Gaston, B.; Isakson, B. E. *Nature*, **2012**, *491*, 473. (f) Gladwin, M. T.; Kim-Shapiro, D. B. *Nature*, **2012**, *491*, 344. (g) Silvernail, N. J.; Olmstead, M. M.; Noll, B. C.; Scheidt, W. R. *Inorg. Chem.* **2009**, *48*, 971. (h) Zheng, H. W.; Wang, R. B.; Qiao, L. K.; Du, Y. *Sci. China Technol. Sci*. **2014**, *57*, 857.

14. (a) Wang, H.; Zhong, F.; Pan, J.; Li, W.; Su, J.; Huang, Z.-X.; Tan, X., *J. Biolog. Inorg. Chem.* **2012**, *17*, 719. (b) Garthwaite, J. *Trends Neurosci.* **1991**, *14*, 60.

15. (a) Fritz, B. G.; Roberts, S. A.; Ahmed, A.; Breci, L.; Li, W.; Weichsel, A.; Brailey, J. L.; Wysocki, V. H.; Tama, F.; Montfort, W. R. *Biochemistry* **2013**, *52*, 156. (b) Rapoport, R. M.; Murad, F. *Circ. Res.* **1983**, *52*, 352. (c) Ignarro, L. J.; Adams, J. B.; Horwitz, P. M.; Wood, K. S. *J. Biol. Chem.* **1986**, *261*, 4997.

16. (a) Azuma, H.; Ishikawa, M.; Sekizaki, S. *Br. J. Pharmacol.* **1986**, *88*, 411. (b) Furlong, B.; Henderson, A. H.; Lewis, M. J.; Smith, J. A. *Br. J. Pharmacol.* **1987**, *90*, 687.

17. (a) Campbell, M. G.; Underbakke, E. S.; Potter, C. S.; Carragher, B.; Marletta, M. A. *Proc. Natl. Acad. Sci. USA* **2014**, *111*, 2960. (b) Ursu, O. N.; Sauter, M.; Ettischer, N.; Kandolf, R.; Klingel, K. *Cell. Physiol. Biochem.* **2014**, *33*, 52.

18. (a) Scheidt, W. R.; Frisse, M. E. *J. Am. Chem. Soc.* **1975**, *97*, 17. (b) Scheidt, W. R.; Hoard, J. L. *J. Am. Chem. Soc.* **1973**, *95*, 8281.

19. (a) Scheidt, W. R.; Barabanschikov, A.; Pavlik, J. W.; Silvernail, N. J.; Sage, J. T. *Inorg. Chem.* **2010**, *49*, 6240. (b) Kim, H.; Chang, Y. H.; Lee, S.-H.; Lim, S.; Noh, S.-K.; Kim, Y.-H.; Kahng, S.-J. *Chem. Sci.* **2014**, *5*, 2224. (c) Sulok, C. D.; Bauer, J. L.; Speelman, A. L.; Weber, B.; Lehnert, N. *Inorg. Chim. Acta* **2012**, *380*, 148. (d) Lehnert, N.; Galinato, M. G. I.; Paulat, F.; Richter-Addo, G. B.; Sturhahn, W.; Xu, N.; Zhao, J. Y. *Inorg. Chem.* **2010**, *49*, 4133.

20. Spackman, M. A.; Jayatilaka, D. *CrystEngComm* **2009**, *11*, 19.

21. Spackman, M. A.; McKinnon, J. J. *CrystEngComm* **2002**, *4*, 378.

22. McKinnon, J. J.; Jayatilaka, D.; Spackman, M. A. *Chem. Commun.* **2007**, 3814.

23. Turner, M. J.; McKinnon, J. J.; Jayatilaka, D.; Spackman, M. A. *CrystEngComm* **2011**, *13*, 1804.

24. Dougan, B. A. Ph. D. Dissertation, The University of Tennessee, Knoxville, 2009.

25. Poulsen, R.; Bentien, A.; Graber, T.; Iverson, B. *Acta Crystallogr. Sect. A* **2004**, *A60,* 382.

26. Bruker (2003). SAINT-PLUS, Version 6.02 (including XPREP). Bruker AXS Inc., Madison, Wisconsin, USA.
27. Bruker (2007). APEX2. Version 2.14. Bruker AXS Inc., Madison, Wisconsin, USA.
28. Sheldrick, G. M. (2003). SADABS. University of Göttingen, Germany.
29. Lehmann, M. S.; Kuhs, W.; Allibon, J.; Wilkinson, C.; McIntyre, G. J. *J. Appl. Cryst.* **1989**, *22*, 562.
30. Wilkinson, C.; Khamis, H. W.; Stansfield, R. F. D.; McIntyre, G. J. *J. Appl. Cryst.* **1988**, *21*, 471.
31. Coppens, P.; Leiserowitz, L.; Rabinovich, D. *Acta Cryst.* **1965**, *18*, 1035.
32. Howard, J. A. K.; Johnson, O.; Schultz, A. J.; Stringer, A. M. *J. Appl. Cryst.* **1987**, *20*, 120.
33. Sheldrick, G. M. *Acta Cryst.* **2008**, *A64*, 112.
34. Spek, A. L. *J. Appl. Cryst.* **2003**, *36*, 7.
35. Wolff, S. K.; Grimwood, D. J.; McKinnon, J. J.; Turner, M. J.; Jayatilaka, D.; Spackman, M. A. CrystalExplorer (Version 3.1), University of Western Australia, 2012.
36. (a) Sakurai, T.; Yamamoto, K.; Naito, H.; Nakamoto, N. *Bull. Chem. Soc. Jpn.* **1976**, *49*, 3042. (b) Coutsolelos, A.; Guilard, R.; Bayeul, D.; Lecomte, C. *Polyhedron* **1986**, *5*, 1157. (c) Cheng, B.; Scheidt, W. R. *Acta Cryst.* **1996**, *C52*, 361.
37. Skelton, B. W.; White, A. H. *Aust. J. Chem.* **1971**, *30*, 2655.
38. Hatano, K.; Scheidt, W. R. *Inorg. Chem.* **1979**, *18*, 877.
39. Anzai, K.; Hatano, K.; Lee, Y. J.; Scheidt, W. R. *Inorg. Chem.* **1981**, *20*, 2337.

40. Sakurai, T.; Yamamoto, K. *Sci. Paper. Inst. Phys. Chem. Res.* **1976**, *70*, 31.

41. Two CIF files were generated with the following ratios of Fe-Cl part/phenyls: 0.4084 /0.5916 (Figure 3.12a), 0.4084/0.4084 (Figure 3.12b). These CIF files were used to generate the fingerprints in Figures 3.12a-b.

42. Rowland, R. S.; Taylor, R. *J. Phys. Chem.* **1996**, *100*, 7384.

43. Shannon, R. D. *Acta Crystallogr.* **1976**, *A32*, 751.

Part 4

Syntheses and Characterization of Tantalum Alkyl Amide Imide Complexes and Their Reactions with O_2

Abstract

The alkyl amide imide complexes $TaMe_2(=NSiMe_3)[N(SiMe_3)_2]$ (**9**) and $Ta(CH_2Ph)_2(=NSiMe_3)[N(SiMe_3)_2]$ (**10**) have been prepared from the reactions of $\{Ta(\mu\text{-}Cl)Cl(=NSiMe_3)[N(SiMe_3)_2]\}_2$ (**8**) with the appropriate organometallic reagents. **10** has been characterized by single-crystal X-ray diffraction and shows η^2 coordination of the phenyl ring on one of the benzyl ligands to the Ta center. The reaction of **9** and 0.5 equiv of O_2 leads to selective oxygen insertion into one Ta-Me bond, yielding an alkoxy bridged dimer $Ta_2(\mu\text{-}OMe)_2(=NSiMe_3)_2[N(SiMe_3)_2]_2Me_2$ as *cis*- and *trans*-isomers (***cis*-11** and ***trans*-11**). The ***trans*-11** isomer has been characterized by single-crystal X-ray diffraction. A mixture of ***cis*-11** and ***trans*-11** in benzene-d_6 was found to react with additional O_2 to give $\{Ta(\mu\text{-}OMe)(OMe)(=NSiMe_3)[N(SiMe_3)_2]\}_2$.

4.1. Introduction

Chemistry of transition-metal imide complexes is an active area of research due to their potential use as catalysts and as precursors in the preparation of microelectronic materials.[1-3] For example, an imide ligand is used in the Schrock's metathesis catalyst.[1b,2a] Imide ligands have been prepared by a variety of methods, the vast majority being intermolecular imidation[1,4-5] with primary amines, imines, nitriles, and other nitrogen-containing compounds.[1,4] The rarer intramolecular imidation is generally formed through 1,2-elimination of Me_3SiCl or interligand transfer.[4,5] Thermolysis of $TaCl_3[N(SiMe_3)_2]_2$ (**7**), for example, gives Me_3SiCl and $\{Ta(\mu\text{-}Cl)Cl(=NSiMe_3)[N(SiMe_3)_2]\}_2$ (**8**).[4h] Reaction of $CrO_2[N(SiMe_3)_2]_2$ with excess pyridine leads to the $SiMe_3$ migration to an oxo ligand, forming $[CrO(NSiMe_3)Py]_2(\mu\text{-}OSiMe_3)_2$.[4c]

Tantalum imide complexes have been used as precursors for Ta_2O_5[3,6] and TaN[7] thin films in chemical vapor deposition (CVD) and atomic layer deposition (ALD) processes. SiO_2 has typically been the gate insulator due to its ease of preparation. However, SiO_2 is a poor insulator due to its low dielectric constant (k = 3.9) and suffers from gate current leakage when the thickness of the gate insulator film is below 2 nm.[8-15] New high-k metal oxides such as HfO_2 and Ta_2O_5 have been replacing SiO_2 in existing microelectronics.[15] To make these metal oxide thin films, d^0 metal precursors, such as $Bu^tN{=}Ta(NEt_2)_3$, react with O_2 or H_2O in CVD or ALD processes (Scheme 4.1).[16-20] The nature of CVD/ALD processes makes it difficult to determine the mechanistic pathways of these reactions.

The reactions between transition metals and O_2 play an important role in biological systems, catalytic processes, and the synthesis of fine chemicals.[21-23] For late

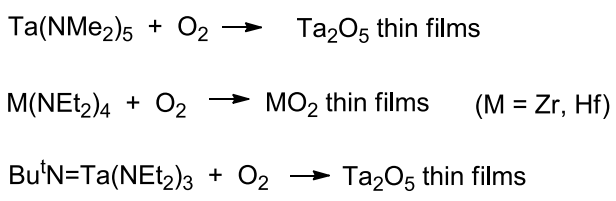

Scheme 4.1. CVD and ALD processes to metal-oxide thin films.[16-20]

transition metal complexes, the oxidation of the metals is an important step.[24] Unlike the reactions between late transition metal complexes and O_2, very little is known about the reactions of d^0 transition metal complexes with O_2, due in part to the difficulty in studying these reactions. Most d^0 metal complexes are air sensitive, requiring work under inert gases.[25] There has also been a lack of potential applications of such reactions. Oxygen insertion into metal-carbon bonds has been reported by Schwartz et al. in the reactions of O_2 with $Cp_2Zr(R)Cl$ (R = alkyl) and by Wolczanski et al. in the reactions between O_2 and $(RO)_2TiMe_2$ (Scheme 4.2).[25c,d] The formation of the siloxide $Cp_2Zr(OSiMe_3)Cl$ was reported by Tilley in the reaction of O_2 with $Cp_2Zr(SiMe_3)Cl$ (Scheme 4.2).[25b]

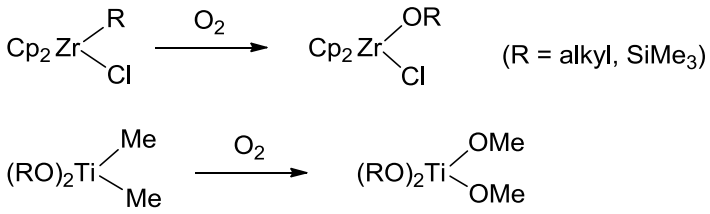

Scheme 4.2. Previous examples of reactions between d^0 metal complexes and O_2.[25b-d]

Our group has studied the reaction between the alkyl amide imide complex $Ta(CH_2Bu^t)_2(=NSiMe_3)[N(SiMe_3)_2]$ and O_2.[25w] Selective oxygen insertion into the two Ta-alkyl bonds was observed, yielding an alkoxide complex $Ta(=NSiMe_3)[N(SiMe_3)_2](OCH_2Bu^t)_2$ (Scheme 4.3). $Ta(=NSiMe_3)[N(SiMe_3)_2](OCH_2Bu^t)_2$ undergoes a ligand exchange to give $Ta_2(\mu\text{-}NSiMe_3)_2(OCH_2Bu^t)_6$ and $Ta(=NSiMe_3)[N(SiMe_3)_2]_2(OCH_2Bu^t)$ (Scheme 4.3).

We have prepared $TaMe_2(=NSiMe_3)[N(SiMe_3)_2]$ (**9**) and $Ta(CH_2Ph)_2(=NSiMe_3)[N(SiMe_3)_2]$ (**10**) from $\{Ta(\mu\text{-}Cl)Cl(=NSiMe_3)[N(SiMe_3)_2]\}_2$ (**8**) and the appropriate organometallic reagents. The reaction between 0.5 equiv of O_2 and **9** results in oxygen insertion into a Ta-Me bond forming the methoxy bridged dimer $Ta_2(\mu\text{-}OMe)_2(=NSiMe_3)_2[N(SiMe_3)_2]_2Me_2$ (***cis*-11** and ***trans*-11**). ***Cis*-11** and ***trans*-11** react with additional O_2 to give $\{Ta(\mu\text{-}OMe)(OMe)(=NSiMe_3)[N(SiMe_3)_2]\}_2$. Our studies are reported here.

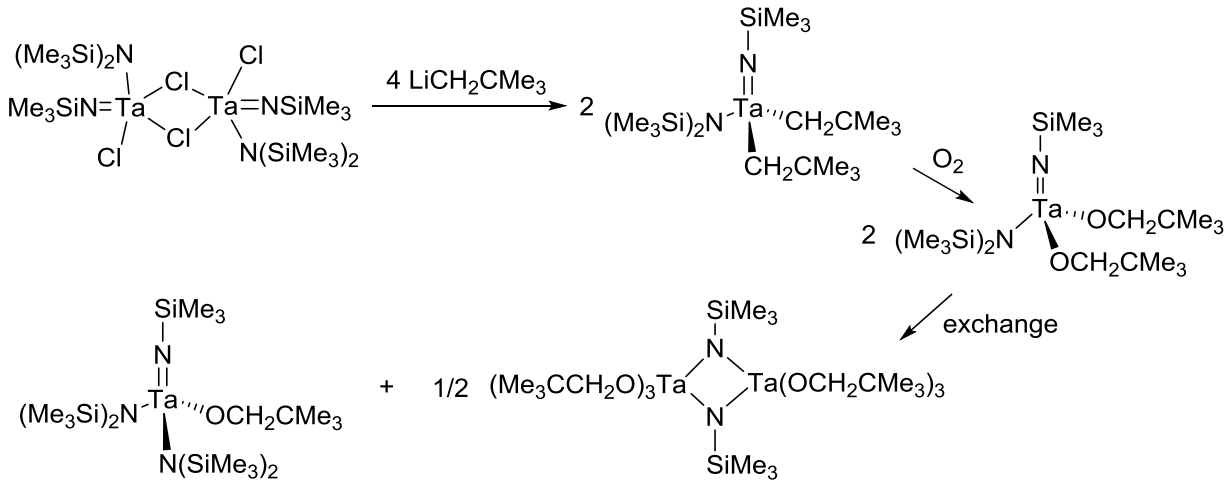

Scheme 4.3. Synthesis of $Ta(CH_2Bu^t)_2(=NSiMe_3)[N(SiMe_3)_2]$ and its reaction with O_2.[25w]

4.2. Experimental Section

All manipulations were performed under a dry nitrogen atmosphere with the use of either a drybox or standard Schlenk techniques. All solvents such as diethyl ether, THF, hexanes, toluene, and pentane were dried over potassium/benzophenone, distilled, and stored under nitrogen. $TaCl_5$ (Strem), $LiN(SiMe_3)_2$ (Aldrich), and MeLi (1.6 M in Et_2O, Acros) were used as received. $\{Ta(\mu\text{-}Cl)Cl(=NSiMe_3)[N(SiMe_3)_2]\}_2$ (**8**) and $ClMgCH_2Ph$ (1.02 M in Et_2O) were prepared by the literature methods.[4h,26,27] NMR spectra were recorded on a Varian VNMRS 500 MHz, Mercury-VX 300 MHz, Bruker Avance 400 MHz, or AC 250 MHz FT spectrometer and were referenced to solvents. Elemental analyses were conducted via Complete Analysis Laboratories, Inc., Parsippany, NJ.

4.2.1. Synthesis of $TaMe_2(=NSiMe_3)[N(SiMe_3)_2]$ (9)

MeLi (1.36 mL, 1.39 mmol) in Et_2O was added dropwise to a stirred solution of **8** (542 mg, 0.543 mmol) in Et_2O (30 mL) with stirring at -50 °C. The solution was stirred for 18 h as the temperature gradually warmed to 23 °C. The solvent was then removed in vacuo and pentane was added. The solution was then filtered and solvent removed in vacuo to give **9** (414 mg, 0.903 mmol, 83.1% yield) as a crude brown liquid. Distillation of the crude liquid at 85.5 °C under 0.01 torr vacuum gave a yellow liquid of **9** (101 mg, 0.220 mmol, 20.3% yield) condensed on a cold finger at -15 °C. ^{1}H NMR (benzene-d_6, 250 MHz, 23 °C) δ 0.57 (s, 6H, *Me*), 0.37 (s, 9H, =NSi*Me*$_3$), 0.32 [s, 18H, N(Si*Me*$_3$)$_2$]. ^{13}C NMR (benzene-d_6, 75.0 MHz, 23 °C) δ 52.94 (*Me*), 4.41 [N(Si*Me*$_3$)$_2$], 2.70 (=NSi*Me*$_3$). MS for [**9**+H^+]: Calculated *m*/*z* = 459.15097. Found 459.14993.

4.2.2. Synthesis of $Ta(CH_2Ph)_2(=NSiMe_3)[N(SiMe_3)_2]$ (10)

$ClMgCH_2Ph$ (2.01 mL, 2.05 mmol) in Et_2O was added dropwise to a stirring solution of **8** (512 mg, 0.51 mmol) in Et_2O (30 mL) at -30 °C. The solution was stirred for 18 h, as the temperature gradually warmed to 23 °C, and then filtered. The volatiles were then removed in vacuo, giving **10** (0.520 mg, 0.85 mmol, 83% yield) as a brown solid. Crystals were obtained from a saturated solution of **10** in pentane at -30 °C. ^{1}H NMR (benzene-d_6, 499.7 MHz, 23 °C) δ 2.34 (d, 2H, CH_aH$_b$Ph), 2.01 (d, 2H, CH$_a$$H_b$Ph), 0.30 (s, 9H, =NSi$Me_3$), 0.23 [s, 18H, N(Si$Me_3$)$_2$]. ^{13}C NMR (benzene-$d_6$, 62.5 MHz, 23 °C) δ 138.87–125.16 (CH_2*Ph*), 64.92 (*C*H$_2$Ph), 4.50 [N(SiMe_3)$_2$], 2.97 (=NSiMe_3). Anal. Calcd for $C_{23}H_{41}N_2Si_3Ta$: C, 45.23; H, 6.77. Found: C, 45.07; H, 6.79.

4.2.3. Synthesis of $Ta_2(\mu\text{-}OMe)_2(=NSiMe_3)_2[N(SiMe_3)_2]_2Me_2$ (*cis*-11 and *trans*-11)

9 (242 mg, 0.528 mmol) in pentane (20 mL) in a Schlenk flask was frozen in a liquid nitrogen bath, and the volatiles inside the Schlenk flask were removed in vacuo. Half equiv of O_2 (0.264 mmol) was introduced through a gas manifold. The flask was gradually warmed to room temperature, and the solution was stirred for 6 h. The volatiles were removed in vacuo giving a crude mixture of ***cis*-11** and ***trans*-11**. The crude product was dissolved in pentane at 23 °C. Within a few minutes, white crystals of ***trans*-11** began to appear. Cooling the mixture at -30 °C yielded more crystals of ***trans*-11** (147 mg, 0.150 mmol, 58.8% yield). ^{1}H NMR (benzene-d_6, 300.0 MHz, 23 °C) ***cis*-11**: δ 3.86 (s, 6H, μ-O*Me*), 0.65 (s, 6H, *Me*), 0.40 [s, 36H, N(SiMe_3)$_2$], 0.33 (s, 18H, =NSiMe_3). ***trans*-11**: δ 3.78 (s, 6H, μ-O*Me*), 0.62 (s, 6H, *Me*), 0.42 [s, 36H, N(SiMe_3)$_2$], 0.31 (s, 18H, =NSiMe_3). ^{13}C NMR (benzene-d_6, 75.0 MHz, 23 °C) ***cis*-11**: δ ~64.16 (broad, μ-O*Me*), 41.61 (*Me*),

4.39 [overlapping peak, N(Si*Me*$_3$)$_2$], 3.47 (=NSi*Me*$_3$). ***trans*-11**: δ 63.09 (μ-O*Me*), 42.20 (*Me*), 4.39 [overlapping peak, N(Si*Me*$_3$)$_2$], 3.55 (=NSi*Me*$_3$). The ^{13}C NMR assignments were made with help of HSQC. Anal. Calcd for C22H66N4O2Si6Ta2 (crystals of ***trans*-11**): C, 27.84; H, 7.01; N, 5.90. Found: C, 27.69; H, 6.83; N, 5.71.

4.2.4. Determination of the Crystal Structures of 10 and *trans*-11

X-ray diffraction data at 173 K were collected on a Bruker AXS Smart 1000 diffractometer equipped with a CCD area detector and a graphite-monochromated Mo source and fitted with an upgraded Nicolet LT-2 low-temperature device (SMART APEX II systems; Precision Cryogenic Systems Inc.). Suitable crystals were coated with Paratone-N^{TM} oil (Exxon Chemical) and mounted on a cryo-loop and measured under an open-flow nitrogen cryo-stream at 143(2) K. Global refinements for the unit cell and data reduction were performed with the SAINT program.[28] Empirical absorption correction was performed with SADABS.[29] The space group for structure solution and refinement was determined from systematic absences using XPREP.[28]

4.3. Results and Discussion

4.3.1. Synthesis of TaMe$_2$(=NSiMe$_3$)[N(SiMe$_3$)$_2$] (9)

Reaction of 4 equiv of MeLi with {Ta(μ-Cl)Cl(=NSiMe$_3$)[N(SiMe$_3$)$_2$]}$_2$ (**8**) gave TaMe$_2$(=NSiMe$_3$)[N(SiMe$_3$)$_2$] (**9**) as a yellow liquid (Scheme 4.4). **9** was characterized by ^{1}H and ^{13}C NMR and MS spectroscopies. The identity of **9** was further confirmed through the characterization of Ta$_2$(μ-OMe)$_2$(=NSiMe$_3$)$_2$[N(SiMe$_3$)$_2$]$_2$Me$_2$ (***cis*-11** and ***trans*-11**), the product of the reaction between **9** and 0.5 equiv of O$_2$.

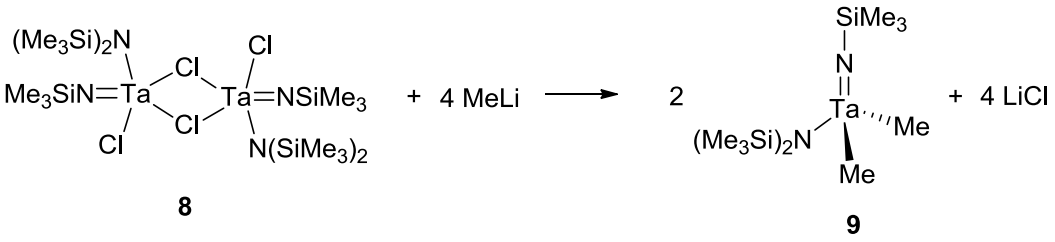

8 **9**

Scheme 4.4. Preparation of **9**.

The ^{1}H NMR spectrum of $TaMe_2(=NSiMe_3)[N(SiMe_3)_2]$ (**9**) in benzene-d_6 (Figure 4.1) showed a singlet for the methyl ligand at 0.57 ppm. The imide =NSi*Me*$_3$ and amide N(Si*Me*$_3$)$_2$ ligands were observed as singlets at 0.37 and 0.32 ppm, respectively. In the ^{13}C NMR spectrum of **9** in benzene-d_6 (Figure 4.2), the Ta-*Me* peak was at 52.94 ppm. The amide N(Si*Me*$_3$)$_2$ and imide =NSi*Me*$_3$ ligands were observed at 4.41 and 2.70 ppm, respectively. These NMR features and the observation of [**9**+H$^+$] in the MS spectrum (Figure 4.3) are consistent with a monomeric structure of **9**.

9 is reactive to trace O_2 in the inert gas, forming the methoxy methyl complex $Ta_2(\mu\text{-}OMe)_2(=NSiMe_3)_2[N(SiMe_3)_2]_2Me_2$ (***cis*-11** and ***trans*-11**) in pentane or hexanes solutions. ***trans*-11** has low solubility, forming white crystals from the solutions.

4.3.2. Synthesis of $Ta(CH_2Ph)_2(=NSiMe_3)[N(SiMe_3)_2]$ (10)

Reaction of $[Ta(\mu\text{-}Cl)Cl(=NSiMe_3)[N(SiMe_3)_2]]_2$ (**8**) with the Grignard reagent $ClMgCH_2Ph$ yielded **10** as a brown solid. Brown crystals of **10** were obtained from concentrated hexanes or pentane solution at -33 °C.

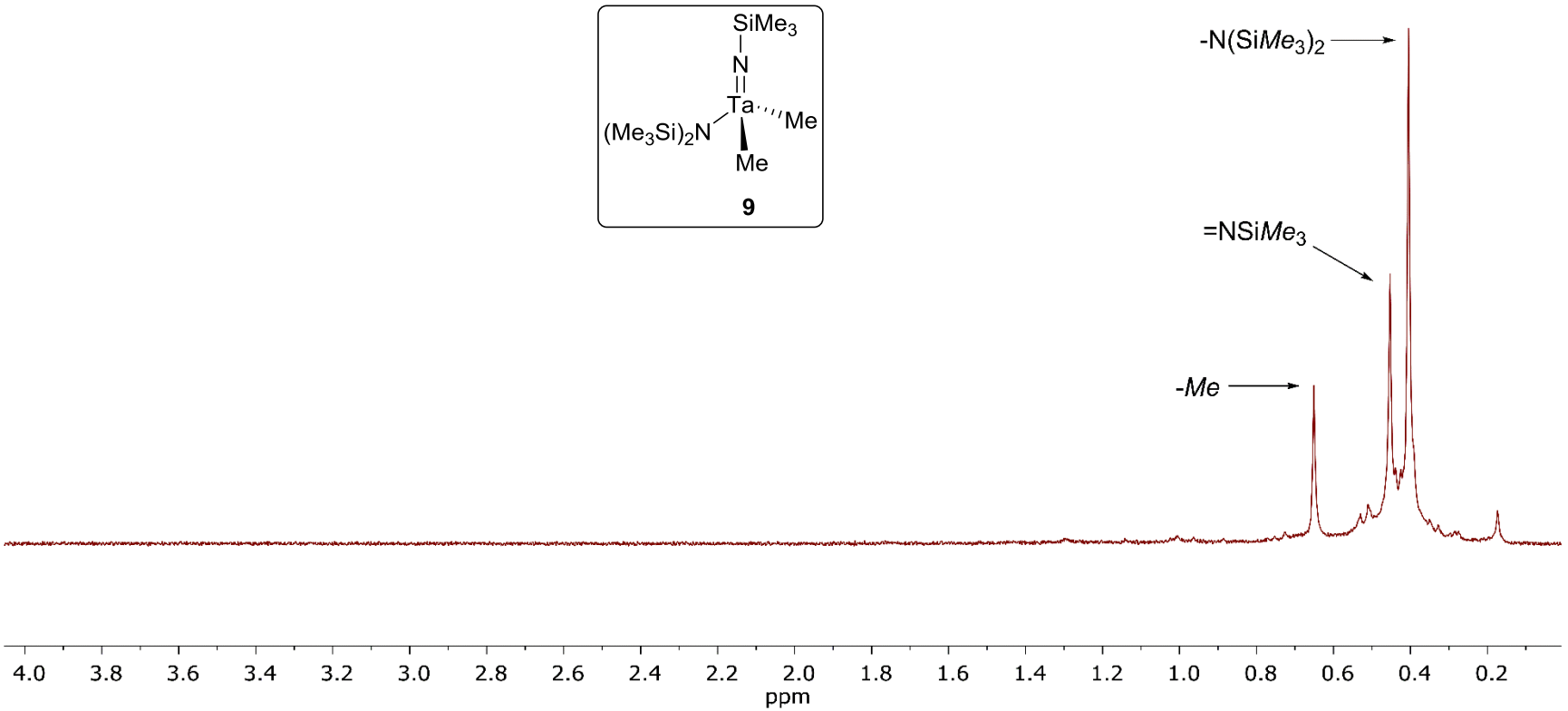

Figure 4.1. ^{1}H NMR spectrum of **9** in benzene-d_6 at 23 °C.

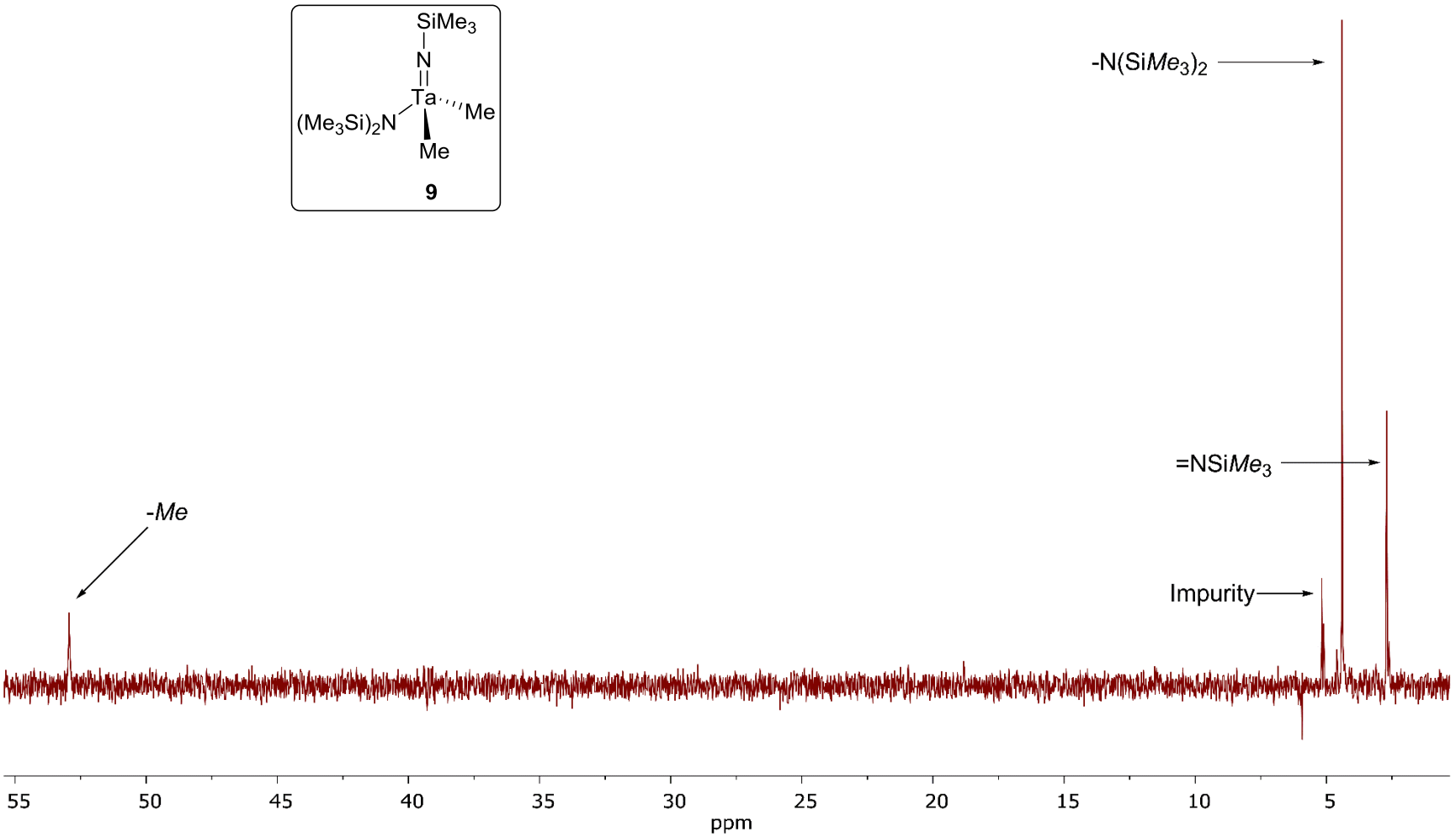

Figure 4.2. ^{13}C NMR spectrum of **9** in benzene-d_6 at 23 °C.

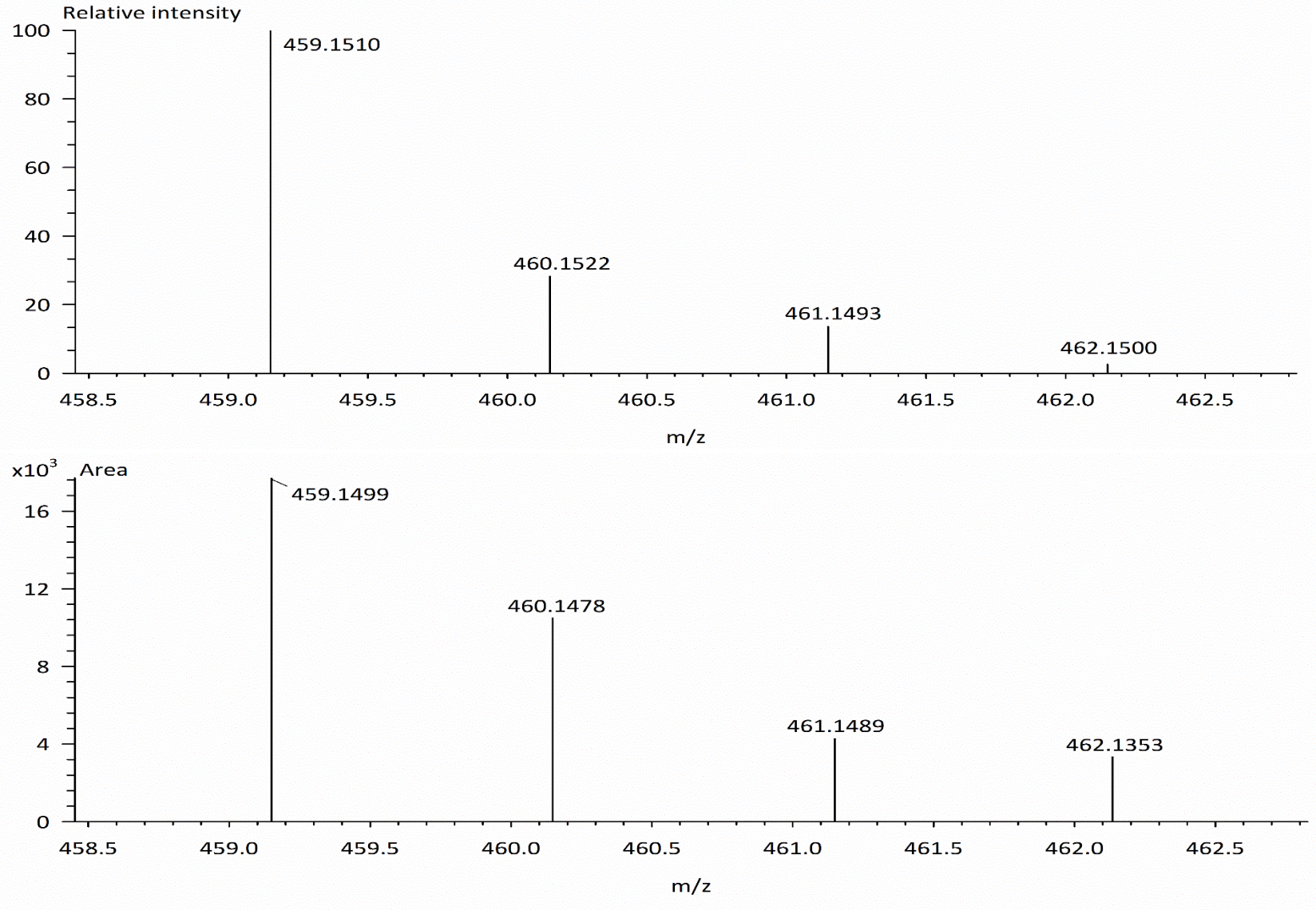

Figure 4.3. (Top) Calculated and (Bottom) Observed MS for [**9**+H^+].

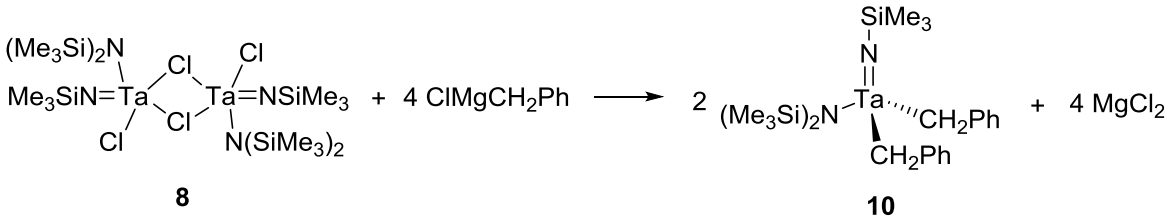

Scheme 4.5. Preparation of **10**.

The -C*H*$_2$- hydrogen atoms in the benzyl ligands in Ta(CH$_2$Ph)$_2$(=NSiMe$_3$)[N(SiMe$_3$)$_2$] (**10**) form a diastereotopic pair (Figure 4.4), as observed in the ^{1}H NMR spectrum of **10** (Figure 4.5). Singlets at 0.23 and 0.30 ppm were observed for the N(Si*Me*$_3$)$_2$ and =NSi*Me*$_3$ ligands, respectively.

The ^{13}C NMR spectrum of **10** in benzene-*d*$_6$ at 23 °C (Figure 4.6) has a peak at 64.92 ppm corresponding to the –*C*H$_2$-atoms of the *C*H$_2$Ph ligands. The phenyl carbon atoms of CH$_2$*Ph* are observed at 138.87–125.16 ppm. The peak for the silyl amide N(Si*Me*$_3$)$_2$ was observed at 4.50 ppm. A peak at 2.97 ppm was found corresponding to the silyl imide =NSi*Me*$_3$.

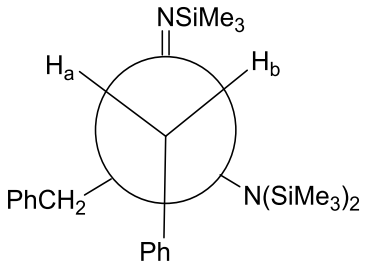

Figure 4.4. Newman projection of **10**.

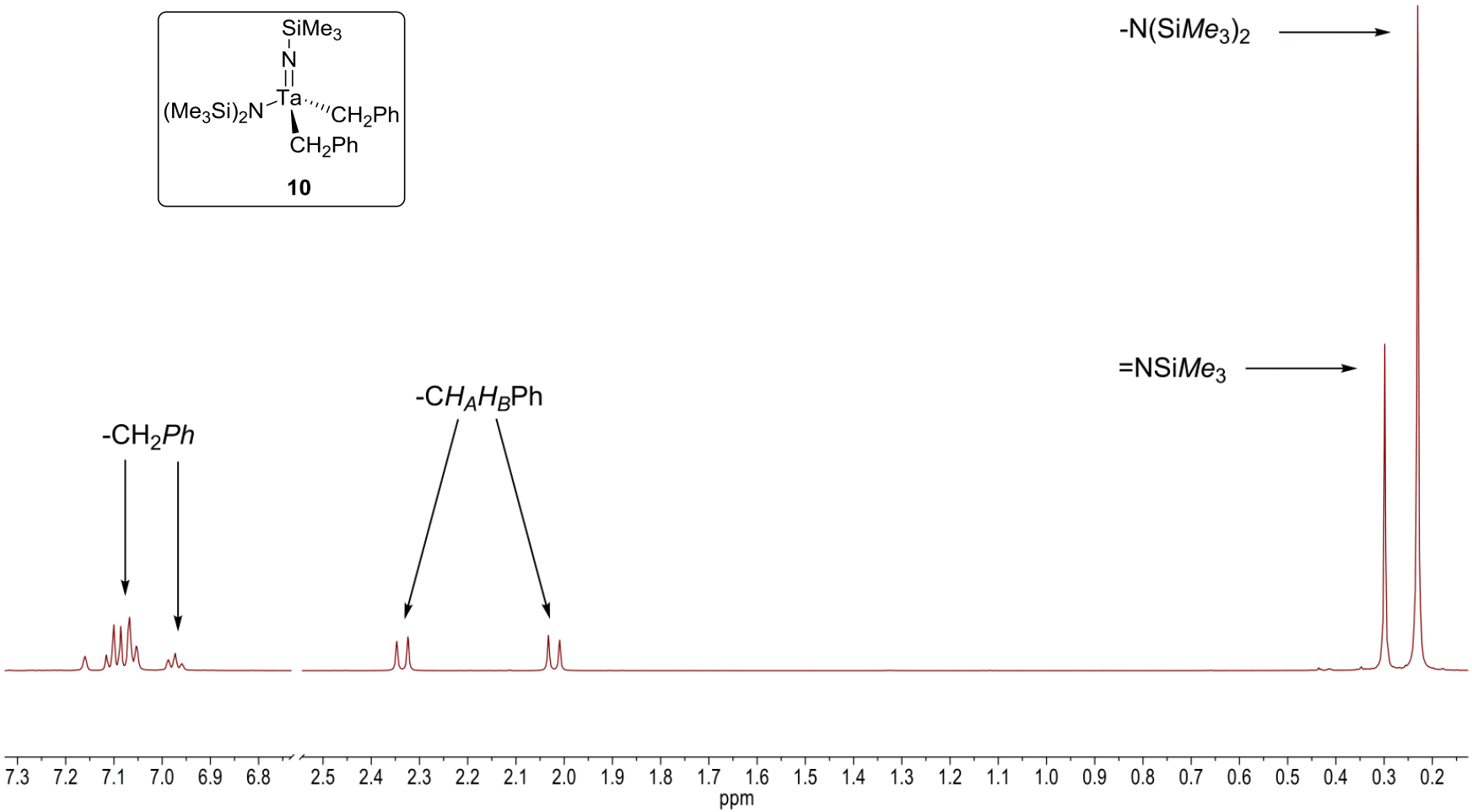

Figure 4.5. ^{1}H NMR spectrum of **10** in benzene-d_6 at 23 °C.

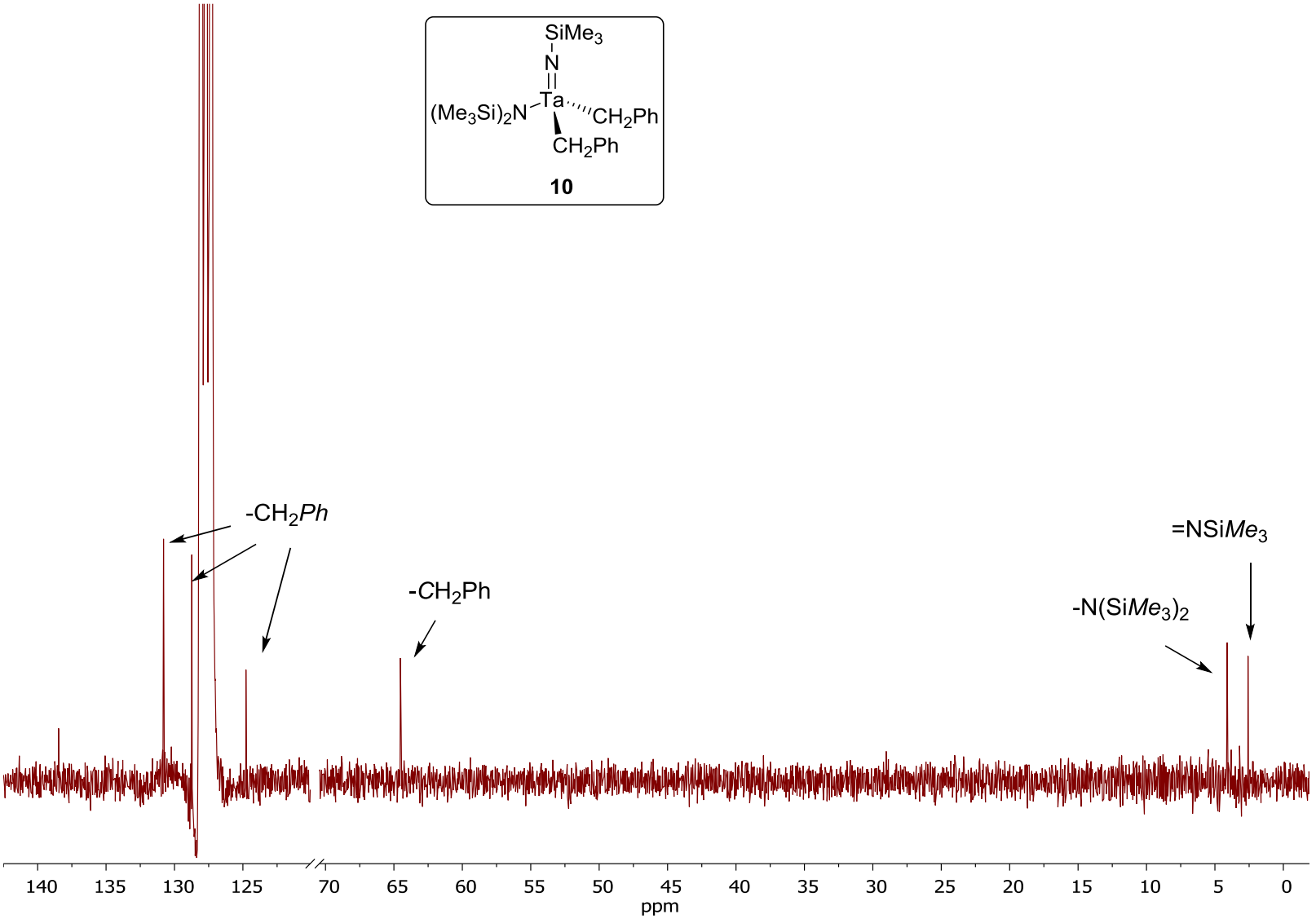

Figure 4.6. ^{13}C NMR spectrum of **10** in benzene-d_6 at 23 °C.

4.3.3. Crystal Structure of $Ta(CH_2Ph)_2(=NSiMe_3)[N(SiMe_3)_2]$ (10)

An ORTEP view of the crystal structure of **10** is given in Figure 4.7 (Top) and its crystal data are given in Tables 4.1-4.2. The metal center adopts a tetrahedral geometry. The Ta-N(2) bond length of 1.770(4) Å of $Ta=NSiMe_3$ and the Ta-N(1) length of 1.987(4) Å of $Ta-N(SiMe_3)_2$ are similar to those in $Ta(CH_2Bu^t)_2(=NSiMe_3)[N(SiMe_3)_2]$ (**10**), 1.770(6) Å for the imide bond and 1.981(7) Å for the amide bond.[25w] The Ta-C(11)-C(18) bond angle of 86.69° on one of the benzyl ligands suggests η^2 coordination of the delocalized electrons on the phenyl ring to the metal center (Figure 4.7, Bottom). This is reasonable due to the electron deficient metal center (10-14e^-). It is also in agreement with the observations by Parkin et al. on the binding modes of benzyl ligands.[30]

4.3.4. Synthesis of $Ta_2(\mu\text{-}OMe)_2(=NSiMe_3)_2[N(SiMe_3)_2]_2Me_2$ (*cis*-11 and *trans*-11)

Reaction of O_2 (0.5 equiv) with $TaMe_2(=NSiMe_3)[N(SiMe_3)_2]$ (**9**) led to the formation of a mixture of the methoxy methyl dimer ***cis*-11** and ***trans*-11** (Scheme 4.6), which gave only ***trans*-11** as crystals. Oxygen selectively inserts into one Ta-Me bond in **9**. Such selective oxygen insertion is known (Scheme 4.7). For example, $Mo(=NR)_2Me_2$ (R = 2,6-$Pr^i_2C_6H_3$) reacts with O_2 to form $[Mo(=NR)_2Me(\mu\text{-}OMe)]_2$. (cyclo)$Si(NBu^t)_2TiMe_2$ reacts with O_2 forming $[(cyclo)Si(NBu^t)_2Ti(\mu\text{-}OMe)Me]_2$.[31,32]

Reaction of O_2 with the ***cis*-11/*trans*-11** mixture led to oxygen insertion into the remaining Ta-Me bonds in ***cis*-11/*trans*-11** to give a mixture of *cis*/*trans*-dimethoxy dimers $\{Ta(\mu\text{-}OMe)(OMe)(=NSiMe_3)[N(SiMe_3)_2]\}_2$ (Scheme 4.6) which had been prepared from the reaction of LiOMe with $\{Ta(\mu\text{-}Cl)Cl(=NSiMe_3)[N(SiMe_3)_2]\}_2$ (**8**).[4h]

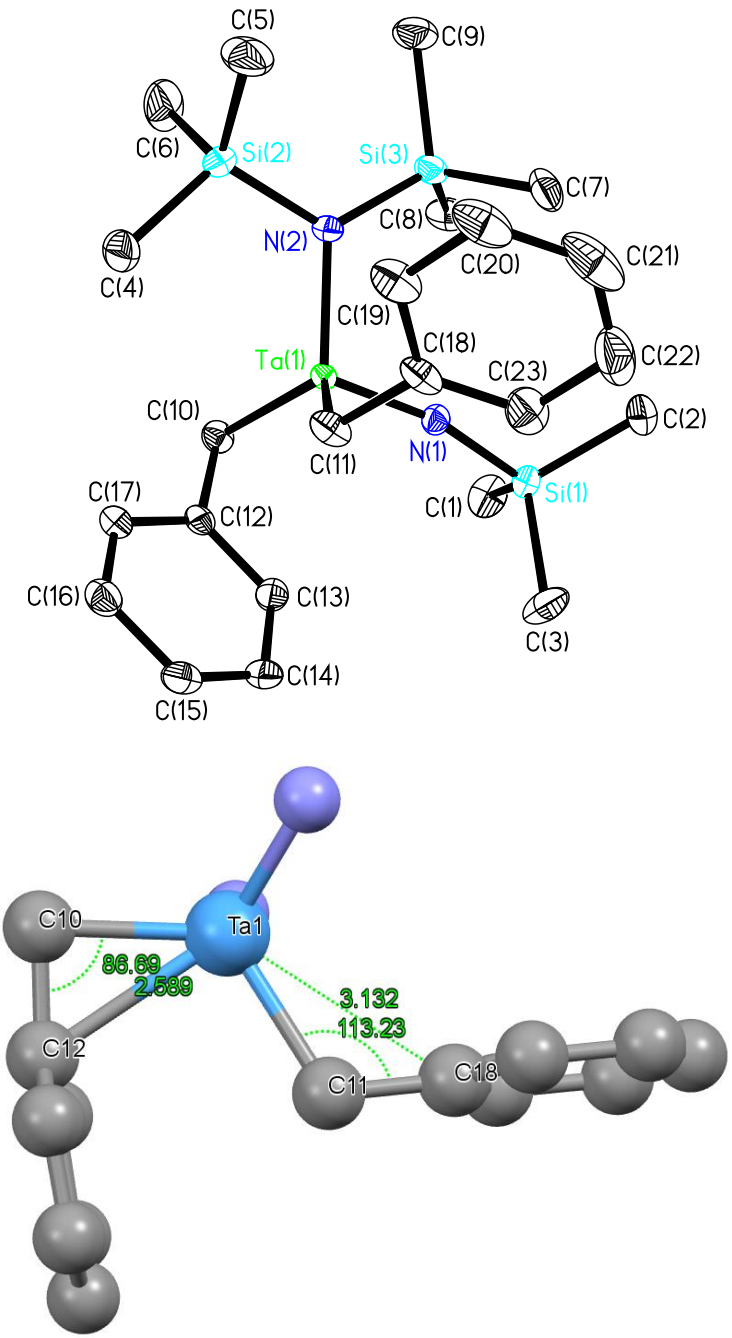

Figure 4.7. (Top) ORTEP view of **10**. (Bottom) Bonding of the two benzyl ligands to the Ta center in **10**.

Table 4.1. Crystal data and structure refinement for **10**

Empirical formula	C23 H41 N2 Si3 Ta	
Formula weight	610.80	
Temperature	100(2) K	
Wavelength	0.71073 Å	
Crystal system	Orthorhombic	
Space group	$P2_12_12_1$	
Unit cell dimensions	a = 9.5766(3) Å	α = 90°
	b = 17.0542(6) Å	β = 90°
	c = 17.4821(6) Å	γ = 90°
Volume	2855.20(17) $Å^3$	
Z	4	
Density (calculated)	1.421 Mg/m^3	
Absorption coefficient	3.987 mm^{-1}	
F(000)	1232	
Crystal size	0.20 x 0.18 x 0.15 mm^3	
θ range for data collection	1.668 to 28.323°	
Index ranges	$-12 \le h \le 12$, $-22 \le k \le 22$, $-23 \le l \le 22$	
Reflections collected	47821	
Independent reflections	7106 [R(int) = 0.0516]	
Completeness to θ = 25.242°	100.0%	

Table 4.1. Continued

Refinement method	Full-matrix least-squares on F^2
Data / restraints / parameters	7106 / 0 / 271
Goodness-of-fit on F^2	1.218
Final R indices [$I > 2\sigma(I)$]	$R1$ = 0.0412, w$R2$ = 0.1349
R indices (all data)	$R1$ = 0.0419, w$R2$ = 0.1364
Absolute structure parameter	0.966(4)
Largest diff. peak and hole	0.507 and -0.950 e.Å^{-3}

Table 4.2. Bond lengths (Å) and angles (°) for **10**

C(13)-C(12)	1.404(13)	N(2)-Si(2)-C(4)	109.8(5)
C(13)-C(14)	1.407(15)	C(6)-Si(2)-C(4)	107.8(7)
Ta(1)-N(1)	1.768(8)	N(2)-Si(2)-C(5)	111.3(6)
Ta(1)-N(2)	1.986(7)	C(6)-Si(2)-C(5)	109.9(9)
Ta(1)-C(10)	2.201(9)	C(4)-Si(2)-C(5)	106.4(7)
Ta(1)-C(11)	2.219(9)	N(2)-Si(3)-C(8)	110.3(5)
Si(2)-N(2)	1.747(8)	N(2)-Si(3)-C(9)	113.0(5)
Si(2)-C(6)	1.855(15)	C(8)-Si(3)-C(9)	105.5(6)
Si(2)-C(4)	1.870(13)	N(2)-Si(3)-C(7)	109.2(5)
Si(2)-C(5)	1.877(14)	C(8)-Si(3)-C(7)	112.0(6)
Si(3)-N(2)	1.763(8)	C(9)-Si(3)-C(7)	106.8(7)
Si(3)-C(8)	1.877(12)	N(1)-Si(1)-C(2)	111.3(5)
Si(3)-C(9)	1.878(12)	N(1)-Si(1)-C(1)	109.0(5)
Si(3)-C(7)	1.880(13)	C(2)-Si(1)-C(1)	109.3(7)
Si(1)-N(1)	1.731(8)	N(1)-Si(1)-C(3)	109.3(5)
Si(1)-C(2)	1.862(12)	C(2)-Si(1)-C(3)	108.7(7)
Si(1)-C(1)	1.868(12)	C(1)-Si(1)-C(3)	109.3(7)
Si(1)-C(3)	1.869(12)	Si(1)-N(1)-Ta(1)	167.5(5)
C(12)-C(17)	1.403(15)	Si(2)-N(2)-Si(3)	122.0(5)
C(12)-C(10)	1.496(14)	Si(2)-N(2)-Ta(1)	116.8(4)
C(11)-C(18)	1.503(12)	Si(3)-N(2)-Ta(1)	121.3(4)

Table 4.2. Continued

C(22)-C(21)	1.37(3)	C(17)-C(12)-C(13)	117.5(9)
C(22)-C(23)	1.424(18)	C(17)-C(12)-C(10)	121.8(9)
C(23)-C(18)	1.360(18)	C(13)-C(12)-C(10)	120.1(9)
C(19)-C(20)	1.390(16)	C(18)-C(11)-Ta(1)	113.2(6)
C(19)-C(18)	1.408(15)	C(12)-C(10)-Ta(1)	86.7(5)
C(21)-C(20)	1.36(3)	C(21)-C(22)-C(23)	119.9(15)
C(16)-C(17)	1.377(15)	C(18)-C(23)-C(22)	120.1(15)
C(16)-C(15)	1.420(15)	C(20)-C(19)-C(18)	120.2(13)
C(15)-C(14)	1.374(17)	C(23)-C(18)-C(19)	118.9(10)
C(12)-C(13)-C(14)	120.9(10)	C(23)-C(18)-C(11)	123.4(11)
N(1)-Ta(1)-N(2)	106.9(3)	C(19)-C(18)-C(11)	117.7(10)
N(1)-Ta(1)-C(10)	102.2(4)	C(20)-C(21)-C(22)	120.4(12)
N(2)-Ta(1)-C(10)	111.6(3)	C(21)-C(20)-C(19)	120.5(14)
N(1)-Ta(1)-C(11)	103.4(4)	C(17)-C(16)-C(15)	119.9(10)
N(2)-Ta(1)-C(11)	109.6(4)	C(16)-C(17)-C(12)	121.9(10)
C(10)-Ta(1)-C(11)	121.7(4)	C(14)-C(15)-C(16)	119.1(10)
N(2)-Si(2)-C(6)	111.4(7)	C(15)-C(14)-C(13)	120.6(10)

Symmetry transformations used to generate equivalent atoms:

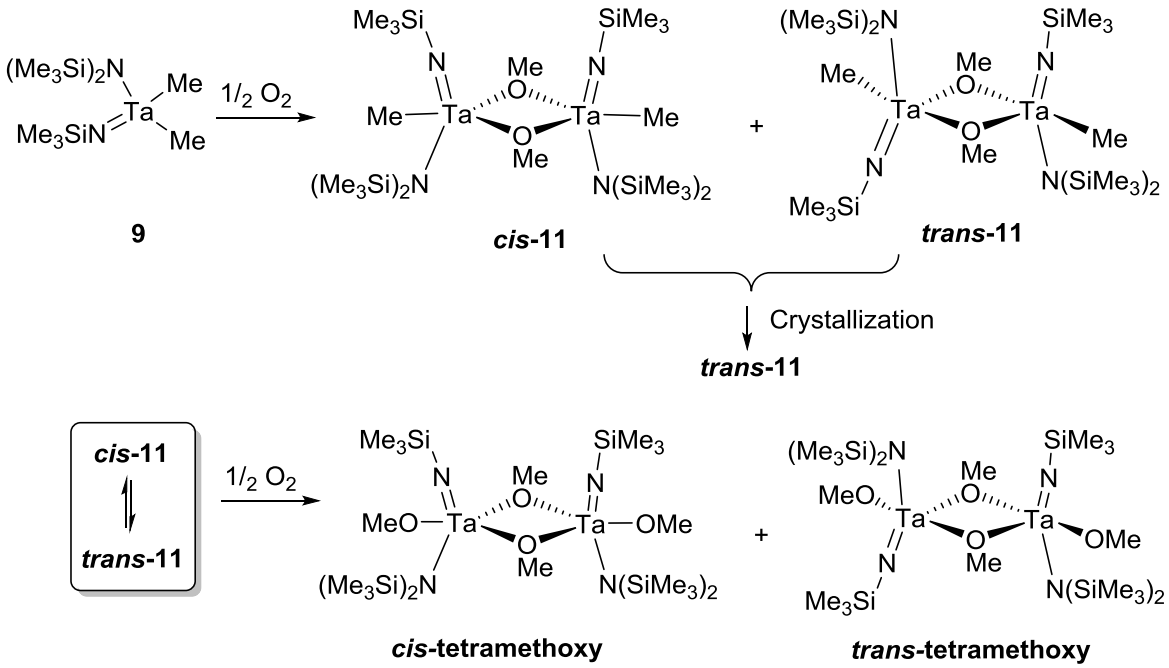

Scheme 4.6. Synthesis of a ***cis*-11**/***trans*-11** mixture, its crystallization to give ***trans*-11** only, and the ***cis*-11** ⇌ ***trans*-11** exchange. Reaction of the mixture with O_2 leads to oxygen insertion into Ta-Me bonds to give a mixture of *cis*/*trans*-dimethoxy dimers.

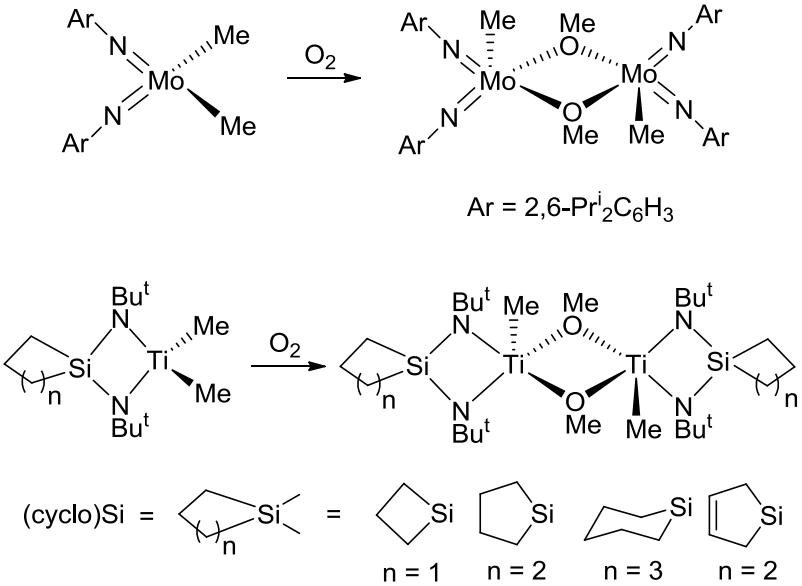

Scheme 4.7. Previous examples of selective oxygen insertion.[31,32]

A solution of ***trans*-11** in benzene-d_6, prepared from crystals of ***trans*-11**, slowly converted to its *cis* isomer ***cis*-11**, eventually reaching an exchange equilibrium, ***cis*-11** ⇌ ***trans*-11**, with K_{eq} = 0.78(0.02) (Scheme 4.6). Similar exchange was reported for {Ta(μ-OMe)(OMe)(=NSiMe$_3$)[N(SiMe$_3$)$_2$]}$_2$.[4h] The ^{1}H NMR spectrum of ***trans*-11** in benzene-d_6 (Figure 4.8) showed a singlet at 0.31 ppm for =NSi*Me*$_3$ ligand. A singlet at 0.42 ppm was observed for N(Si*Me*$_3$)$_2$. The *Me* and O*Me* peaks were at 0.62 and 3.78 ppm, respectively. The ^{1}H NMR of a ***cis*/*trans*-11** mixture at equilibrium is given in Figure 4.9. The ^{1}H NMR spectrum of ***cis*-11** in benzene-d_6 (Figure 4.9) showed a singlet at 0.33 ppm for =NSi*Me*$_3$. A singlet at 0.40 ppm was observed for N(Si*Me*$_3$)$_2$. The *Me* and O*Me* peaks were at 0.65 and 3.86 ppm, respectively.

The assignments of the ^{13}C NMR spectrum of the ***cis*-11/*trans*-11** mixture in benzene-d_6 (Figure 4.10) were assisted by HSQC NMR (Figure 4.11). For ***trans*-11**, the O*Me* and *Me* ligands were observed at 63.09 and 42.21 ppm, respectively. The =NSi*Me*$_3$ peak was at 3.55 ppm. A broad overlapping peak for the N(Si*Me*$_3$)$_2$ ligands in ***cis*-11** and ***trans*-11** was observed at 4.39 ppm. For ***cis*-11**, the *Me* and =NSi*Me*$_3$ ligands were at 41.61 and 3.47 ppm, respectively. The O*Me* peak was not directly observed in the ^{13}C NMR spectra (Figure 4.10), but the HSQC spectrum indicated that it was a broad peak at 64.16 ppm overlapping with the O*Me* peak in ***trans*-11**. These observations perhaps indicate exchanges in ***cis*-11** and ***trans*-11**.

4.3.5. Crystal Structure of Ta$_2$(μ-OMe)$_2$(=NSiMe$_3$)$_2$[N(SiMe$_3$)$_2$]$_2$Me$_2$ (*trans*-11)

An ORTEP view of the crystal structure of ***trans*-11** is given in Figure 4.10 and its crystal data are given in Tables 4.5-4.6. The structure of ***trans*-11** consists of two

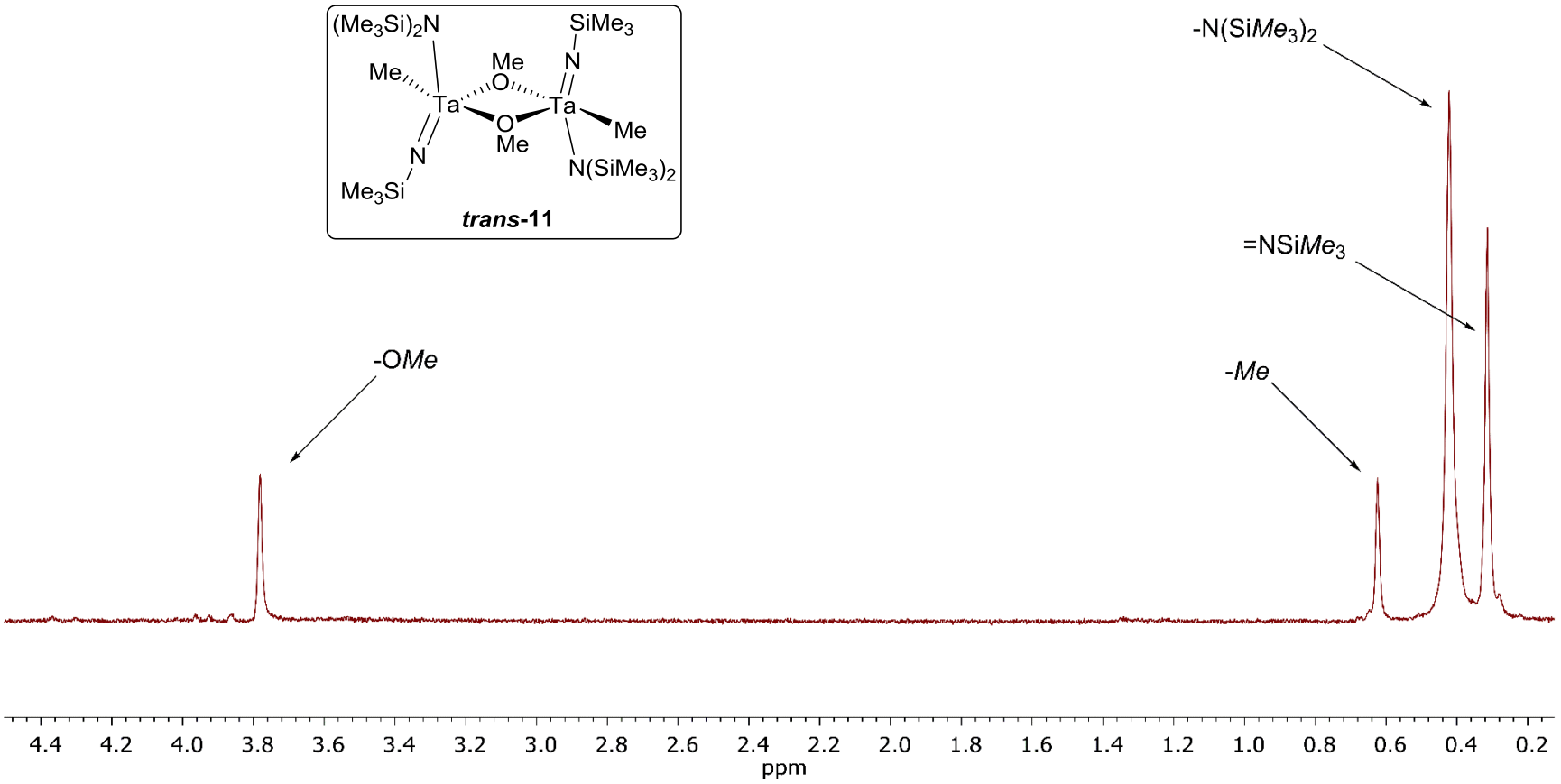

Figure 4.8. ^{1}H NMR spectrum of ***trans*-11** in benzene-d_6 at 23 °C.

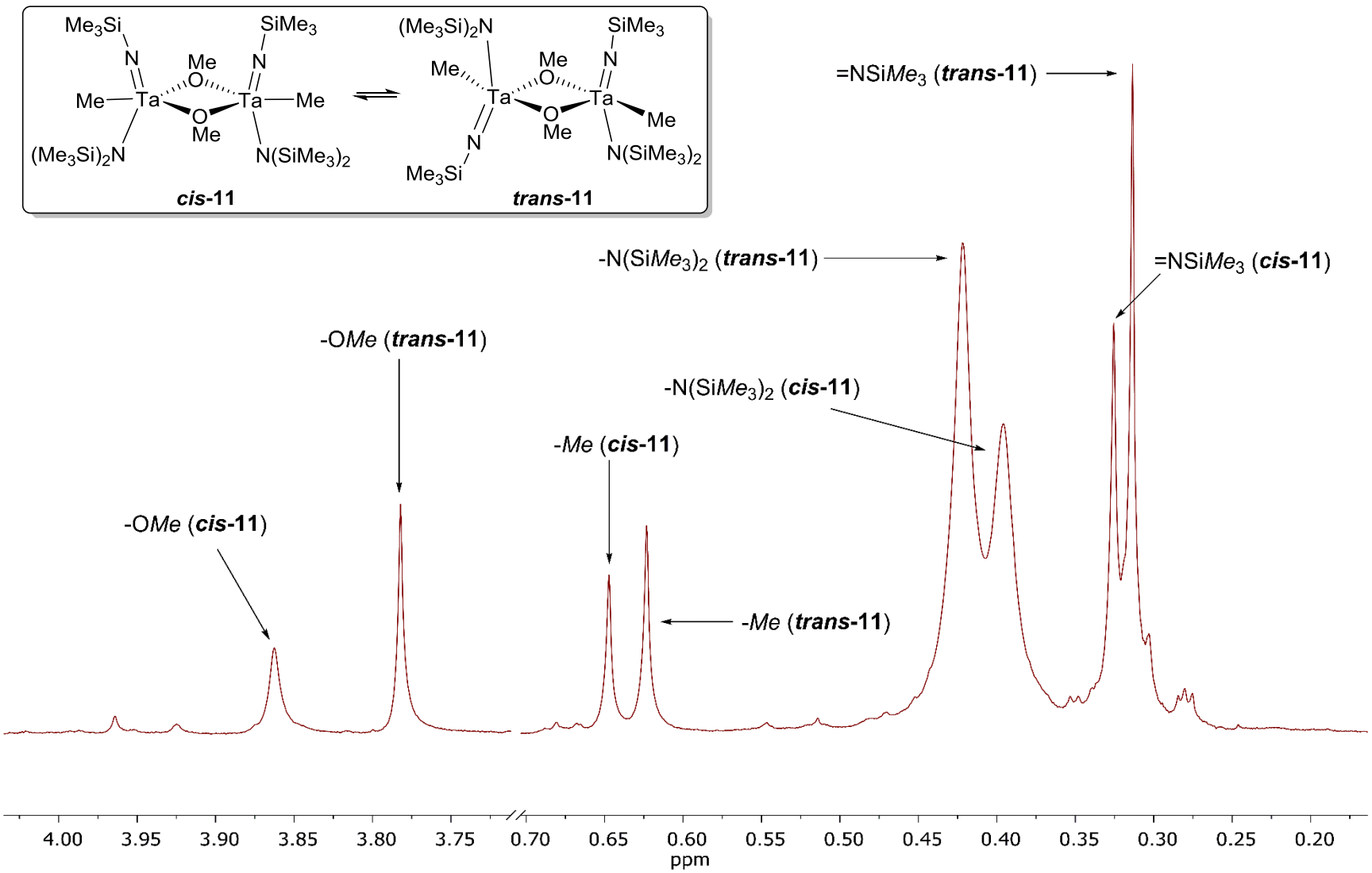

Figure 4.9. ^{1}H NMR spectrum of a ***cis*-11** and ***trans*-11** mixture in benzene-d_6 at 23 °C.

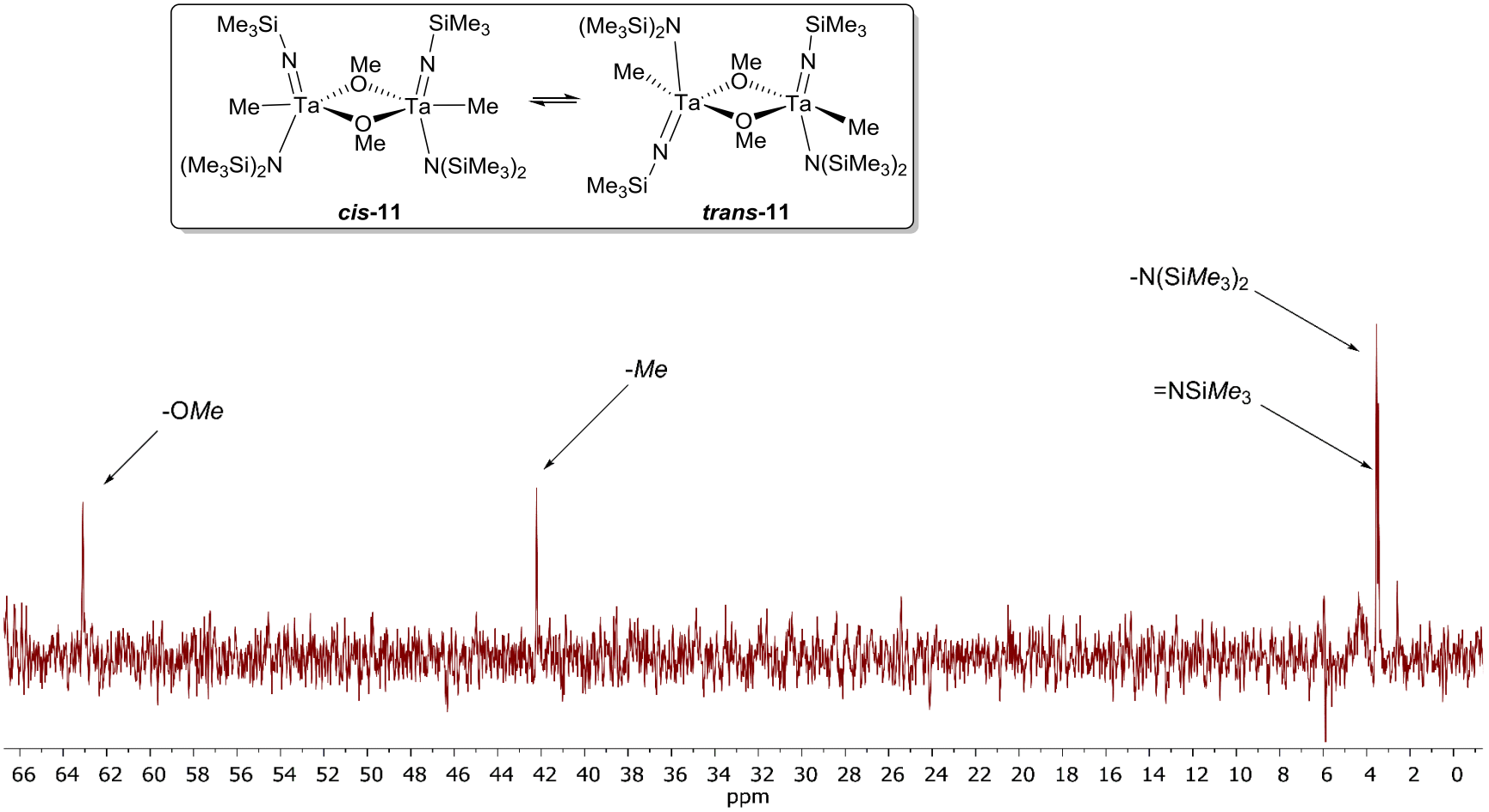

Figure 4.10. ^{13}C NMR spectrum of a ***cis*-11** and ***trans*-11** mixture in benzene-d_6 at 23 °C.

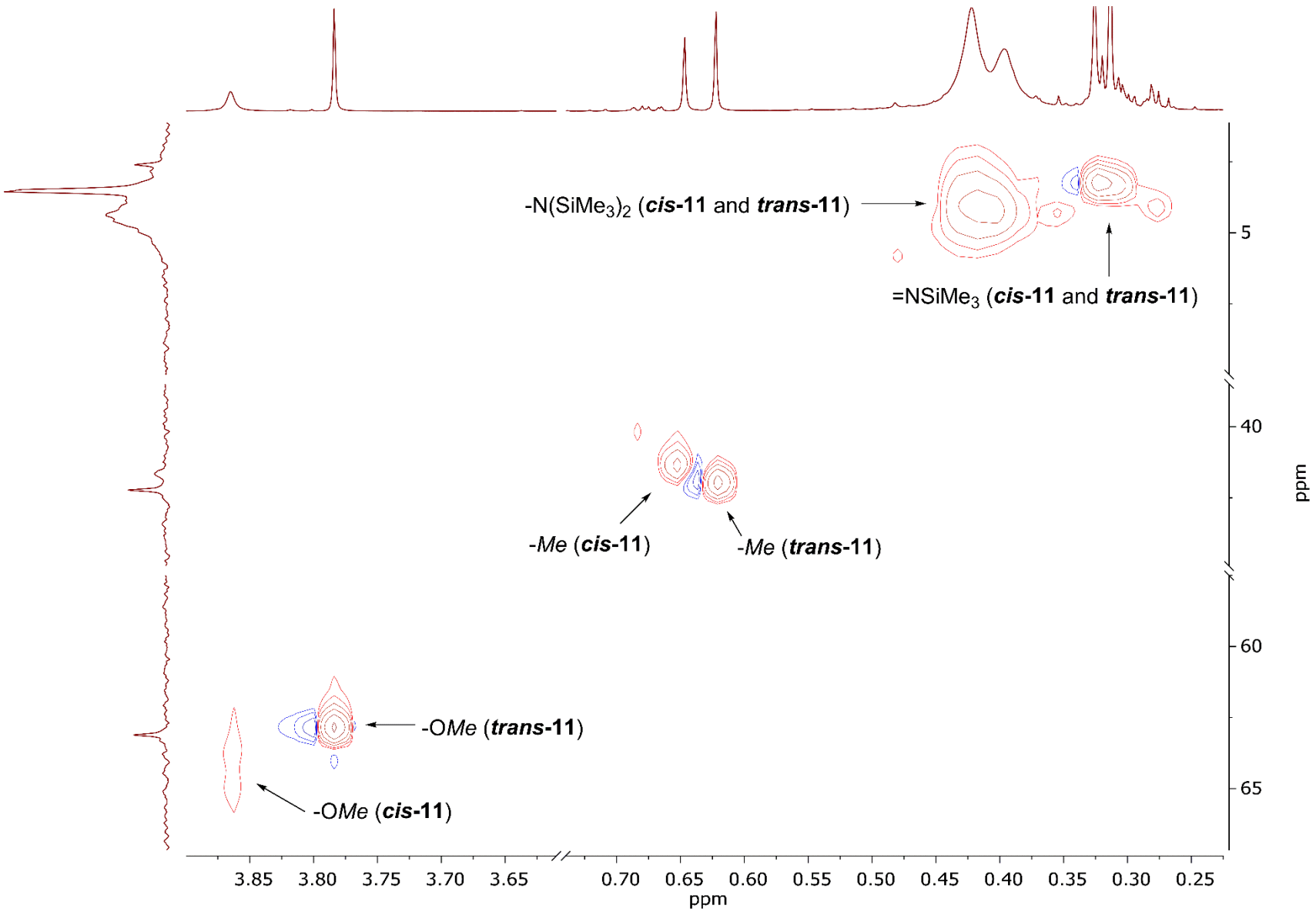

Figure 4.11. HSQC spectrum of a ***cis*-11** and ***trans*-11** mixture in benzene-d_6 at 23 °C.

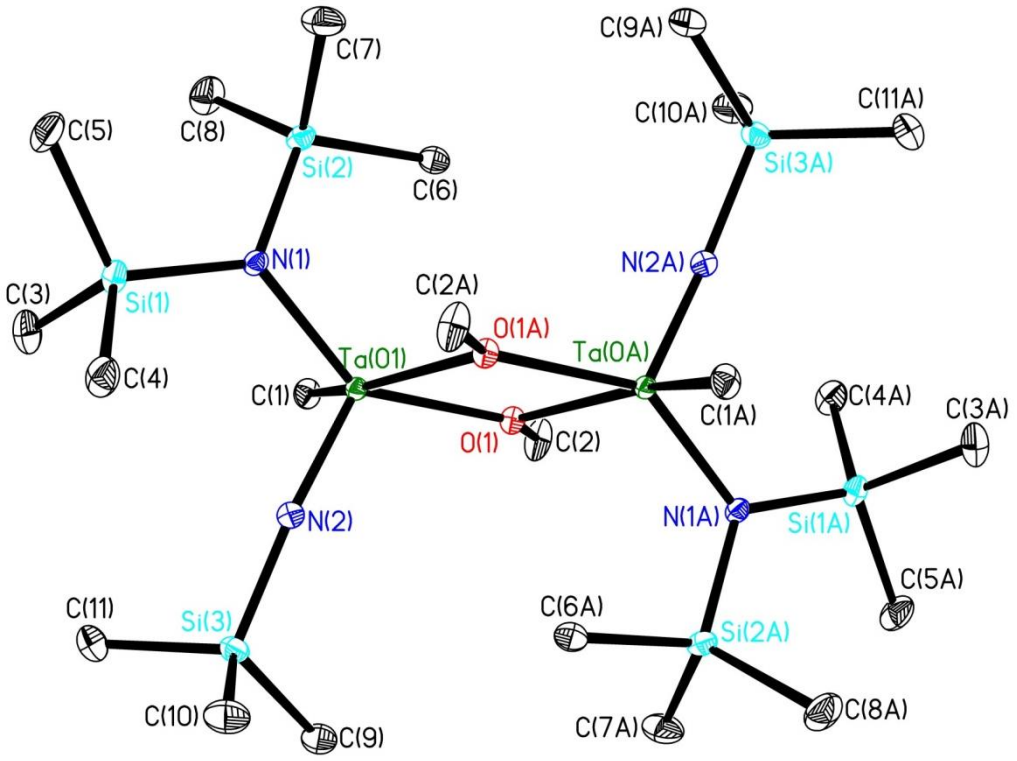

Figure 4.12. ORTEP view of ***trans*-11**.

Table 4.3. Crystal data and structure refinement for ***trans*-11**

Empirical formula	C22 H66 N4 O2 Si6 Ta2	
Formula weight	949.22	
Temperature	100(2) K	
Wavelength	0.71073 Å	
Crystal system	Monoclinic	
Space group	$P2_1/n$	
Unit cell dimensions	a = 9.4036(7) Å	α = 90°
	b = 16.0261(11) Å	β = 92.7050(10)°
	c = 13.5459(10) Å	γ = 90°
Volume	2039.1(3) Å^3	
Z	2	
Density (calculated)	1.546 Mg/m^3	
Absorption coefficient	5.561 mm^{-1}	
F(000)	944	
Crystal size	0.105 x 0.064 x 0.029 mm^3	
θ range for data collection	1.970 to 28.802°	
Index ranges	$-12 \le h \le 12$, $-21 \le k \le 21$, $-18 \le l \le 18$	
Reflections collected	23774	
Independent reflections	5007 [R(int) = 0.0237]	
Completeness to θ = 25.242°	99.9%	

Table 4.3. Continued

Absorption correction	Semi-empirical from equivalents
Max. and min. transmission	0.851 and 0.659
Refinement method	Full-matrix least-squares on F^2
Data / restraints / parameters	5007 / 0 / 174
Goodness-of-fit on F^2	1.110
Final R indices [$I > 2\sigma(I)$]	$R1$ = 0.0172, w$R2$ = 0.0461
R indices (all data)	$R1$ = 0.0189, w$R2$ = 0.0469
Largest diff. peak and hole	1.772 and -0.608 e.Å^{-3}

Table 4.4. Bond lengths (Å) and angles (°) for ***trans*-11**

Ta(01)-N(2)	1.780(2)	O(1)-Ta(01)-C(1)	86.24(8)
Ta(01)-N(1)	1.9967(19)	O(1A)-Ta(01)-C(1)	149.89(8)
Ta(01)-O(1)	2.1244(16)	N(1)-Si(1)-C(4)	112.09(11)
Ta(01)-O(1A)	2.1376(16)	N(1)-Si(1)-C(3)	109.63(12)
Ta(01)-C(1)	2.199(2)	C(4)-Si(1)-C(3)	110.48(15)
Si(1)-N(1)	1.762(2)	N(1)-Si(1)-C(5)	112.16(12)
Si(1)-C(4)	1.860(3)	C(4)-Si(1)-C(5)	104.55(14)
Si(1)-C(3)	1.862(3)	C(3)-Si(1)-C(5)	107.76(15)
Si(1)-C(5)	1.873(3)	N(1)-Si(2)-C(7)	111.57(12)
Si(2)-N(1)	1.751(2)	N(1)-Si(2)-C(8)	110.46(12)
Si(2)-C(7)	1.865(3)	C(7)-Si(2)-C(8)	111.83(15)
Si(2)-C(8)	1.866(3)	N(1)-Si(2)-C(6)	109.84(11)
Si(2)-C(6)	1.876(3)	C(7)-Si(2)-C(6)	105.73(13)
Si(3)-N(2)	1.727(2)	C(8)-Si(2)-C(6)	107.21(13)
Si(3)-C(11)	1.863(3)	N(2)-Si(3)-C(11)	108.82(12)
Si(3)-C(10)	1.867(3)	N(2)-Si(3)-C(10)	110.25(12)
Si(3)-C(9)	1.873(3)	C(11)-Si(3)-C(10)	110.08(15)
O(1)-C(2)	1.435(3)	N(2)-Si(3)-C(9)	110.45(12)
O(1)-Ta(0A)	2.1376(16)	C(11)-Si(3)-C(9)	107.93(14)
N(2)-Ta(01)-N(1)	107.13(9)	C(10)-Si(3)-C(9)	109.28(14)
N(2)-Ta(01)-O(1)	110.41(8)	C(2)-O(1)-Ta(01)	129.02(15)

Table 4.4. Continued

N(1)-Ta(01)-O(1)	141.73(7)	C(2)-O(1)-Ta(0A)	118.00(15)
N(2)-Ta(01)-O(1A)	105.57(8)	Ta(01)-O(1)-Ta(0A)	112.06(7)
N(1)-Ta(01)-O(1A)	95.17(7)	Si(2)-N(1)-Si(1)	120.98(11)
O(1)-Ta(01)-O(1A)	67.95(7)	Si(2)-N(1)-Ta(01)	113.38(10)
N(2)-Ta(01)-C(1)	97.62(10)	Si(1)-N(1)-Ta(01)	124.37(11)
N(1)-Ta(01)-C(1)	96.08(9)	Si(3)-N(2)-Ta(01)	166.53(14)

Symmetry transformations used to generate equivalent atoms:

#1 -*x*+1,-*y*+1,-*z*+1

equivalent tantalum centers, each adopting a distorted trigonal bipyramidal environment. The bond lengths of the Ta-N imide and amide bonds in ***trans*-11**, 1.780 and 1.996 Å, respectively, are similar to those in the dimethoxy dimer analogue *trans*-{Ta(μ-OMe)(OMe)(=NSiMe$_3$)[N(SiMe$_3$)$_2$]}$_2$ (1.777, 2.023 Å).[4h]

4.3.6. Reaction of Ta(CH$_2$Ph)$_2$(=NSiMe$_3$)[N(SiMe$_3$)$_2$] (10) and O$_2$

Ta(CH$_2$Ph)$_2$(=NSiMe$_3$)[N(SiMe$_3$)$_2$] (**10**) completely reacts within 24 h with 1 atm of O$_2$ at room temperature to give multiple products. ^{1}H and ^{13}C NMR spectra show multiple peaks in regions that are typical for benzoxy ligands O*CH*$_2$Ph. Attempts to separate products were unsuccessful. The reaction between {Ta(μ-Cl)Cl(=NSiMe$_3$)[N(SiMe$_3$)$_2$]}$_2$ (**8**) and LiOBn (Bn = benzyl) also gave multiple products which have the same NMR peaks in the benzoxy region. This observation suggests that Ta(=NSiMe$_3$)[N(SiMe$_3$)$_2$](OCH$_2$Ph)$_2$ might have formed initially but then undergoes a ligand exchange similar to that in the alkoxide Ta(=NSiMe$_3$)[N(SiMe$_3$)$_2$](OCH$_2$Bu^t)$_2$ our groups previously reported.[25w]

4.4. Concluding Remarks

In this part, the syntheses of the alkyl amide imide complexes TaMe$_2$(=NSiMe$_3$)[N(SiMe$_3$)$_2$] (**9**) and Ta(CH$_2$Ph)$_2$(=NSiMe$_3$)[N(SiMe$_3$)$_2$] (**10**) and their reactions with O$_2$ are reported. Oxygen initially inserts into only one Ta-Me bond of the two methyl ligands in **9** to form the methoxy dimer Ta$_2$(μ-OMe)$_2$(=NSiMe$_3$)$_2$[N(SiMe$_3$)$_2$]$_2$Me$_2$ (***cis*-11** and ***trans*-11**). A mixture of ***cis*-11** and ***trans*-11** reacts with additional O$_2$ to give {Ta(μ-OMe)(OMe)(=NSiMe$_3$)[N(SiMe$_3$)$_2$]}$_2$. ***Cis*-11** and ***trans*-11** undergo an exchange, reaching equilibrium.

References

1. (a) Berry, J. F. *Comments Inorg. Chem.* **2009**, *30*, 28. (b) Schrock, R. R. *Chem. Rev.* **2009**, *109,* 3211. (c) Zarubin, D.; Ustynyuk, N. *Russ. Chem. Rev.* **2006**, *75,* 671. (d) Eikey, R.; Abu-Omar, M. *Coord. Chem. Rev.* **2003**, *243,* 83. (e) Li, Y.; Wong, W. *Coord. Chem. Rev.* **2003**, *243,* 191. (f) Gade, L.; Mountford, P. *Coord. Chem. Rev.* **2001**, *216−217,* 65. (g) Nugent, W. A.; Mayer, J. M. Metal−Ligand Multiple Bonds; Wiley-Interscience: New York, 1988. (h) Rosenfeld, D. C.; Wolczanski, P. T.; Barakat, K. A.; Buda, C.; Cundari, T. R.; Schroeder, F. C.; Lobkovsky, E. B. *Inorg. Chem.* **2007**, *46,* 9715. (i) Holland, P. L.; Andersen, R. A.; Bergman, R. G. *Organometallics* **1998**, *17,* 433. (j) Burland, M. C.; Pontz, T. W.; Meyer, T. Y. *Organometallics* **2002**, *21,* 1933. (k) Brown, S. D.; Peters, J. C. *J. Am. Chem. Soc.* **2004**, *126,* 4538. (l) Bailey, B. C.; Huffman, J. C.; Mindiola, D. J.; Weng, W.; Ozerov, O. V. *Organometallics* **2005**, *24,* 1390. (m) Kogut, E.; Wiencko, H. L.; Zhang, L.; Cordeau, D. E.; Warren, T. H. *J. Am. Chem. Soc.* **2005**, *127,* 11248. (n) Bart, S. C.; Lobkovsky, E.; Bill, E.; Chirik, P. J. *J. Am. Chem. Soc.* **2006**, *128,* 5302. (o) Ison, E. A.; Abboud, K. A.; Boncella, J. M. *Organometallics* **2006**, *25,* 1557. (p) Shaver, M. P.; Fryzuk, M. D. *J. Am. Chem. Soc.* **2005**, *127,* 500. (q) Sceats, E. L.; Figueroa, J. S.; Cummins, C. C.; Loening, N. M.; Van der Wel, P.; Griffin, R. G. *Polyhedron* **2004**, *23,* 2751. (r) Shay, D. T.; Yap, G. P. A.; Zakharov, L. N.; Rheingold, A. L.; Theopold, K. H. *Angew. Chem., Int. Ed.* **2005**, *44,* 1508.
2. (a) Jiang, A. J.; Simpson, J. H.; Mueller, P.; Schrock, R. R. *J. Am. Chem. Soc.* **2009**, *131,* 7770. (b) Bolton, P.; Mountford, P. *Adv. Synth. Catal.* **2005**, *347,* 355.

(c) Poater, A.; Solans-Monfort, X.; Clot, E.; Copéret, C.; Eisenstein, O. *J. Am. Chem. Soc.* **2007**, *129,* 8207. (d) Ong, T.-G.; Yap, G. P. A.; Richeson, D. S. *Chem. Commun.* **2003**, *20,* 2612.

3. (a) Baunemann, A.; Kim, Y.; Winter, M.; Fischer, R. A. *Dalton Trans.* **2006**, 121. (b) Chiu, H.; Wang, C.; Chuang, S. *Chem. Vap. Deposition* **2000**, *6,* 223. (c) Jayaratne, K. C.; Yap, G. P. A.; Haggerty, B. S.; Rheingold, A. L.; Winter, C. H. *Inorg. Chem.* **1996**, *35,* 4910.

4. (a) Chong, A. O.; Oshima, K.; Sharpless, K. B. *J. Am. Chem. Soc.* **1977**, *99*, 3420. (b) Maatta, E. A.; Haymore, B. L.; Wentworth, R. A. D. *Inorg. Chem.* **1980**, *19*, 1055. (c) Lam, H. –W.; Wilkinson, G.; Hussain-Bates, B.; Hursthouse, M. B. *J. Chem. Soc. Dalton Trans.* **1993**, 1477. (d) Burger, U.; Wannagat, U. *Monatsh. Chem.* **1963**, *94*, 761. (e) Burger, H.; Smrekar, O. *Monatsh. Chem.* **1964**, *95*, 292. (f) Nugent, W. A.; Harlo, R. L. *J. Chem. Soc., Chem. Commun.* **1978**, 579. (g) Jones, C. M.; Lerchen, M. E.; Church, C. J.; Schomber, B. M.; Doherty, N. M. *Inorg. Chem.* **1990**, *29*, 1679. (h) Bradley, D. C.; Hursthouse, M. B.; Howes, A. J.; Jelfs, A. N. D.; Runnacles, J. D.; Thorntonpett, M. *J. Chem. Soc.-Dalton Trans.* **1991**, 841. (i) Rossi, R.; Marchi, A.; Duatti, A.; Magon, L.; Bernado, P. *Transition Met. Chem.* **1985**, *10*, 151.

5. (a) Bradley, D. C.; Thomas, I. M. *Can. J. Chem.* **1962**, *40*, 1355. (b) Davies, H. O.; Jones, A. C.; McKinnell, E. A.; Raftery, J.; Muryn, C. A.; Afzaal, M.; O'Brien, P. *J. Mater. Chem.* **2006**, *16*, 2226. (c) Chen, S.-J.; Zhang, J.; Yu, X.; Bu, X.; Chen, X.-T.; Xue, Z.-L. *Inorg. Chem.* **2010**, *49*, 4017.

6. (a) Son, K.-A.; Mao, A. Y.; Sun, Y.-M.; Kim, B. Y.; Liu, F.; Kamath, A.; White, J. M.; Kwong, D. L.; Roberts, D. A.; Vrtis, R. N. *Appl. Phys. Lett.* **1998**, *72*, 1187. (b) Niimi, H.; Johnson, R. S.; Lucovsky, G.; Massoud, H. Z. *Proc. Electrochem. Soc.* **2000**, *2000-2*, 487. (c) Rodriguez-Reyes, J. C. F.; Teplyakov, A. V. *J. Appl. Phys.* **2008**, *104*, 084907/1. (d) Hausmann, D. M.; de Rouffignac, P.; Smith, A.; Gordon, R.; Monsma, D. *Thin Solid Films* **2003**, *443*, 1. (f) Wiedmann, M. K.; Heeg, M. J.; Winter, C. H. *Inorg. Chem.* **2009**, *48*, 5382. (g) Dezelah, C. L., IV; Wiedmann, M. K.; Mizohata, K.; Baird, R. J.; Niinistoe, L.; Winter, C. H. *J. Am. Chem. Soc.* **2007**, *129*, 12370.

7. (a) Fix, R.; Gordon, R. G.; Hoffman, D. M. *Chem. Mater.* **1993**, *5*, 614. (b) Juppo, M.; Ritala, M.; Leskelä, M. *J. Electrochem. Soc.* **2000**, *147*, 3377. (c) Leng, Y. X.; Sun, H.; Yang, P.; Chen, J. Y.; Wang, J.; Wan, G. J.; Huang, N.; Tian, X. B.; Wang, L. P.; Chu, P. K. *Thin Soild Films* **2001**, *398-399*, 471. (d) Leskelä, M.; Ritala, M. *Angew. Chem. Int. Ed.* **2003**, *42*, 5548. (e) Aouadi, S. M.; Debessai, M. *J. Vac. Sci. Technol. A* **2004**, *22*, 1975. (f) Rayner Jr.; G. B.; George, S. M. *J. Vac. Sci. Technol. A* **2009**, *27*, 716. (g) Shen, L.; Wang, N. *J. Nanomater.* **2011**, 2011, article ID 781935. (h) Zhou, Y.; Jin, P.; Chen, S.; Zhu, Y. Mater. Lett. **2014**, *136*, 168.

8. Rockett, A. The Materials Science of Semiconductors, Springer Science+Business Media, LLC, New York, 2008.

9. Smith, R. C.; Ma, T.; Hoilien, N.; Tsung, L. Y.; Bevan, M. J.; Colombo, L.; Roberts, J.; Campbell, S. A.; Gladfelter, W. L. *Adv. Mater. Opt. Electron* **2000***, 10,* 105*.*

10. Wallace, R.; Wilk, G. D. *Crit. Rev. Solid State Mater. Sci.* **2003***, 28,* 231*.*

11. Wilk, G. D.; Wallace, R. M.; Anthony, J. M. *J. Appl. Phys.* **2001***, 89,* 5243*.*

12. Robertson, J. *Rep. Prog. Phys.* **2006**, *69*, *327.*

13. Arghavani, R.; Miner, G.; Agustin, M. *Semicond. Internal.* 2007, **30**, 32.

14. Jones, A. C.; Aspinall, H. C.; Chalker, P. R.; Potter, R. J.; Kukli, K.; Rahtu, A.; Ritala, M.; Leskelae, M. *J. Mater. Chem*. **2004**, *14,* 3101.

15. Wallace, R.; Wilk, G. D. *MRS Bull*. **2002**, *27*, 192.

16. Campbell, S. A. *Science and Engineering of Microelectronic Fabrication,* ed. A. S. Sedra, Oxford University Press, Oxford, 2nd Ed., 2001.

17. Panda, D.; Tseng, T. –Y. *Thin Solid Films* **2013**, *531,* 1.

18. (a) Hitchman, M. L.; Jenson, K. F. *Chemical Vapor Deposition: Principles and Applications*. eds. Hitchman, M. L.; Jenson, K. F. Academic Press Ltd. London, UK, 1993, 1. (b) Jenson, K. F. *Chemical Vapor Deposition: Principles and Applications*. eds. Hitchman, M. L.; Jenson, K. F. Academic Press Ltd. London, UK, 1993, 31.

19. Pierson, H. O. *Handbook of Chemical Vapor Deposition: Principles, Technology, and Applications.* eds. Bunshah, R. F.; McGuire, G. E.; Rossnagel, S. M. Noyes Publications, Park Ridge, New Jersey,1992.

20. *Vapor Deposition*, eds. Powell, C. F.; Oxley, J. H.; Blocher, J. M. The Electrochemical Society, New York, 1966.

21. (a) Feig, A. L.; Lippard, S. J. *Chem. Rev.* **1994**, *94*, 759. (b) Klotz, I. M.; Kurtz, D. M. *Chem. Rev.* **1994**, *94*, 567. (c) Theopold, K. H.; Reinaud, O. M.; Blanchard, S.; Leelasubeharoen, S.; Hess, A.; Thyagarajan, S. *ACS Symp. Ser.* **2002**, *823*, 75. (d) Kopp, D. A.; Lippard, S. J. *Curr. Opin. Chem. Biol.* **2002**, *6*, 568. (e) Que, L., Jr.; Tolman, W. B. *Angew. Chem. Int. Ed.* **2002**, *41*, 1114. (f) Brown, S. N.; Mayer,

J.M. *Inorg. Chem.* **1992**, *31*, 4091. (g) Balch, A. L.; Cornman, C. R.; Olmstead, M. M. *J. Am. Chem. Soc.* **1990**,*112*, 2963.

22. *Advances in Catalytic Activation of Dioxygen by Metal Complexes*; Sim_andi, L. I., Ed.; Kluwer: Boston: Catalytic Metal Complexes, Vol. 26; 2003: (a) Ezhova, M. B.; James, B. R. in pp 1-77. (b) Zhang, C. X.; Liang, H.-C.; Humphreys, K. J.; Karlin, K. D. in pp 79-121. (c) Funabiki, T. in pp 157-226. (d) Boring, E.; Geletii, Y. V.; Hill, C. L. in pp 227-264. (e) Simandi, L. I. in pp 265-328.
23. *The Activation of Dioxygen and Homogeneous Catalytic Oxidation*; Barton, D. H. R.; Martell, A. E.; Sawyer,D. T., Eds.; Plenum: NewYork, 1993.
24. (a) Que, L.; Tolman, W. B. *Nature* **2008**, *455*, 333. (b) Yokoyama, A.; Han, J. E.; Cho, J.; Kubo, M.; Ogura, T.; Siegler, M. A.; Karlin, K. D.; Nam, W. *J. Am. Chem. Soc.* **2012**, *134*, 15269. (c) Campbell, A. N.; Stahl, S. S. *Acc. Chem. Res.* **2012**, *45*, 851. (d) Shook, R. L.; Borovik, A. S. *Chem. Commun.* **2008**, 6095. (e) Monillas, W. H.; Yap, G. P. A.; MacAdams, L. A.; Theopold, K. H. *J. Am. Chem. Soc.* **2007**, *129*, 8090. (f) McQuilken, A. C.; Jiang, Y.; Siegler, M. A.; Goldberg, D. P. *J. Am. Chem. Soc.* **2012**, *134*, 8758. (g) Scheuermann, M. L.; Fekl, U.; Kaminsky, W.; Goldberg, K. I. *Organometallics* **2010**, *29*, 4749. (h) Khusnutdinova, J. R.; Rath, N. P.; Mirica, L. M. *J. Am. Chem. Soc.* **2012**, *134*, 2414. (i) Nguyen, K. T.; Rath, S. P.; Latos-Grazynski, L.; Olmstead, M. M.; Balch, A. L. *J. Am. Chem. Soc.* **2004**, *126*, 6210. (j) Kelley, M. R.; Rohde, J.-U. *Chem. Commun.* **2012**, *48*, 2876. (k) Frisch, J. R.; McDonnell, R.; Rybak-Akimova, E. V.; Que Jr., L. *Inorg. Chem.* **2013**, *52*, 2627.

25. (a) Stanciu, C.; Jones, M. E.; Fanwick, P. E.; Abu-Omar, M. M. *J. Am. Chem. Soc.* **2007**, *129*, 12400. (b) Tilley, T. D. *Organometallics*, **1985**, *4*, 1452. (c) Blackburn, T. F.; Labinger, J. A.; Schwartz, J. *Tetrahedron Lett.* **1975**, *16*, 3041. (d) Lubben, T. V.; Wolczanski, P. T. *J. Am. Chem. Soc.* **1987**, *109*, 424. (e) Wang, R.; Folting, K.; Huffman, J. C.; Chamberlain, L. R.; Rothwell, I. P. *Inorg. Chim. Acta* **1986**, *120*, 81. (f) Gibson, V. C.; Redshaw, C.; Walker, G. L. P.; Howard, J. A. K.; Hoy, V. J.; Cole, J. M.; Kuzmina, L. G.; De Silva, D. S. *Dalton Trans.* **1999**, 161. (g) Schaverien, C. J.; Orpen, A. G. *Inorg. Chem.* **1991**, *30*, 4968. (h) Liu, X.; Cui, D. *Dalton Trans.* **2008**, 3747. (i) Van Asselt, A.; Trimmer, M. S.; Henling, L. M.; Bercaw, J. E. *J. Am. Chem. Soc.* **1988**, *110*, 8254. (j) Brindley, P. B.; Hodgson, J. C. *J. Organomet. Chem.* **1974**, *65*, 57. (k) Boro, B. J.; Lansing, R.; Goldberg, K. I.; Kemp, R. A. *Inorg. Chem. Commun.* **2011**, *14*, 531. (l) Lu, F.; Zarkesh, R. A.; Heyduk, A. F. *Eur. J. Inorg. Chem.* **2012**, *3*, 467. (m) Chisholm, M. H.; Hammond, C. E.; Huffman, J. C. *Chem. Commun.* **1987**, 1423. (n) Wang, R.-T.; Zhang, X.-H.; Chen, S.-J.; Yu, X.-H.; Wang, C.-S.; Beach, D. B.; Wu, Y.-D.; Xue, Z.-L. *J. Am. Chem. Soc.* **2005**, *127*, 5204. (o) Chen, S.-J.; Zhang, X.-H.; Yu, X.; Qiu, H.; Yap, G. P. A.; Guzei, I. A.; Lin, Z.; Wu, Y. D.; Xue, Z.-L. *J. Am. Chem. Soc.* **2007**, *129*, 14408. (p) Chen, S.-J.; Zhang, J.; Yu, X.; Bu, X.; Chen, X.-T.; Xue, Z.-L. *Inorg. Chem.* **2010**, *49*, 4017. (q) Morton, L. A.; Miao, M.; Callaway, T. M.; Chen, T.; Chen, S.-J.; Tuinman, A. A.; Yu, X.-H.; Lu, Z.; Xue, Z.-L. *Chem. Commun.* **2013**, *49*, 9555. (r) Chen, T.-N.; Zhang, X.-H.; Wang, C.-S.; Chen, S.-J.; Wu, Z.-Z.; Li, L.-T.; Sorasaenee, K. R.; Diminnie, J. B.; Pan, H.-J.; Guzei, I. A.; Rheingold, A. L,; Wu, Y.-D.; Xue, Z.-L. *Organometallics* **2005**, *24*, 1214. (s) Qiu, H.; Chen, S.-J.;

Wang, C.-S.; Wu, Y.-D.; Guzei, I. A.; Chen, X.-T.; Xue, Z.-L. *Inorg. Chem.* **2009**, *48*, 3073. (t) Yu, X.; Chen, X.-T.; Xue, Z.-L. *Organometallics* **2009**, *28*, 6642. (u) Chen, S.-J.; Yap, G. P. A.; Xue, Z.-L. *Sci. China: Chem.* **2009**, *52*, 1583. (v) Chen, S.-J.; Zhang, X.-H.; Lin, Z.; Wu, Y.-D.; Xue, Z.-L. *Sci. China: Chem.* **2009**, *52*, 1723. (w) Chen, S.-J.; Xue, Z.-L. *Organometallics* **2010**, *29*, 5579. (x) Sharma, B.; Callaway, T. M.; Lamb, A. C.; Steren, C. A.; Chen, S.-J.; Xue, Z,-L. *Inorg. Chem.* **2013**, *52*, 11409. (y) Lamb, A. C.; Lu, Z.; Xue, Z.-L. *Chem. Commun.* **2014**, *50*, 10517.

26. Bradley, D. C.; Hursthouse, M. B.; Abdul Malik, K. M.; Vuru, G. B. C. Inorg. Chim. Acta **1980**, *44*, L5.
27. Benkeser, R. A.; Snyder, D. C. *J. Org. Chem.* **1982**, *47*, 1243.
28. Bruker (2003). SAINT-PLUS, Version 6.02 (including XPREP). Bruker AXS Inc., Madison, Wisconsin, USA.
29. Sheldrick, G. M. (2003). SADABS. University of Göttingen, Germany.
30. Rong, Y.; Al-Harbi, A.; Parkin, G. *Organometallics* **2012**, *31*, 8208.
31. Gibson, V. C.; Redshaw, C.; Walker, G. L. P.; Howard, J. A. K.; Hoy, V. J.; Cole, J. M.; Kuzming, L. G.; De Silva, D. S. *J. Chem. Soc., Dalton Trans.* **1999**, 161.
32. Kim, S.-J.; Jung, I. N.; Yoo, B. R.; Cho, S.; Ko, J.; Kim, S. H.; Kang, S.O. *Organometallics* **2001**, *20*, 1501.

Part 5

Syntheses and Characterization of Tantalum Amide and Imide Complexes

Abstract

New mixed amide imide species $Ta(NR_2)_2(=NSiMe_3)[N(SiMe_3)_2]$ (R = Me, **12**; Et, **13**) have been prepared by two different salt metathesis reactions from $TaCl_3[N(SiMe_3)_2]_2$ (**7**) or $\{Ta(\mu\text{-}Cl)Cl(=NSiMe_3)[N(SiMe_3)_2]\}_2$ (**8**). An intermediate in the reaction involving **7** eliminates $Me_3Si\text{-}NR_2$ (R = Me or Et), converting the amide $N(SiMe_3)_2$ ligand to the imide $=NSiMe_3$ ligand. Such intramolecular imidations are rare.

5.1. Introduction

Tantalum imide complexes have been used as precursors for Ta_2O_5[1] and TaN[2] thin films in chemical vapor deposition (CVD) and atomic layer deposition (ALD) processes. Typically, imide ligands are formed through intermolecular imidation.[3] Intramolecular imidation usually occurs through 1,2-elimination of Me_3SiCl or interligand transfer to an oxo ligand as shown in Scheme 5.1.[4,5]

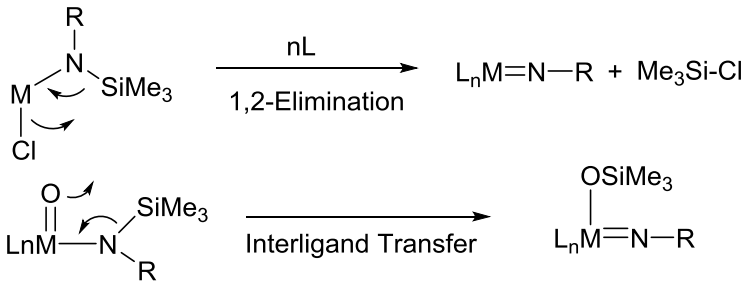

Scheme 5.1. Main types of intramolecular imidaiton.[4,5]

A new type of intramolecular imidation by "α-Si abstraction" was reported by Herrmann and Baratta, who prepared the first known ansa-type Group V complexes in the reaction of $M(NMe_2)_5$ with $[(\eta^5\text{-}C_5H_4)\text{-}Si(CH_3)_2\text{-}(HNC_6H_5)]$.[6] The Si-N bond is cleaved with the help of visible light irradiation to form an imide complex (Scheme 5.2). The isomerization is due to steric crowding between the π-cyclopentadienyl and the four amide ligands.

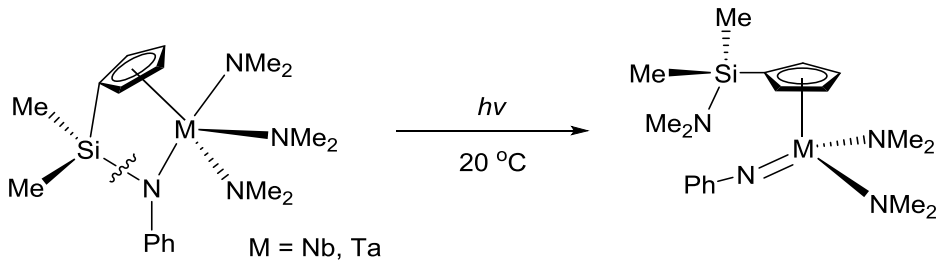

Scheme 5.2. Formation of Ta and Nb imide complexes via photochemical cleavage of Si-N bond.[6]

Our group recently reported the penta-amide $Ta(NMe_2)_4[N(SiMe_3)_2]$, which is unstable at room temperature. Upon heating, this complex undergoes elimination of $Me_3Si\text{-}NMe_2$ to form the imide dimer $[Ta(NMe_2)_3(\mu\text{-}NSiMe_3)]_2$ (Scheme 5.3).[7] This is second case of an "α-Si abstraction" in an amide ligand by another amide ligand to form an imide. Kinetics of the α-$SiMe_3$ abstraction showed that the disappearance of the mixed amide follows first-order kinetics.

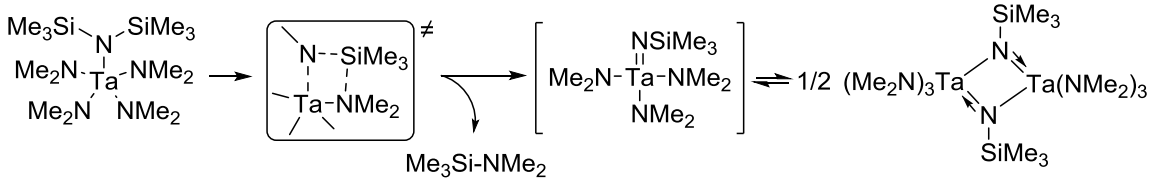

Scheme 5.3. The abstraction of an α-$SiMe_3$ group by an amide ligand which forms an imide "$Ta(NMe_2)_3(=NSiMe_3)$".[7]

Our group has also reported the formation of a four-membered metallaheterocyclic ring, $(Me_2N)_3\overline{Ta(\eta^2\text{-}N(SiMe_3)SiMe_2CH_2)}$, through a γ-hydrogen abstraction in the reaction of the mixed-amido complex $Ta(NMe_2)_3Cl[N(SiMe_3)_2]$ with one equiv. of $LiN(SiMe_3)_2$ (Scheme 5.4).[8] The X-ray crystal structure of $Ta(NMe_2)_3Cl[N(SiMe_3)_2]$ reveals that the compound adopts a distorted trigonal bipyramidal geometry in the solid with the $–N(SiMe_3)_2$ ligand in the equatorial plane and the Cl in the axial position.

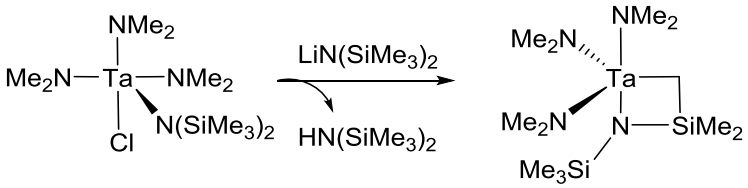

Figure 5.4. The formation of a four-membered metallaheterocyclic ring through γ-hydrogen abstraction.[8]

Herein we report the syntheses and characterization of $Ta(NR_2)_2(=NSiMe_3)[N(SiMe_3)_2]$ (R = Me, **12**; Et, **13**), which have been prepared by two methods. The mixed amide imide complexes **12** and **13** were first prepared from the reaction of $\{Ta(\mu\text{-}Cl)Cl(=NSiMe_3)[N(SiMe_3)_2]\}_2$ (**8**) with the corresponding lithium amide. In an attempt to form the previously mentioned $(Me_2N)_3\overline{Ta(\eta^2\text{-}N(SiMe_3)SiMe_2CH_2)}$,[8] $Ta(NMe_2)_2(=NSiMe_3)[N(SiMe_3)_2]$ **(12)** along with $Me_3Si\text{-}NMe_2$ were obtained from the reaction of $TaCl_3[NSiMe_3)_2]_2$ with three equiv. of $LiNMe_2$.

5.2. Experimental Section

All manipulations were performed under a dry nitrogen atmosphere with the use of either a drybox or standard Schlenk techniques. All solvents such as diethyl ether, THF, hexanes, toluene, and pentane were dried over potassium/benzophenone, distilled, and stored under nitrogen. $TaCl_5$ (Strem), $LiN(SiMe_3)_2$ (Aldrich), and $LiNMe_2$ (Aldrich) were used as received. $TaCl_3[N(SiMe_3)_2]_2$ (**7**) and $\{Ta(\mu\text{-}Cl)Cl(=NSiMe_3)[N(SiMe_3)_2]\}_2$ (**8**) were prepared by the literature methods.[9,10] $LiNEt_2$ was obtained by addition of Bu^nLi to a hexanes solution of diethylamine and then removal of volatiles. NMR spectra were recorded on a Varian 500 MHz Fourier transform spectrometer unless otherwise noted, and were referenced to solvents. Mass spectra were recorded on a JEOL AccuTOF™ DART Mass Spectrometer. Elemental analyses were conducted via Complete Analysis Laboratories, Inc., Parsippany, NJ.

5.2.1. Synthesis of $Ta(NMe_2)_2(=NSiMe_3)[N(SiMe_3)_2]$ (12)

*Preparation from $\{Ta(\mu\text{-}Cl)Cl(=NSiMe_3)[N(SiMe_3)_2]\}_2$ (**8**).* $LiNMe_2$ (261 mg, 5.12 mmol) in diethyl ether (30 mL) was added to **8** (1.20 g, 1.20 mmol) in diethyl ether (30 mL) with stirring at -30 °C. The mixture was allowed to stir for 18 h. Diethyl ether was then removed in vacuo and the residue was dissolved in pentane. The solution was then filtered and the volatiles were removed in vacuo to give **12** as a yellow liquid (1.00 g, 1.94 mmol, 81% yield).

*Preparation from $TaCl_3[N(SiMe_3)_2]_2$ (**7**)*. Solid $LiNMe_2$ (128 mg, 2.51 mmol) was added slowly to **7** (475 mg, 0.78 mmol) in toluene (60 mL) with stirring at -30 °C. The mixture was allowed to stir overnight. Toluene was then removed in vacuo and the residue

was dissolved in pentane. The solution was then filtered and the volatiles were removed in vacuo to give **12** as a yellow liquid (284 mg, 0.55 mmol, 71%). ^{1}H NMR (benzene-d_6, 499.7 MHz, 23 °C) 3.13 (s, 12H, NMe_2), 0.31 [s, 18H, N(SiMe_3)$_2$], 0.31 (s, 9H, =NSiMe_3). ^{13}C NMR (benzene-d_6, 62.5 MHz, 23 °C) δ 47.20 (NMe_2), 5.58 [N(SiMe_3)$_2$], 3.94 (=NSiMe_3). Anal. Calcd for $C_{13}H_{39}N_4Si_3Ta$: C, 30.22; H, 7.61. Found: C, 30.13; H, 7.51.

5.2.2. Synthesis of Ta(NEt$_2$)$_2$(=NSiMe$_3$)[N(SiMe$_3$)$_2$] (13)

*Preparation from {Ta(μ-Cl)Cl(=NSiMe$_3$)[N(SiMe$_3$)$_2$]}$_2$ (**8**).* LiNEt$_2$ (380 mg, 4.81 mmol) in diethyl ether (30 mL) was added dropwise to **8** (1164 mg, 1.17 mmol) in diethyl ether (30 mL) with stirring at -30 °C. The mixture was allowed to stir for 18 h. Diethyl ether was then removed and the residue was dissolved in pentane. The solution was then filtered and the volatiles were removed in vacuo to give **13** as a brown liquid (1.20 g, 2.10 mmol, 90% yield).

*Preparation from TaCl$_3$[N(SiMe$_3$)$_2$]$_2$ (**7**)*. Solid LiNEt$_2$ (212 mg, 2.68 mmol) was added slowly to **7** (510 mg, 0.84 mmol) in diethyl ether (30 mL) with stirring at -30 °C. The mixture was allowed to stir overnight. Diethyl ether was then removed and the residue was dissolved in pentane. The solution was then filtered and the volatiles were removed in vacuo to give **13** as a brown liquid (229 mg, 0.4 mmol, 69% yield). ^{1}H NMR (benzene-d_6, 499.7 MHz, 23 °C) δ 3.49-3.36 (m, 8H, N-CH_2-Me), 1.09 (t, 12H, N-CH$_2$-Me), 0.38 [s, 18H, N(SiMe_3)$_2$], 0.32 (s, 9H, =NSiMe_3). ^{13}C NMR (benzene-d_6, 125 MHz, 23 °C) δ 48.25 (N-CH$_2$-Me), 16.44 (N-CH$_2$-Me), 5.64 [N(SiMe_3)$_2$], 3.69 (=NSiMe_3).

5.3. Results and Discussion

5.3.1. Preparation and Characterization of $Ta(NMe_2)_2(=NSiMe_3)[N(SiMe_3)_2]$ (12)

$Ta(NMe_2)_2(=NSiMe_3)[N(SiMe_3)_2]$ (**12**) was prepared and characterized by ^1H and ^{13}C NMR, elemental analysis and mass spectrometry (MS). Four equiv. of $LiNMe_2$ in diethyl ether was added dropwise to a solution of $\{Ta(\mu\text{-}Cl)Cl(=NSiMe_3)[N(SiMe_3)_2]\}_2$ (**8**) in diethyl ether at -30 °C with continuous stirring (Scheme 5.5). The solution was filtered and upon removal of volatiles in vacuo, a yellow viscous liquid product, **12**, was obtained. NMR characterization showed that the product, without further purification, was pure, and it passed the elemental analysis.

An alternate route for the preparation of $Ta(NMe_2)_2(=NSiMe_3)[N(SiMe_3)_2]$ (**12**) was the addition of four equiv. of solid $LiNMe_2$ to a stirring THF/pentane solution of $\{Ta(\mu\text{-}Cl)Cl(=NSiMe_3)[N(SiMe_3)_2]\}_2$ (**8**) at 23 °C. The volatiles were removed and the crude product was dissolved in pentane. After filtration, pentane was removed under vacuum to give **12**. In addition, $Ta(NMe_2)_2(=NSiMe_3)[N(SiMe_3)_2]$ (**12**) was also prepared from $TaCl_3[N(SiMe_3)_2]_2$ (**7**) and three equiv. of $LiNMe_2$ by both methods listed above.

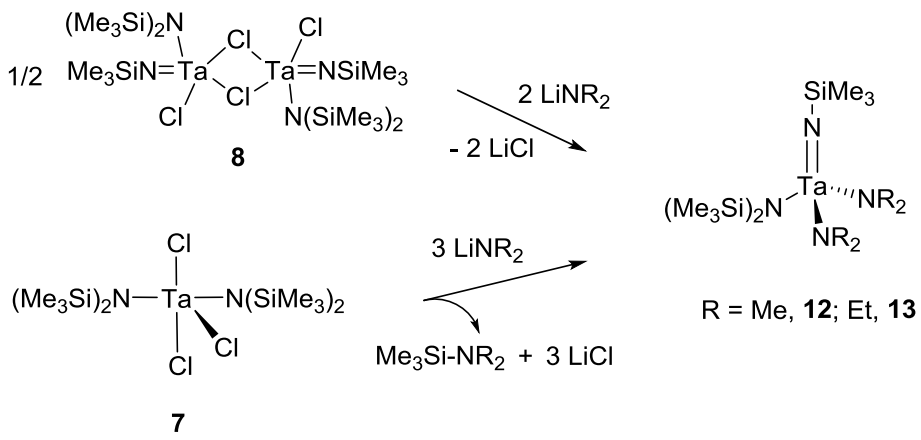

Scheme 5.5. Preparation of **12** and **13**.

The ^{1}H NMR spectrum of **12** in benzene-d_6 (Figure 5.1) showed a singlet at 3.13 ppm for the amide NMe_2 ligands. The singlet for the silyl imide $=NSiMe_3$ and the silyl amide $N(SiMe_3)_2$ overlap at 0.31 ppm. In the ^{13}C NMR spectrum of **12** in benzene-d_6 (Figure 5.2), the N*Me*$_2$ group appears at 47.20 ppm. The methyl group on the silyl amide ligand appears at 5.58 ppm. The methyl group of the silyl imide was observed at 3.94 ppm.

Compound **12** was characterized by MS at *m*/*z* = 517.20 [**12**+H^+]. Due to the isotopes of the elements that make up **12**, it is expected to have a unique MS pattern. A liquid sample of **12** was placed in a heated He stream by the sealed end of a capillary tube. The MS spectrum of **12** is given in Figure 5.3 along with the predicted spectrum. It confirmed the identity of **12**.

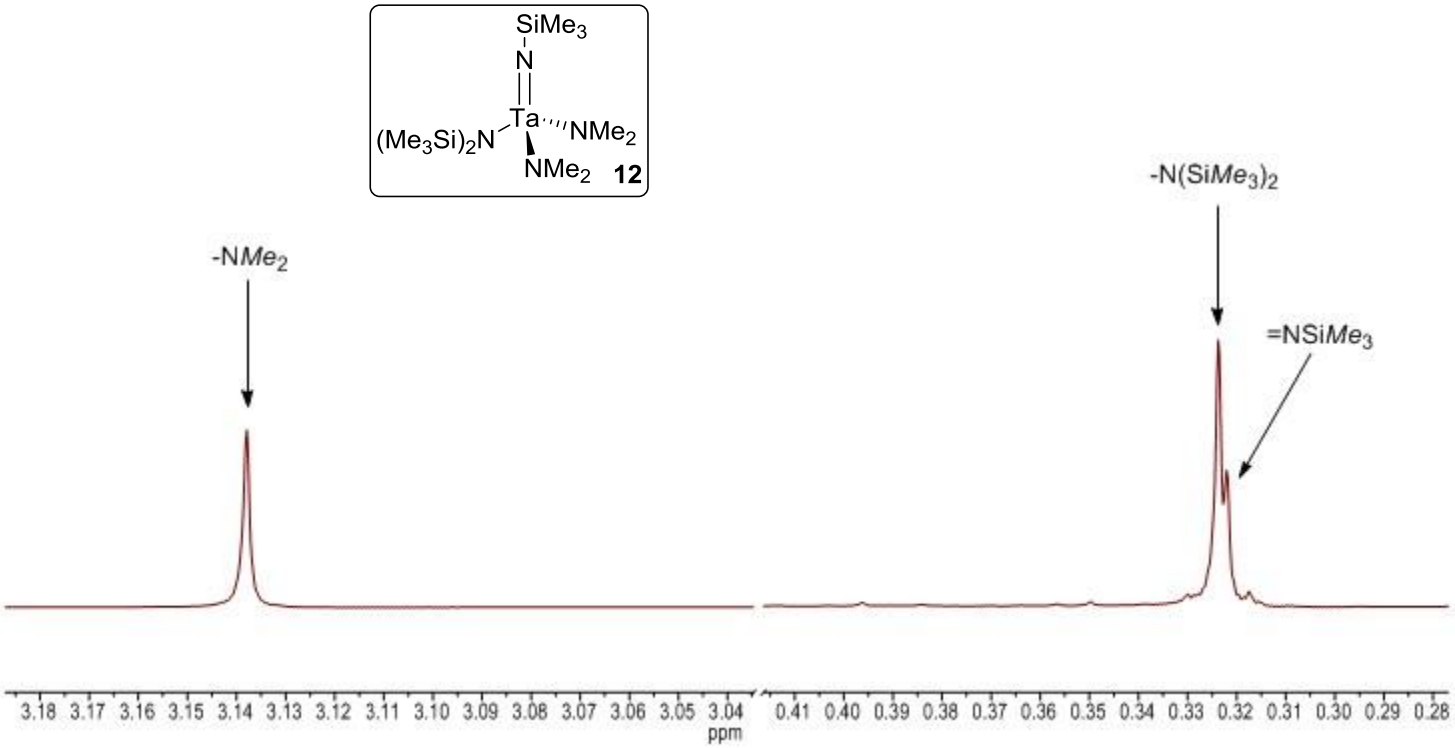

Figure 5.1. ^{1}H NMR spectrum of **12** in benzene-d_6 at 23 °C.

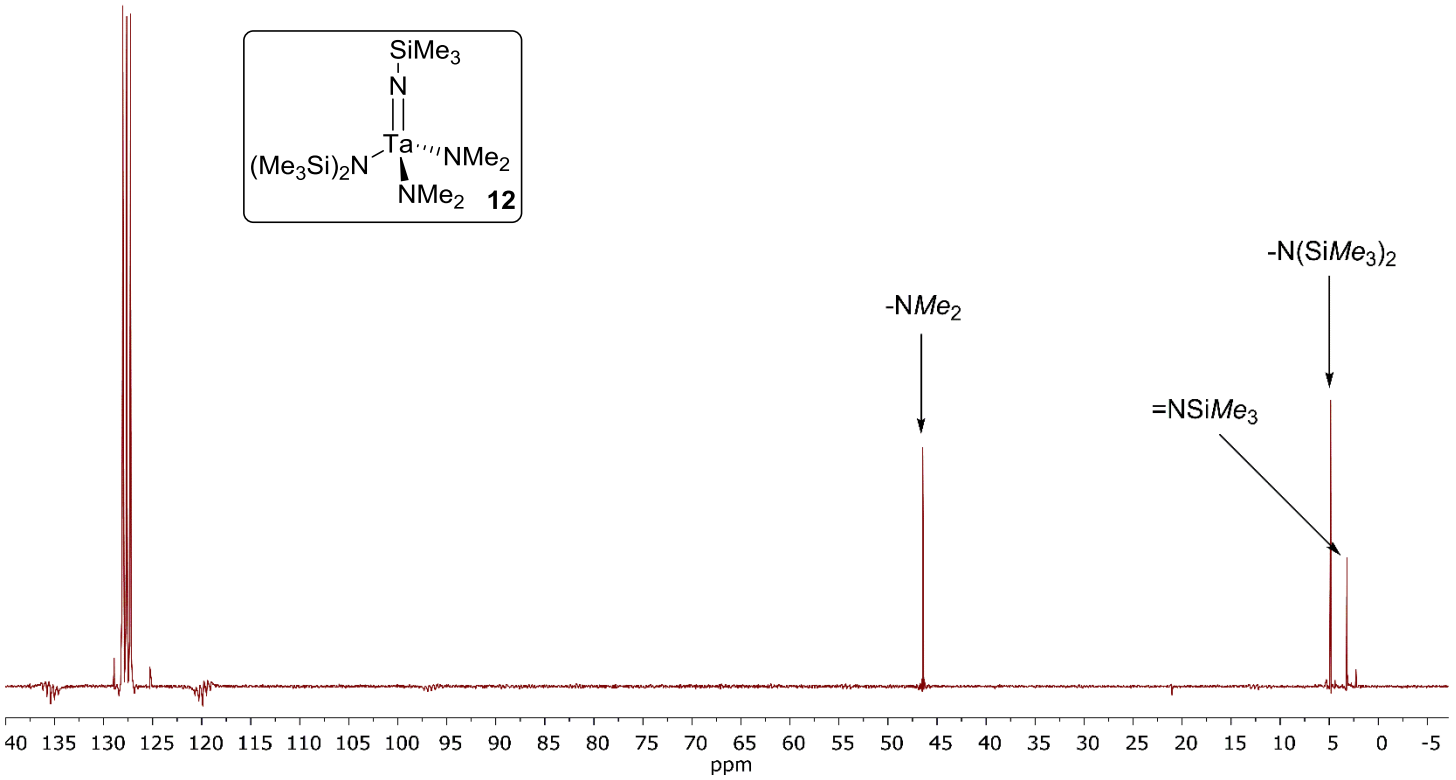

Figure 5.2. ^{13}C NMR spectrum of **12** in benzene-d_6 at 23 °C.

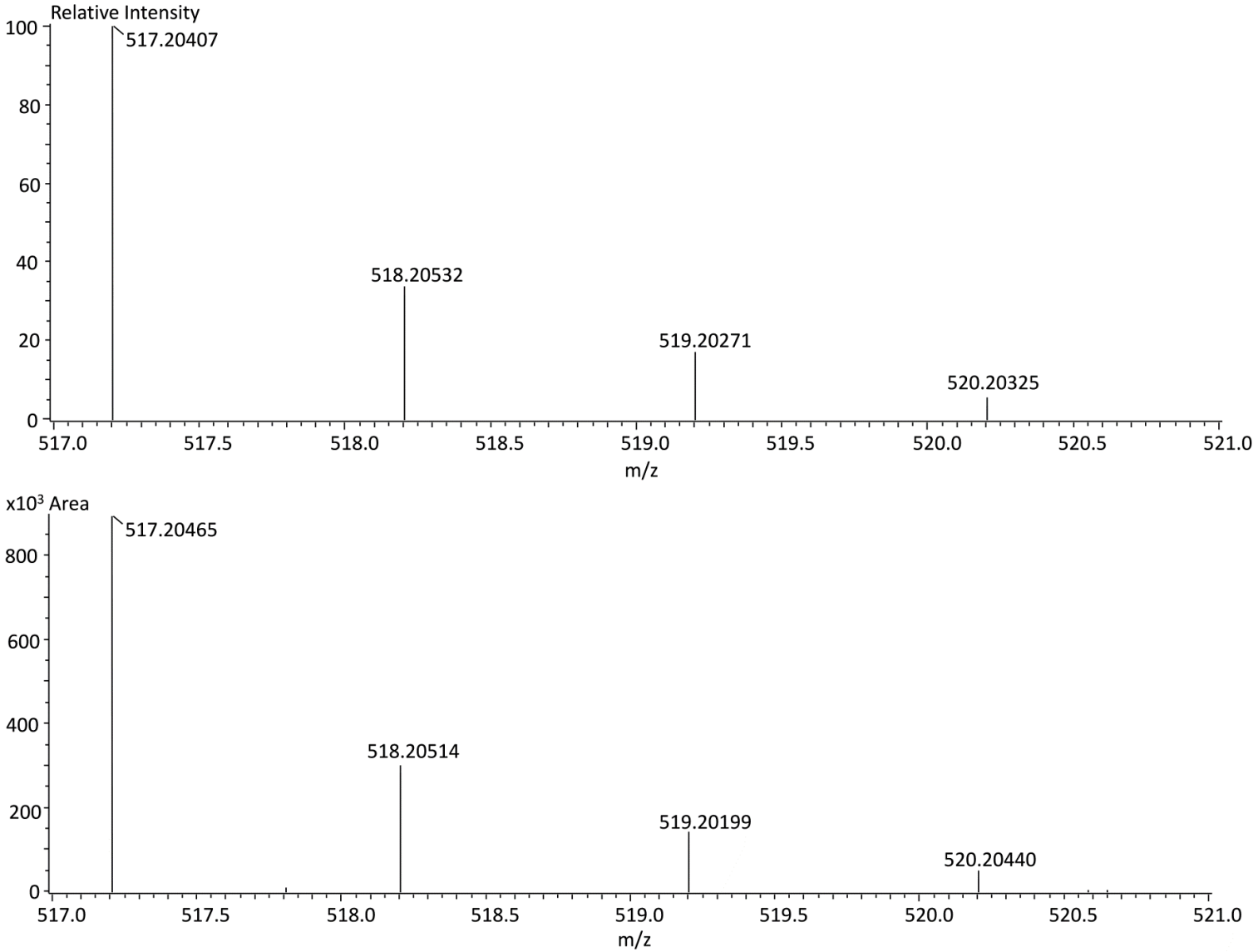

Figure 5.3. (Top) Calculated and (Bottom) Observed MS for [**12**+H^+].

5.3.2. Preparation and Characterization of $Ta(NEt_2)_2(=NSiMe_3)[N(SiMe_3)_2]$ (13)

$Ta(NEt_2)_2(=NSiMe_3)[N(SiMe_3)_2]$ (**13**) was prepared and characterized by ^1H and ^{13}C NMR spectroscopies and mass spectrometry. Four equiv. of $LiNEt_2$ in diethyl ether were added dropwise to a solution of $\{Ta(\mu\text{-}Cl)Cl(=NSiMe_3)[N(SiMe_3)_2]\}_2$ (**8**) in diethyl ether at -40 °C with continuous stirring. The solution was filtered and upon removal of volatiles in vacuo, a brown viscous liquid product, **13**, was obtained. NMR and MS characterization revealed the presence of $HN(SiMe_3)_2$ along with **13**.

The ^1H NMR spectrum of **13** in benzene-d_6 (Figure 5.4) showed a singlet at 0.38 ppm for the silyl amide $N(SiMe_3)_2$. Another singlet at 0.32 ppm is found for silyl imide $=NSiMe_3$. The $-CH_2-$ moieties of the diethyl amide NEt_2 are diastereotopic and show as a multiplet at 3.49-3.36 ppm. The methyl moieties of the ethyl amide ligands are nearly a triplet at 1.09 ppm. In the ^{13}C NMR spectrum of **13** in benzene-d_6 (Figure 5.5), the $-CH_2-$ group of the NEt_2 ligand appears at 16.44 ppm. The CH_3 group of the NEt_2 ligand appear at 48.25 ppm. The methyl groups on the silyl amide ligand appear at 5.64 ppm. The methyl groups of the silyl imide were observed at 3.69 ppm.

Compound **13** was characterized by MS at m/z = 573.27 [**13**+H^+]. Due to the isotopes of the elements that make up **13**, it is expected to have a unique MS pattern. A liquid sample of **13** was placed in a heated He stream by the sealed end of a capillary tube. The MS spectrum of **13** is given in Figure 5.6 along with the predicted spectrum. It confirmed the identity of **13**.

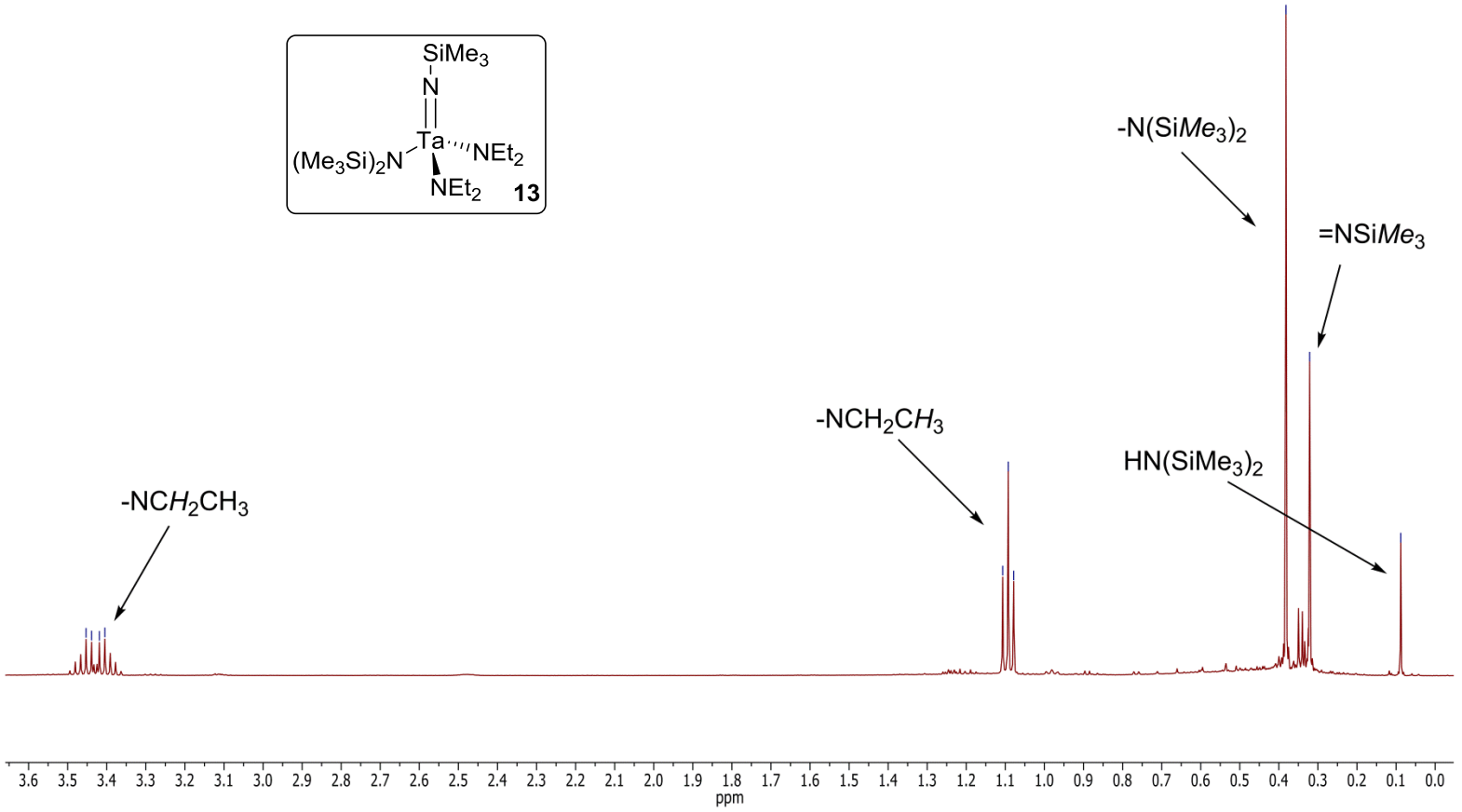

Figure 5.4. ^{1}H NMR spectrum of **13** in benzene-d_6 at 23 °C.

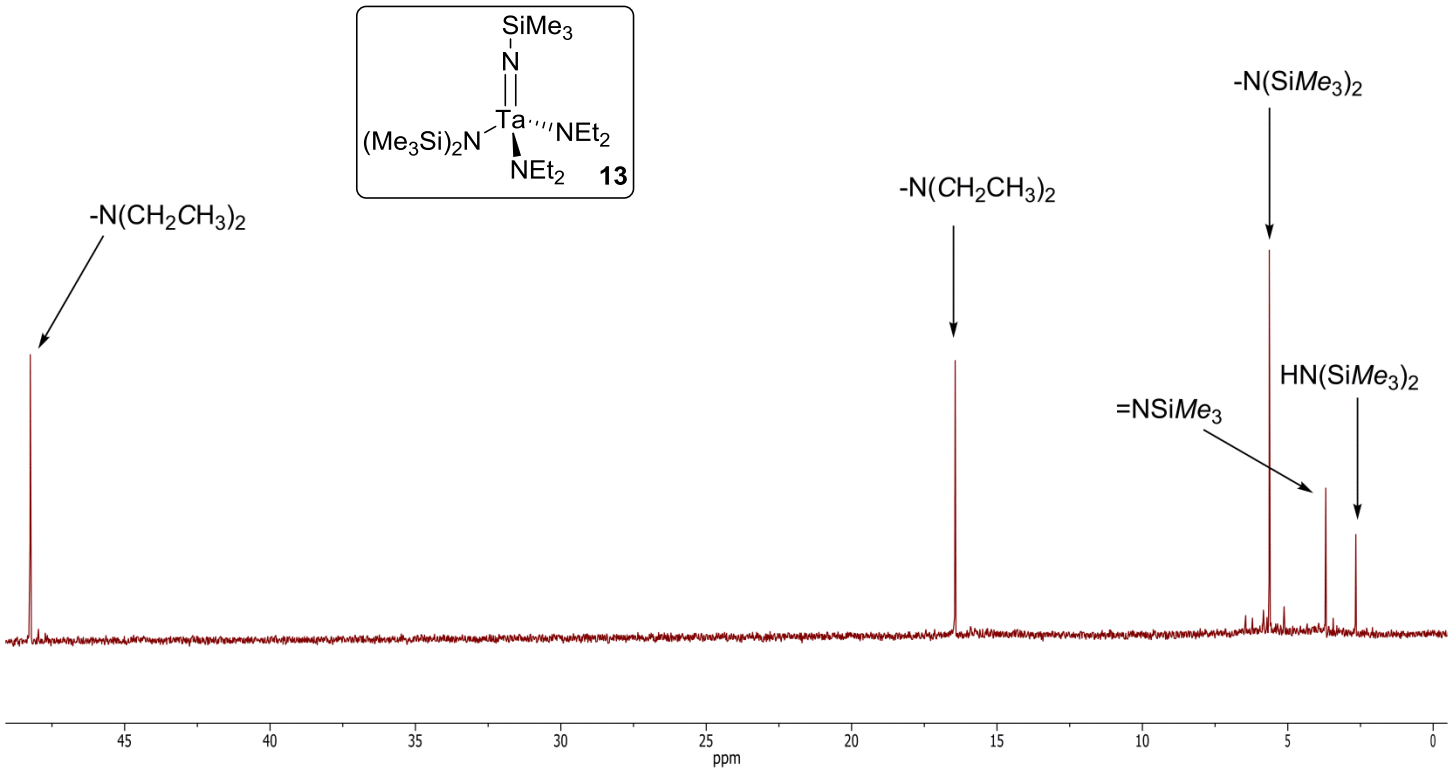

Figure 5.5. ^{13}C NMR spectrum of **13** in benzene-d_6 at 23 °C.

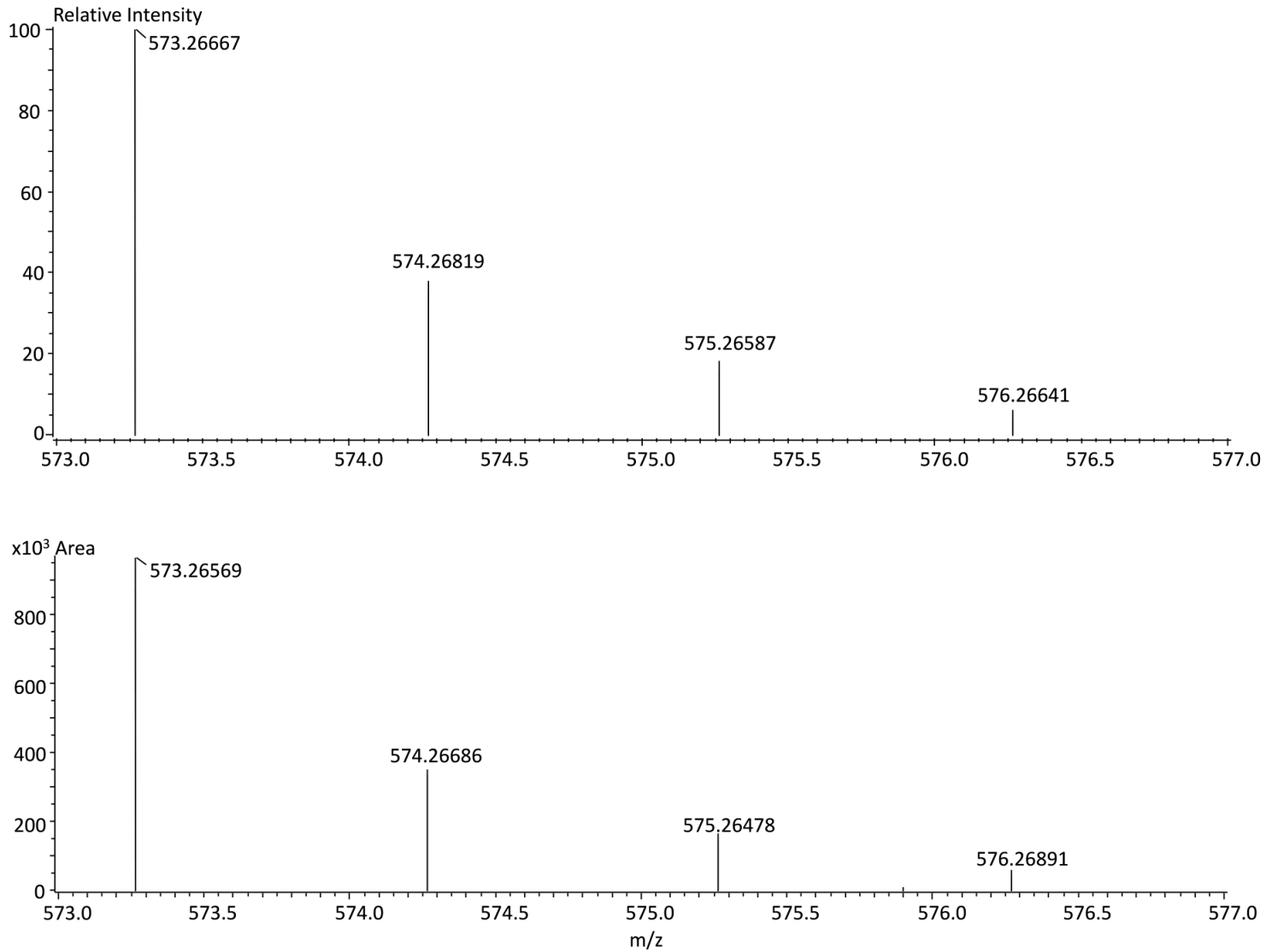

Figure 5.6. (Top) Calculated and (Bottom) Observed MS for [**13**+H^+].

5.3.3. Intramolecular Imidation

12 and **13** were also prepared from the reactions of $TaCl_3[N(SiMe_3)_2]_2$ (**7**) with three equiv. of $LiNR_2$ (R = Me, Et) at -30 °C. The solutions were filtered and upon removal of solvent in vacuo, liquids **12** and **13** were obtained (Scheme 5.5) along with $Me_3Si\text{-}NR_2$ (R = Me, Et) which were confirmed by ^1H NMR spectroscopy and GC-MS. Typically, intermolecular imidation is more common for the formation of imide ligands.[3] For intramolecular imidation the two main types is 1,2-elimination of Me_3SiCl or interligand transfer.[4,5] The reaction here is the third known case of abstraction of an α-$SiMe_3$ group by an amide ligand.[6,7] Our previously reported case in which $Ta(NMe_2)_4[N(SiMe_3)_2]$ undergoes intramolecular imidation by α-$SiMe_3$ abstraction by an amide ligand to form $[Ta(NMe_2)_3(\mu\text{-}NSiMe_3)]_2$, the reaction takes a week. In comparison, the reaction described here is nearly instantaneous.

Our group has previously shown that $Ta(NMe_2)_3[N(SiMe_3)_2]_2$ undergoes γ-hydrogen abstraction to form $(Me_2N)_3Ta(\eta^2\text{-}N(SiMe_3)SiMe_2CH_2)$.[8] The synthesis of $Ta(NR_2)Cl_2[N(SiMe_3)_2]_2$ (R = Me, Et) from **7** was attempted to see if they are stable. In the reaction between **7** and one equiv. of $LiNR_2$ (R = Me, Et), we found the formation of a mixture of **12** or **13**, along with unreacted **7**, suggesting that the intermediate $Ta(NR_2)Cl_2[N(SiMe_3)_2]_2$ is unstable.

5.4. Concluding Remarks

$Ta(NR_2)_2(=NSiMe_3)[N(SiMe_3)_2]$ (R = Me, **12**; Et, **13**) have been synthesized from two different reactions. **12** was characterized by ^1H and ^{13}C NMR spectroscopies, elemental analysis, and MS. **13** was characterized by ^1H and ^{13}C NMR spectroscopies

and MS. The pathway from the reaction of **7** eliminates $Me_3Si\text{-}NR_2$ (R = Me or Et), converting the amide $N(SiMe_3)_2$ ligand to the imide $=NSiMe_3$ ligand.

References

1. (a) Son, K.-A.; Mao, A. Y.; Sun, Y.-M.; Kim, B. Y.; Liu, F.; Kamath, A.; White, J. M.; Kwong, D. L.; Roberts, D. A.; Vrtis, R. N. *Appl. Phys. Lett.* **1998**, *72*, 1187. (b) Niimi, H.; Johnson, R. S.; Lucovsky, G.; Massoud, H. Z. *Proc. Electrochem. Soc.* **2000**, *2000-2*, 487. (c) Rodriguez-Reyes, J. C. F.; Teplyakov, A. V. *J. Appl. Phys.* **2008**, *104*, 084907/1. (d) Hausmann, D. M.; de Rouffignac, P.; Smith, A.; Gordon, R.; Monsma, D. *Thin Solid Films* **2003**, *443*, 1. (e) Chiu, H.-T.; Wang, C.-N.; Chuang, S.-H. *Chem. Vap. Deposition* **2000**, *6*, 223. (f) Wiedmann, M. K.; Heeg, M. J.; Winter, C. H. *Inorg. Chem.* **2009**, *48*, 5382. (g) Dezelah, C. L., IV; Wiedmann, M. K.; Mizohata, K.; Baird, R. J.; Niinistoe, L.; Winter, C. H. *J. Am. Chem. Soc.* **2007**, *129*, 12370.
2. (a) Fix, R.; Gordon, R. G.; Hoffman, D. M. *Chem. Mater.* **1993**, *5*, 614. (b) Juppo, M.; Ritala, M.; Leskelä, M. *J. Electrochem. Soc.* **2000**, *147*, 3377. (c) Leng, Y. X.; Sun, H.; Yang, P.; Chen, J. Y.; Wang, J.; Wan, G. J.; Huang, N.; Tian, X. B.; Wang, L. P.; Chu, P. K. *Thin Soild Films* **2001**, *398-399*, 471. (d) Leskelä, M.; Ritala, M. *Angew. Chem. Int. Ed.* **2003**, *42*, 5548. (e) Aouadi, S. M.; Debessai, M. *J. Vac. Sci. Technol. A* **2004**, *22*, 1975. (f) Rayner Jr.; G. B.; George, S. M. *J. Vac. Sci. Technol. A* **2009**, *27*, 716. (g) Shen, L.; Wang, N. *J. Nanomater.* **2011**, 2011, article ID 781935. (h) Zhou, Y.; Jin, P.; Chen, S.; Zhu, Y. Mater. Lett. **2014**, *136*, 168.
3. (a) Berry, J. F. *Comments Inorg. Chem.* **2009**, *30*, 28. (b) Schrock, R. R. *Chem. Rev.* **2009**, *109*, 3211. (c) Zarubin, D.; Ustynyuk, N. *Russ. Chem. Rev.* **2006**, *75*, 671. (d) Eikey, R.; Abu-Omar, M. *Coord. Chem. Rev.* **2003**, *243*, 83. (e) Li, Y.; Wong, W. *Coord. Chem. Rev.* **2003**, *243*, 191. (f) Gade, L.; Mountford, P. *Coord.*

Chem. Rev. **2001**, *216−217*, 65. (g) Nugent, W. A.; Mayer, J. M. *Metal−Ligand Multiple Bonds*; Wiley-Interscience: New York, 1988. (h) Rosenfeld, D. C.; Wolczanski, P. T.; Barakat, K. A.; Buda, C.; Cundari, T. R.; Schroeder, F. C.; Lobkovsky, E. B. *Inorg. Chem.* **2007**, *46*, 9715. (i) Holland, P. L.; Andersen, R. A.; Bergman, R. G. *Organometallics* **1998**, *17*, 433. (j) Burland, M. C.; Pontz, T. W.; Meyer, T. Y. *Organometallics* **2002**, *21*, 1933. (k) Brown, S. D.; Peters, J. C. *J. Am. Chem. Soc.* **2004**, *126*, 4538. (l) Bailey, B. C.; Huffman, J. C.; Mindiola, D. J.; Weng, W.; Ozerov, O. V. *Organometallics* **2005**, *24*, 1390. (m) Kogut, E.; Wiencko, H. L.; Zhang, L.; Cordeau, D. E.; Warren, T. H. *J. Am. Chem. Soc.* **2005**, *127*, 11248. (n) Bart, S. C.; Lobkovsky, E.; Bill, E.; Chirik, P. J. *J. Am. Chem. Soc.* **2006**, *128*, 5302. (o) Ison, E. A.; Abboud, K. A.; Boncella, J. M. *Organometallics* **2006**, *25*, 1557. (p) Shaver, M. P.; Fryzuk, M. D. *J. Am. Chem. Soc.* **2005**, *127*, 500. (q) Sceats, E. L.; Figueroa, J. S.; Cummins, C. C.; Loening, N. M.; Van der Wel, P.; Griffin, R. G. *Polyhedron* **2004**, *23*, 2751. (r) Shay, D. T.; Yap, G. P. A.; Zakharov, L. N.; Rheingold, A. L.; Theopold, K. H. *Angew. Chem., Int. Ed.* **2005**, *44*, 1508.

4. (a) Chong, A. O.; Oshima, K.; Sharpless, K. B. *J. Am. Chem. Soc.* **1977**, *99*, 3420. (b) Maatta, E. A.; Haymore, B. L.; Wentworth, R. A. D. *Inorg. Chem.* **1980**, *19*, 1055. (c) Rossi, R.; Marchi, A.; Duatti, A.; Magon, L.; Bernado, P. *Transition Met. Chem.* **1985**, *10*, 151. (d) Burger, U.; Wannagat, U. *Monatsh. Chem.* **1963**, *94*, 761. (e) Burger, H.; Smrekar, O. *Monatsh. Chem.* **1964**, *95*, 292. (f) Nugent, W. A.; Harlo, R. L. *J. Chem. Soc., Chem. Commun.* **1978**, 579. (g) Jones, C. M.; Lerchen, M. E.; Church, C. J.; Schomber, B. M.; Doherty, N. M. *Inorg. Chem.* **1990**, *29*, 1679.

5. (a) Bradley, D. C.; Thomas, I. M. *Can. J. Chem.* **1962**, *40*, 1355. (b) Davies, H. O.; Jones, A. C.; McKinnell, E. A.; Raftery, J.; Muryn, C. A.; Afzaal, M.; O'Brien, P. *J. Mater. Chem.* **2006**, *16*, 2226. (c) Chen, S.-J.; Zhang, J.; Yu, X.; Bu, X.; Chen, X.-T.; Xue, Z.-L. *Inorg. Chem.* **2010**, *49*, 4017.
6. Herrmann, W. A.; Baratta, W. *J. Organomat. Chem.* **1996**, *506*, 357.
7. Sharma, B.; Chen, S.-J.; Abbott, J. K. C.; Chen, X.-T.; Xue, Z.-L. *Inorg. Chem.* **2012**, *51*, 25.
8. Cai, H.; Yu, X.; Chen, T.; Chen, X.-T.; You, X.-Z.; Xue, Z.-L. *Can. J. Chem.,* **2003**, *81*, 1398.
9. Bradley, D. C.; Hursthouse, M. B.; Howes, A. J.; Jelfs, A. N. D.; Runnacles, J. D.; Thorntonpett, M. *J. Chem. Soc.-Dalton Trans.* **1991**, 841.
10. Bradley, D. C.; Hursthouse, M. B.; Abdul Malik, K. M.; Vuru, G. B. C. Inorg. Chim. Acta **1980**, *44*, L5.

Part 6

Conclusion and Future Studies

This dissertation focused on two distinct projects: (1) Magnetic and structural properties of metalloporphyrins; (2) Synthesis and characterization of mixed tantalum amide imide complexes. Using inelastic neutron scattering (INS), we have been able to directly determine the zero field splitting (ZFS) parameters *D* for [M(TPP)Cl] (M = Cr, **3**; Mn, **2**; Fe, **1**; TPP^{2-} = *meso*-tetraphenylporphyrinate) and [Mn(TPP)] (**4**). It was also found that intermolecular interactions in the solid state of the biomimetic porphyrins **1** and [M(TPP)(NO)] (M = Fe, **5**; Co, **6**) cause the disorder and phase changes observed earlier in variable temperature studies. The amide imide alkyl complexes $TaMe_2(=NSiMe_3)[N(SiMe_3)_2]$ (**9**) and $Ta(CH_2Ph)_2(=NSiMe_3)[N(SiMe_3)_2]$ (**10**) have been synthesized by metathesis reactions. The reactions of **9** or **10** with O_2 were investigated. The methoxy dimer $Ta_2(\mu\text{-}OMe)_2(=NSiMe_3)_2[N(SiMe_3)_2]_2Me_2$ (***trans*-11**) was isolated and characterized by single-crystal X-ray diffraction. The novel mixed amide imide complexes $Ta(NR_2)_2(=NSiMe_3)[N(SiMe_3)_2]$ (R = Me, **12**; Et, **13**) were prepared from the reaction of $TaCl_3[N(SiMe_3)_2]_2$ (**7**) or $\{Ta(\mu\text{-}Cl)Cl(=NSiMe_3)[N(SiMe_3)_2]\}_2$ (**8**) and the appropriate lithium amide salt.

In Part 2, magnetic excitations of metalloporphyrins were probed for the first time by INS. Due to the small energy of these excitations, non-deuterated samples were used. A positive *D* value, 6.33(8) cm^{-1} for [Fe(TPP)Cl] (**1**) and 0.79(2) cm^{-1} for [Mn(TPP)] (**4**), were determined for the two *S* = 5/2 complexes. The direct determination of ZFS *D* parameter for **1** puts to rest often inaccurate measurements from other methods. Typical of Mn(III) *S* = 2 complexes, a negative *D*, -2.24(3) cm^{-1}, was determined for [Mn(TPP)Cl] (**2**). For [Cr(TPP)Cl] (**3**), $|D|$ = 0.234(12) cm^{-1}, which is due in part to the spherical nature of the unpaired *d* electrons in this *S* = 3/2 spin system.

In Part 3, a variable-temperature (VT) study of [Fe(TPP)Cl] (**1**) and a comparison to previously published VT studies on [M(TPP)(NO)] (M = Fe, **5**; Co, **6**) are presented. Hirshfeld analysis has been employed to showcase how conformational changes appear in the molecular structures, and to identify driving forces for such changes that are otherwise not obvious as a result of disorder or twinning. These analyses have revealed that the disorders in the crystal structures of **5** and **6** at room temperature and phase changes at lower temperatures are a result of intermolecular interactions in the solid state. The phase changes in **5** and **6**, accompanied by the phenyl tilting, lead to reduced intermolecular interactions by gradual movement of the phenyl groups into the open voids. The same occurs in **1** with no phase change. Hirshfeld surface analyses as a whole-of-molecule approach allows for an objective way to compare crystal structures of different crystal symmetries, but with similar molecular forces and interactions.

In Part 4, syntheses of $TaMe_2(=NSiMe_3)[N(SiMe_3)_2]$ (**9**) and $Ta(CH_2Ph)_2(=NSiMe_3)[N(SiMe_3)_2]$ (**10**) and their reactions with O_2 are reported. **9** has been characterized by ^1H and ^{13}C NMR spectroscopies and MS. **10** was characterized by ^1H and ^{13}C NMR spectroscopies, elemental analysis and single-crystal X-ray diffraction. The crystal structure of **10** reveals η^2 coordination to the Ta center by a phenyl ring on one of the benzyl ligands. In the reaction between **9** and ½ equivalence of O_2, oxygen inserts into only one methyl ligand in **9** to form the methoxy dimer $Ta_2(\mu\text{-}OMe)_2(=NSiMe_3)_2[N(SiMe_3)_2]_2Me_2$ (***trans*-11** and ***cis*-11**). ***Trans*-11** was characterized by ^1H and ^{13}C NMR spectroscopies, elemental analysis and single-crystal X-ray diffraction.

In Part 5, new mixed amide imide species $Ta(NR_2)_2(=NSiMe_3)[N(SiMe_3)_2]$ (R = Me, **12**; Et, **13**) have been synthesized from two different reactions. **12** was characterized by

^{1}H and ^{13}C NMR spectroscopies, elemental analysis, and MS. **13** was characterized by ^{1}H and ^{13}C NMR spectroscopies and MS. The reaction from **7** eliminates $Me_3Si\text{-}NR_2$ (R = Me or Et), converting the amide $N(SiMe_3)_2$ ligand to the imide $=NSiMe_3$ ligand.

Future work for the magnetic studies project will focus on using INS to determine large zero-field splitting (ZFS) parameters. INS data were also obtained for the air-sensitive [Fe(TPP)] (**14**) complex shown in Figure 6.1. Previous magnetic structural studies of [Fe(TPP)] (**14**) shows that it has an intermediate spin, S = 1, with a relatively large D parameter, 65 cm^{-1}.[1] A challenge in using INS to determine large D splittings is that above ~30 cm^{-1}, the phonon region begins and it becomes difficult to differentiate between magnetic and phonon peaks, as shown in Figure 6.1. There are a few options that can be performed to attempt to discern which peaks are magnetic: (a) A magnet could be used to split the magnetic peak, and this separation between the peaks is relative to the strength of the magnetic field, or (b) Use a second sample that is isomorphous with the complex, but non-magnetic. The phonon peaks of the two samples should be similar. Subtraction of the INS spectrum of the non-magnetic control from the INS spectrum of the sample would yield the magnetic peaks. Neutrons have a spin s = 1/2 and can be polarized with either up or down spin. Polarized neutrons would interact with the magnetic peaks, changing their intensity, while not changing the intensity of the phonon/vibrational peaks. These experimental techniques, along with Q and temperature dependence, will be used to determine the ZFS parameters in the future.

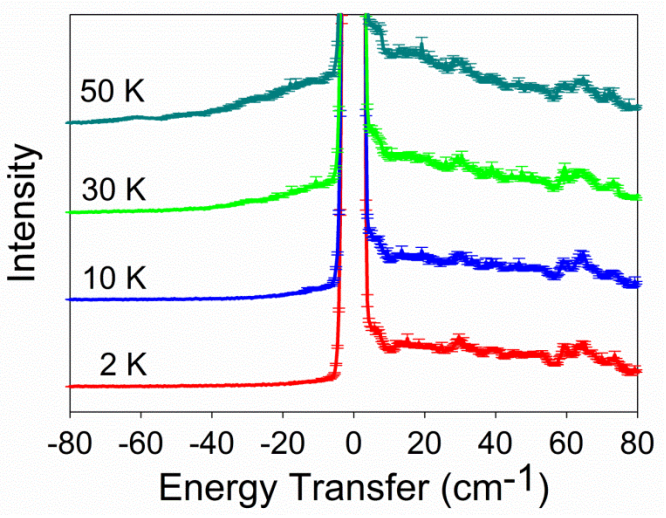

Figure 6.1. INS spectra of [Fe(TPP)] (**14**) using a 96.77 cm^{-1} incident neutron beam.

Future work on the d^0 tantalum imide complexes will focus on H_2O reactions with $TaMe_2(=NSiMe_3)[N(SiMe_3)_2]$ (**9**), $Ta(CH_2Ph)_2(=NSiMe_3)[N(SiMe_3)_2]$ (**10**) and $Ta(NR_2)_2(=NSiMe_3)[N(SiMe_3)_2]$ (R = Me, **12**; Et, **13**). Theoretical studies are underway to understand the mechanistic pathways for the imidation seen in the syntheses of **12** and **13**.

Reference

1. Boyd, P. D. W.; Buckingham, D. A.; McMeeking, R. F.; Mitra, S. *Inorg. Chem.* **1979**, *18*, 3585.

Appendices

Appendix A

Appendix A.1

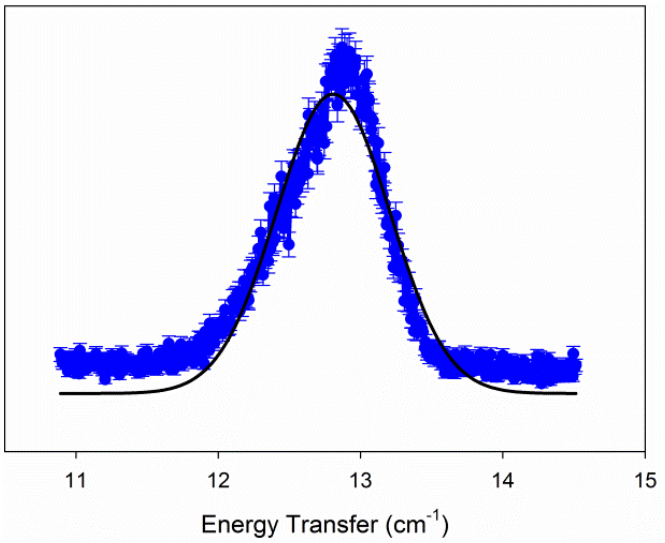

Area	3.72(3) x 10^{-3}
Center	12.7920(25)* cm^{-1}
FWHM	0.800(6) cm^{-1}
Background	4.09(6) x 10^{-4}

* Two significant digits for the error in "Center" are retained and will be rounded off in the calculation of the *D* value.

Figure A.1. Example of the INS peaks of [Fe(TPP)Cl] (**1**) used for the calibration of the elastic peak and calculation of the *D* value.

Error Analysis

(1) Incident neutron beam energies: 24.20 and 80.66 cm^{-1}; $|Q|$ range is 0.48-1.8 Δ^{-1}

(2) Step size in Figure S7: 0.008 cm^{-1}

(3) Usually the error associated with a peak position is of the order of the 10% of the linewidth (= 0.08 cm^{-1} in the current case), it is used here: $2D$ = 12.65(8) cm^{-1}; D = 6.33(8) cm^{-1}.

Appendix A.2

Area	12.2(8)
Center	2.3495(63)* cm^{-1}
FWHM	0.204(14) cm^{-1}
Background	11.1(6)
* Two significant digits for the error in "Center" are retained and will be rounded off in the calculation of the *D* value.	

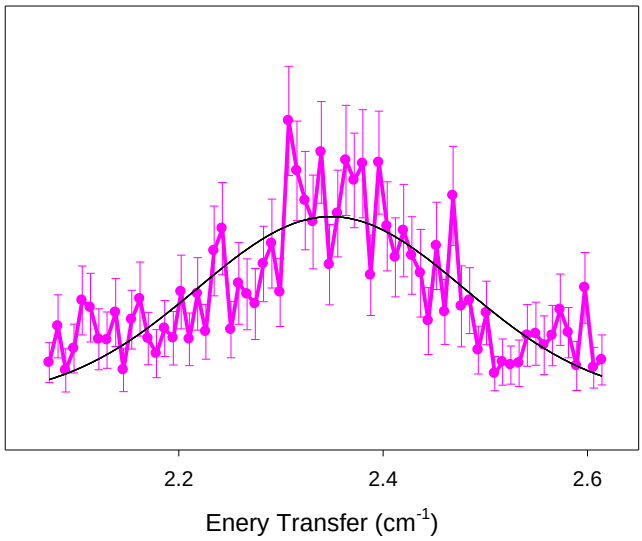

Figure A.2. Example of the INS peaks of [Mn(TPP)Cl] (**2**) used for the calibration of the elastic peak and calculation of the *D* value.

Error Analysis

(1) Incident neutron beam energies: 12.58 and 24.20 cm^{-1}; $|Q|$ range is 0.4-0.9 Δ^{-1}

(2) Step size in Figure S8: 0.008 cm^{-1}

(3) Using the peaks at -2.235 and 2.235 cm^{-1} (= *D*) which have the best resolutions,

Temperature (incident energy)	Energy transfer peak (cm^{-1})
50 K (12.58 cm^{-1})	2.2499
50 K (24.20 cm^{-1})	2.2200
Average	2.2350
σ_{n-1}	0.0149

$\sigma_{total}^2 = (0.008)^2 + (0.0149)^2$; σ_{total} = 0.017 cm^{-1}

(4) Since usually the error associated with a peak position is of the order of the 10% of the linewidth (= 0.02 cm^{-1} in the current case), and the error analysis above yields σ_{total} < 0.02 cm^{-1}, 0.02 cm^{-1} is used as the estimated error for the *D* value: *D* = -2.24(2) cm^{-1}.

Appendix A.3

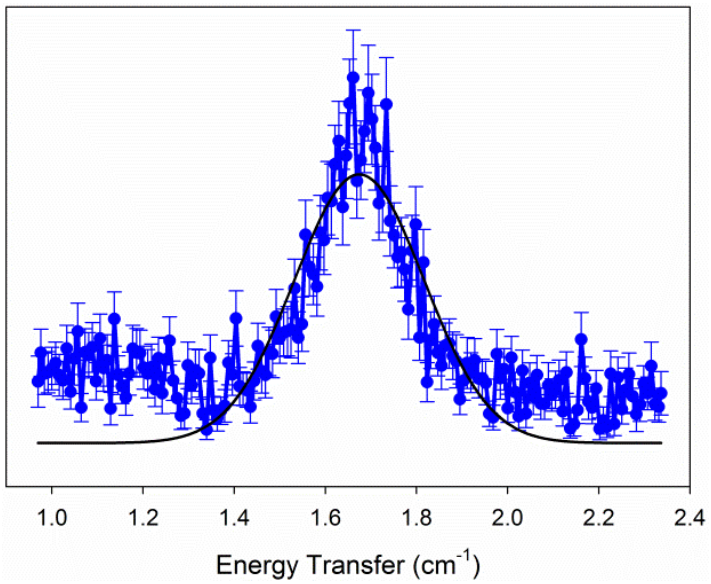

Area	25.1(9)
Center	1.6728(36)* cm^{-1}
FWHM	0.228(8) cm^{-1}
Background	17.3(7)

* Two significant digits for the error in "Center" are retained and will be rounded off in the calculation of the *D* value.

Figure A.3. Example of the INS peaks of [Mn(TPP)] (**4**) used for the calibration of the elastic peak and calculation of the *D* value.

Error Analysis

(1) Incident neutron beam energies: 12.58 cm^{-1}; $|Q|$ range is 0.4-1.2 Δ^{-1}

(2) Step size in Figure S9: 0.008 cm^{-1}

(3)

Temperature	Energy transfer peak (cm^{-1})
50 K	1.5667
10.2 K	1.5728
5.1 K	1.5700
2. 1 K	1.5692
Average	1.5697
σ_{n-1}	0.00249

$\sigma_{total}^2 = (0.008)^2 + (0.00249)^2$; $\sigma_{total} = 0.0084$ cm^{-1}

(4) Attempts were made to use the peaks at -3.14 and 3.14 cm^{-1} (4*D*) at 5.1, 10.2 and 50.0 K to calculate the *D* value. However, these peaks are weaker than those at -1.56 and 1.56 cm^{-1}, and Gaussian fits of the peaks were not successful. Thus the peaks at -3.14 and 3.14 cm^{-1} were not used further.

(5) Since usually the error associated with a peak position is of the order of the 10% of the linewidth (= 0.2 cm^{-1} in the current case), and the error analysis above yields $\sigma_{total} < 0.2$ cm^{-1}, 0.2 cm^{-1} is used as the estimated error for the 2*D* and *D* values. 2*D* = 1.57(2) cm^{-1}; *D* = 0.79(2) cm^{-1}

Appendix A.4

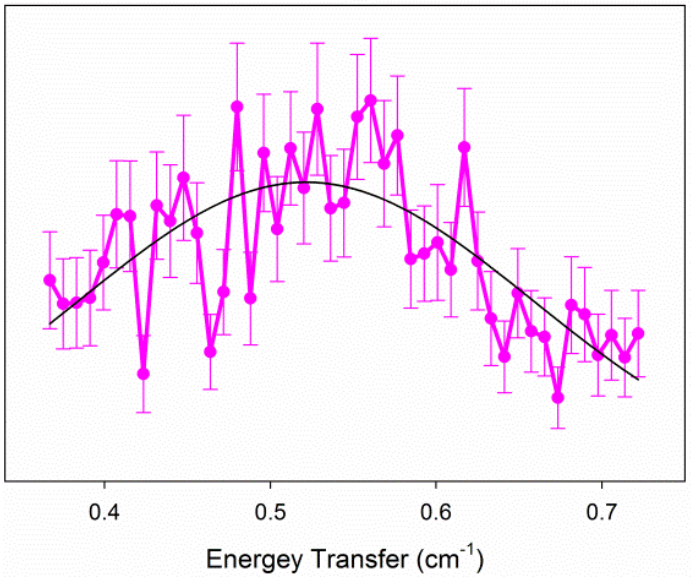

Area	1.8(4)
Center	0.4541(66)* cm^{-1}
FWHM	0.120(2) cm^{-1}
Background	1.1(1.1)

* Two significant digits for the error in "Center" are retained and will be rounded off in the calculation of the *D* value.

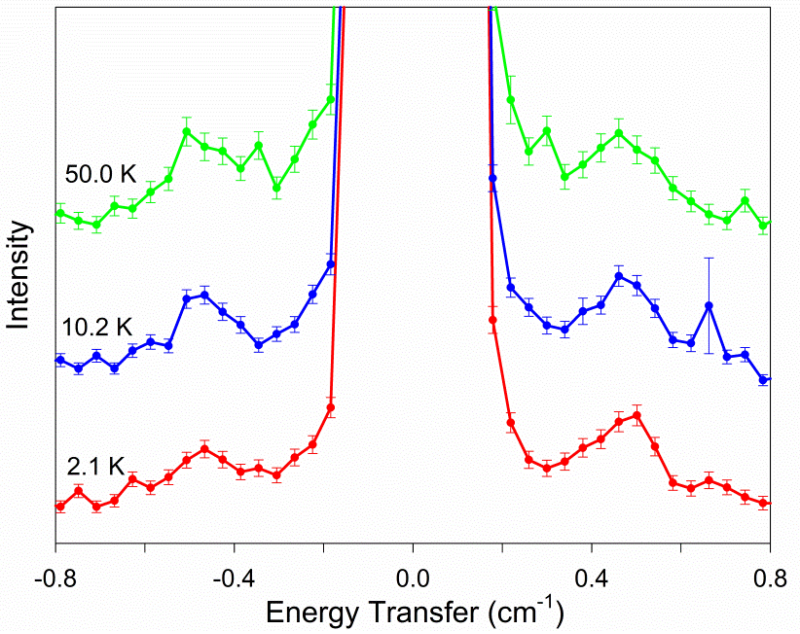

Figure A.4. (Top) Example of the INS peaks of [Cr(TPP)Cl] (**3**) used for the calibration of the elastic peak and calculation of the *D* value. (Bottom) Figure 2.9 is placed here for comparison of the peak resolutions.

Error Analysis

(1) Incident neutron beam energies: 8.06 cm^{-1}; $|Q|$ range is 0.5-1.0 Δ^{-1}

(2) Step size in Figure S10: 0.008 cm^{-1}

(3)

Temperature	Energy transfer peak (cm^{-1})
10 K	0.4695
2.1 K	0.4667
Average	0.4681
σ_{n-1}	0.0020246

$\sigma_{total}^2 = (0.008)^2 + (0.0020246)^2$; $\sigma_{total} = 0.008316$ cm^{-1}

(4) Since usually the error associated with a peak position is of the order of the 10% of the linewidth (= 0.012 cm^{-1} in the current case), and the error analysis above yields $\sigma_{total} < 0.012$ cm^{-1}, 0.012 cm^{-1} is used as the estimated error for the 2*D* and *D* values.

$2D = 0.468(12)$ cm^{-1}; $D = 0.234(12)$ cm^{-1}

Appendix B

Table B.1. Atomic coordinates (x 10^4) and equivalent isotropic displacement parameters (Å^2 x 10^3) for **10**. *U*(eq) is defined as one third of the trace of the orthogonalized U^{ij} tensor.

	x	*y*	*z*	*U*(eq)
C(13)	8812(11)	6910(5)	655(5)	33(2)
Ta(1)	8887(1)	6359(1)	2298(1)	21(1)
Si(2)	7703(3)	6800(2)	3943(2)	40(1)
Si(3)	10247(3)	5707(2)	3891(2)	35(1)
Si(1)	11673(3)	5410(1)	1419(2)	31(1)
N(1)	10306(8)	5809(4)	1938(5)	30(1)
N(2)	8959(8)	6275(4)	3430(4)	28(1)
C(12)	8414(11)	7406(5)	1258(5)	30(2)
C(11)	7032(11)	5719(6)	1861(6)	37(2)
C(3)	11037(15)	5127(9)	447(7)	59(3)
C(10)	9395(11)	7552(5)	1909(6)	34(2)
C(1)	13082(13)	6161(8)	1322(9)	54(3)
C(2)	12394(15)	4524(7)	1899(8)	54(3)
C(5)	6651(16)	6138(11)	4578(9)	74(5)
C(4)	6439(13)	7265(8)	3265(8)	55(3)
C(6)	8510(20)	7592(9)	4520(10)	82(6)

Table B.1. Continued

	x	*y*	*z*	*U*(eq)
C(9)	10120(17)	5744(10)	4962(7)	59(3)
C(8)	12034(12)	6089(8)	3655(7)	49(3)
C(7)	10033(14)	4651(7)	3607(8)	51(3)
C(22)	7410(20)	3520(7)	2222(10)	72(5)
C(23)	7606(15)	4277(7)	1896(9)	52(3)
C(19)	5992(12)	4792(7)	2804(7)	46(2)
C(18)	6899(10)	4905(6)	2180(6)	36(2)
C(21)	6521(19)	3427(9)	2829(10)	74(5)
C(20)	5818(16)	4050(9)	3118(9)	62(4)
C(16)	6062(12)	7427(6)	737(6)	40(2)
C(17)	7021(12)	7661(6)	1277(6)	38(2)
C(15)	6478(13)	6923(6)	131(6)	40(2)
C(14)	7846(13)	6684(6)	90(6)	40(2)

Table B.2. Anisotropic displacement parameters ($Å^2$ x 10^3) for **10**. The anisotropic displacement factor exponent takes the form: $-2\pi^2[h^2a^{*2}U^{11} + ... + 2hka^*b^*U^{12}]$

	U^{11}	U^{22}	U^{33}	U^{23}	U^{13}	U^{12}
C(13)	35(4)	32(4)	34(4)	3(3)	6(4)	0(4)
Ta(1)	22(1)	20(1)	22(1)	2(1)	-2(1)	-1(1)
Si(2)	44(1)	45(2)	30(1)	1(1)	6(1)	11(1)
Si(3)	36(1)	40(1)	28(1)	5(1)	-4(1)	5(1)
Si(1)	29(1)	29(1)	34(1)	-4(1)	2(1)	1(1)
N(1)	32(4)	26(3)	30(3)	-3(3)	-3(3)	2(3)
N(2)	32(3)	30(3)	22(3)	3(3)	2(3)	0(3)
C(12)	40(4)	22(3)	28(4)	8(3)	1(4)	-1(3)
C(11)	40(5)	34(4)	37(5)	8(4)	-12(4)	-11(4)
C(3)	55(7)	82(9)	41(6)	-27(6)	0(6)	6(7)
C(10)	37(4)	27(4)	36(4)	3(4)	-1(4)	-5(3)
C(1)	44(6)	52(6)	68(8)	-6(6)	12(6)	-10(5)
C(2)	61(7)	43(6)	56(7)	4(5)	1(6)	21(6)
C(5)	58(7)	105(12)	58(8)	36(8)	23(7)	18(9)
C(4)	46(6)	66(7)	54(7)	11(6)	9(5)	21(6)
C(6)	122(16)	53(7)	72(9)	-29(7)	-36(11)	25(9)
C(9)	66(8)	79(9)	32(5)	5(6)	-7(5)	12(7)
C(8)	38(5)	72(8)	38(5)	4(5)	-9(4)	-9(5)

Table B.2. Continued

	U^{11}	U^{22}	U^{33}	U^{23}	U^{13}	U^{12}
C(7)	55(7)	35(5)	61(7)	18(5)	3(6)	8(5)
C(22)	97(12)	33(5)	85(11)	-6(6)	-33(10)	6(6)
C(23)	60(7)	38(5)	58(7)	-3(5)	-15(6)	-8(5)
C(19)	38(5)	49(6)	51(6)	15(5)	-6(5)	-18(4)
C(18)	39(5)	32(4)	38(5)	11(4)	-17(4)	-14(4)
C(21)	85(10)	54(7)	84(10)	36(7)	-38(9)	-37(8)
C(20)	69(8)	58(7)	60(7)	27(7)	-10(7)	-28(7)
C(16)	34(4)	46(5)	40(5)	6(4)	-4(4)	4(4)
C(17)	46(6)	36(5)	32(5)	5(4)	-2(4)	8(4)
C(15)	48(6)	44(5)	29(4)	4(4)	-5(4)	-1(4)
C(14)	53(6)	43(5)	25(4)	4(4)	2(4)	3(4)

Table B.3. Atomic coordinates (x 10^4) and equivalent isotropic displacement parameters (Å^2 x 10^3) for ***trans*-11**. *U*(eq) is defined as one third of the trace of the orthogonalized U^{ij} tensor.

	x	*y*	*z*	*U*(eq)
Ta(01)	4861(1)	5659(1)	6037(1)	13(1)
Si(1)	6943(1)	6344(1)	7919(1)	21(1)
Si(2)	7408(1)	6894(1)	5797(1)	20(1)
Si(3)	2824(1)	4754(1)	7834(1)	21(1)
O(1)	3923(2)	5287(1)	4649(1)	16(1)
N(1)	6547(2)	6262(1)	6638(1)	16(1)
N(2)	4008(2)	5150(1)	7017(2)	19(1)
C(4)	6938(3)	5311(2)	8544(2)	30(1)
C(1)	3459(3)	6755(2)	5914(2)	23(1)
C(9)	1069(3)	4522(2)	7178(2)	31(1)
C(2)	2781(3)	5671(2)	4074(2)	30(1)
C(11)	2518(3)	5554(2)	8799(2)	32(1)
C(8)	7207(4)	8018(2)	6122(2)	36(1)
C(5)	8775(3)	6767(2)	8200(2)	34(1)
C(6)	6572(3)	6746(2)	4523(2)	23(1)
C(7)	9314(3)	6594(2)	5709(2)	35(1)
C(10)	3547(3)	3779(2)	8418(2)	35(1)

Table B.3. Continued

	x	*y*	*z*	*U*(eq)
C(3)	5650(4)	7064(2)	8479(2)	35(1)

Table B.4. Anisotropic displacement parameters ($Å^2 \times 10^3$) for ***trans*-11**. The anisotropic displacement factor exponent takes the form: $-2\pi^2[h^2a^{*2}U^{11} + ... + 2hka^*b^*U^{12}]$

	U^{11}	U^{22}	U^{33}	U^{23}	U^{13}	U^{12}
Ta(01)	14(1)	13(1)	14(1)	-1(1)	1(1)	0(1)
Si(1)	26(1)	18(1)	18(1)	-2(1)	-3(1)	0(1)
Si(2)	20(1)	17(1)	22(1)	2(1)	-1(1)	-4(1)
Si(3)	22(1)	22(1)	19(1)	3(1)	5(1)	-2(1)
O(1)	14(1)	17(1)	18(1)	-1(1)	-2(1)	4(1)
N(1)	18(1)	13(1)	17(1)	0(1)	0(1)	-2(1)
N(2)	21(1)	19(1)	19(1)	-1(1)	2(1)	-2(1)
C(4)	39(2)	28(1)	22(1)	4(1)	-8(1)	-2(1)
C(1)	20(1)	23(1)	26(1)	-5(1)	2(1)	5(1)
C(9)	20(1)	38(2)	35(2)	-2(1)	6(1)	-4(1)
C(2)	28(2)	30(2)	32(2)	-10(1)	-15(1)	14(1)
C(11)	35(2)	38(2)	24(1)	-4(1)	9(1)	0(1)
C(8)	54(2)	18(1)	36(2)	2(1)	-1(1)	-7(1)
C(5)	36(2)	34(2)	30(1)	-2(1)	-12(1)	-10(1)
C(6)	24(1)	22(1)	23(1)	4(1)	3(1)	-1(1)
C(7)	21(1)	49(2)	36(2)	9(1)	2(1)	-5(1)
C(10)	37(2)	28(2)	40(2)	12(1)	4(1)	-2(1)

Table B.4. Continued

	U^{11}	U^{22}	U^{33}	U^{23}	U^{13}	U^{12}
C(3)	48(2)	32(2)	25(1)	-8(1)	1(1)	7(1)

Vita

Seth C. Hunter was born on April 2, 1985 in Chesterfield, VA to Robert and Gina Hunter. His adolescence education was through the Chesterfield and Powhatan County public school systems. He graduated from Powhatan High School in 2003. In the following fall Seth enrolled in Virginia Commonwealth University (Richmond, VA). He graduated in May 2008 with a B.S. degree in Chemistry. Seth conducted undergraduate research with Dr. Hani El-Kaderi on covalent organic frameworks. He began his graduated studies in chemistry at the University of Tennessee, Knoxville in August 2009.